Characteristics of Offshore Wind Farm Wakes and their Impact on Wind Power Production from Long-term Modelling and Measurements

Department of Wind Energy Master Report

Erin Natasha Langor

DTU Wind Energy-M-0315

August 2019

DTU Wind Energy
Department of Wind Energy

Author: Erin Natasha Langor

Title: Characteristics of Offshore Wind Farm Wakes and their Impact on Wind Power Production from Long-term Modelling and Measurements

DTU Wind Energy-M-031515
August 2019

Project period:
January 2019 – August 2019

ECTS: 45

Education: Master of Science

Supervisor:
Marc Imberger
Xiaoli Guo Larsén
DTU Wind Energy

Simon Walson
TU Delft

Remarks:
This report is submitted as partial fulfillment of the requirements for graduation in the above education at the Technical University of Denmark.

DTU Wind Energy is a department of the Technical University of Denmark with a unique integration of research, education, innovation and public/private sector consulting in the field of wind energy. Our activities develop new opportunities and technology for the global and Danish exploitation of wind

TECNHICAL UNIVERSITY OF DENMARK

Abstract

Faculty Name
Department of Wind Energy

Master of Wind Energy

Characteristics of Offshore Wind Farm Wakes and Their Impact on Wind Power Production from Long-Term Modelling and Measurements

by Erin LANGOR

As the penetration of offshore wind farms continues to increase in Western Europe, the North Sea in particular is becoming more densely populated by offshore wind farms. Wind turbine wakes have been a topic of great research in the field of wind energy for some time, however the industry now seeks an understanding of the influence of the wake from one wind farm on the performance of a downstream wind farm. Few studies have been conducted to this end. This project will contribute to the greater work of the DTU OffshoreWake project. This master thesis will use 2018 SCADA data provided by the project partner, Vattenfall, meteorological mast data provided by BMWi and PTJ, and the author will conduct and analyse simulations using the Weather Research and Forecasting (WRF) model for the same time period. Additionally, this project will comment on the validity of the wind farm parameterization sub-models within WRF, and investigate the dependance of wakes on climatological variables and offer a longer term study than previously conducted, therefore giving the possibility of conclusions with greater certainty based on this body of work. It is found that both of the wind farm parameterization schemes (Fitch and EWP) used in this project can reasonable replicate the trends seen in the measured data. The EWP scheme tends to over-predict both gross power production and mean wind speed, while the Fitch scheme tends to underpredict the same. However, for both schemes, good agreement is found with measurements when the wind speed is accurately predicted. Wind farm wakes are observed in SCADA data and WRF simulations. The magnitude of velocity deficit tends to increase for seasons in which atmospherically stable conditions are most frequent. In the region of study, these stable conditions are accompanied by generally lower wind speeds and winds which prevail from the east.

Acknowledgements

This document represents the completion of a period of study, and a period of my life, that has been personally challenging but also productive and rewarding.

I wish to thank to thank my supervisors, Dr. Xiaoli Guo Larsen, Marc Imberger, and Dr. Ir. Simon Watson for their guidance and encouragement, and all my professors and mentors during the past two years. Without your patience, encouragement, critical discourse and insightful sharing, this accomplishment would not be possible. I also wish to extend a big thank you to Jana Fischereit, Andrea Hahmann and Tobias Torben Ahsbahs for their much needed technological support.

Central to this study was the data shared by Vattenfall and the support of DTU and TU Delft. A sincere thank you for helping me contribute to the area of Wind Energy Research.

Contents

List of Figures

List of Tables

List of Abbreviations

ARW	Advanced Research WRF
ASL	Above Sea Level
CFD	Computational Fluid Dynamics
DNS	Direct Numerical Simulation
EWP	Explicit Wake Parameterization
LES	Large Eddy Simulation
NCAR	National Center for Atmospheric Research
NWP	Numerical Weather Prediction
RANS	Reynolds Averaged Navier Stokes
SAR	Synthetic Aperature Radar
SCADA	Supervisory Control And Data Acquisition
TKE	Turbulent Kinetic Energy
WPS	WRF Pre-processing System
WFP	Wind Farm Parameterization
WRF	Weather Research and Forecasting

Chapter 1

Motivation

During the course of this master thesis, the IPCC (Intergovermental Panel on Climate Change) of the United Nations released a special report on global warming. The report states that human activities have caused global warming of approximately 1^oC above pre-industrial levels. In order to keep global warming below 1.5 ^oC, by 2030, anthropogenic CO_2 emissions must be reduced by 45% of their 2010 levels [1]. The power sector is the largest single contributer to global greenhouse gas emmissions, and according to WindEurope, wind energy is the most efficient solution to reduce the emissions from this sector [2]. Presently, Europe has 178.8 GW of installed wind power installations (onshore and offshore combined), and this figure is likely to surpass the installed capacity of gas generation in 2019, which would make wind energy the largest form of power generation in Europe. In fact, wind power installations accounted for the lion's share of new installations in the EU in 2018, making up 48 % of the capacity of all new power installations [3]. Of the 18.5 GW of wind power capacity installed in Europe in 2018, 2.6 GW was installed offshore. This is a proportion which has been more or less increasing over the past decade [4]. Growth in the industry is evident, and the stakes of our planet's climate crisis are evidently high; however, the modern wind power industry is facing new challenges which must be tackled in order to continue to deliver low-carbon energy to Europe, and the world.

Wind energy proposes a carbon-free, renewable energy source, with a single wind park capable of delivering hundreds of megawatts of electricity to a power grid (which can power hundreds of thousands of homes). However, two factors are essential for a productive wind farm - a strong wind resource and proximity to energy transmission infrastructure. As the wind power industry continues to grow, and especially as new developments are moving offshore, new developments are being constructed in regions nearby to one another. This seems to be a good economic decision, as the new development will benefit from the existing electricity transmission infrastructure but are subject to favorable wind resources. However, researchers have begun to investigate wind farm wakes and have found wind farm wakes in offshore environments which last upwards of 70 km behind their source wind farm [5]. Similar to a wind *turbine* wake, a wind *farm* wake describes the region behind the wind farm (or, wind turbine) characterized by lower wind speeds and increased turbulence intensity. If a wind farm is close enough to another wind farm, it may find itself operating, at least some of the time, in the wake of its neighbour. This translates to lower wind speeds, possibly higher turbine loads and certainly lower power generation (and lower revenue!) during these waked periods. Julie Lundquist et al. have studied an onshore site in West Texas and found a 5% decrease in power production from a wind farm which is occasionally in the wake of another wind farm. While 5% may not seem like a lot, Lundquist et al.'s economic analysis reveals other *costs* that should be considered. The loss in potential revenue, forgone production tax credits, and the societal cost of CO_2 emissions caused by fossil fuel generation sources which must compensate for the missing wind power production. The authors of this study emphacize the need for understanding these wake effects to ensure the sustainable development and stewardship of wind resources [6].

Figure 1.1 shows growth of global installed wind power capacity over the past 4 years. The bulk of this growth can be attributed to development in China and Europe. Looking specifically to the offshore wind power industry in Europe, Figure 1.2 indicates the the North Sea is the most developed basin in the region. Zooming in on the North Sea, Figure 1.3 indicates the locations of wind farms currently operating in the North Sea region. On this map, the blue polygons indicate a region of wind power development, either zoned for development, in the planning stage, under construction or operational (see map legend). It can be seen that there are two main regions of development in the basin; off the East coast of England, and the region North of Germany/Holland and West of Denmark. With dozens of wind farms in the region, it is possible that the wind farm wakes are impacting the climatology in the region. The OffshoreWake project is a joint venture between various disciplines within DTU Wind and Vattenfall, and aims to investigate the wind farm wake effect on wind farms and the Danish power system. Vattenfall is one of the largest wind power operators and developers in Europe, and is specifically concerned with the effect of an increased penetration of wind power on the Danish power system. For this reason, Vattenfall has collaborated with DTU Wind on the OffshoreWake project [7].

This Master Thesis will address the issue of the wind farm wake effect. With the goal of characterizing wind farm wakes, this project will use operational data from two wind farms and meterological mast data to validate mesoscale modelling conducted using the Weather Research and Forecasting model (WRF). The simulation data can then be used to identify wind farm wakes, and characterize wind farm wakes based on metorological indicators.

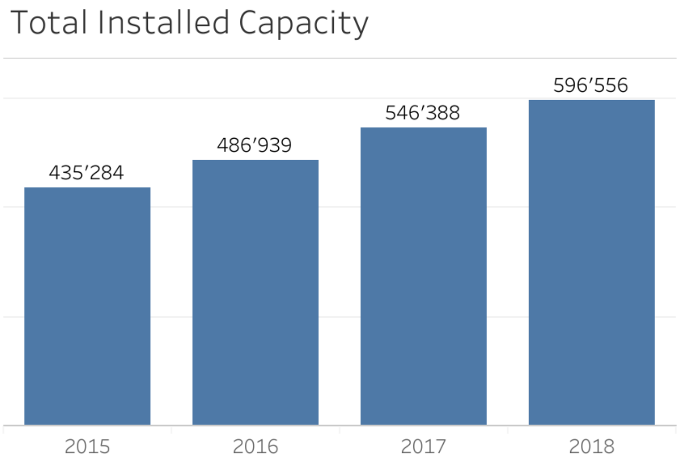

FIGURE 1.1: Total installed capacity worldwide, in MW [8]

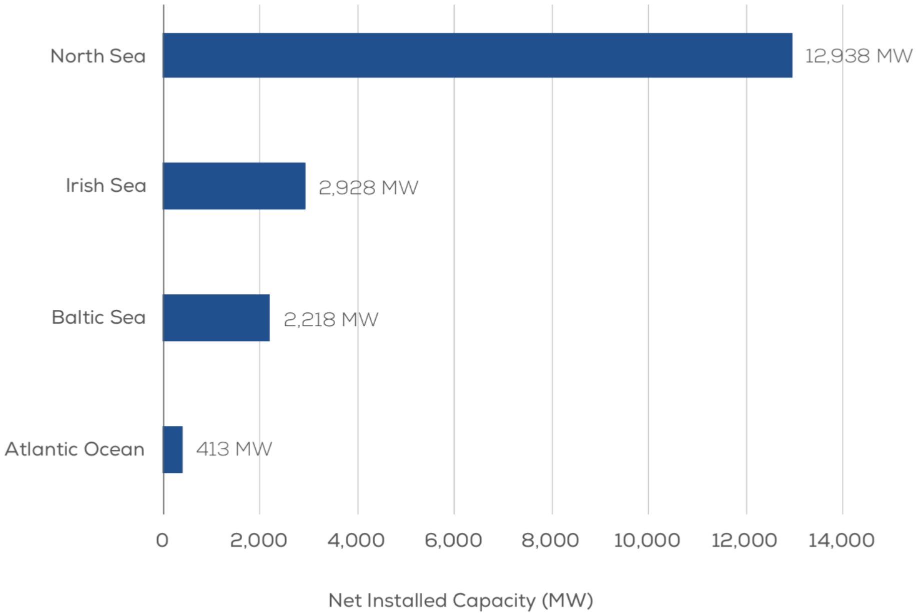

FIGURE 1.2: Total installed capacity European offshore wind energy, per basin, in MW [3]

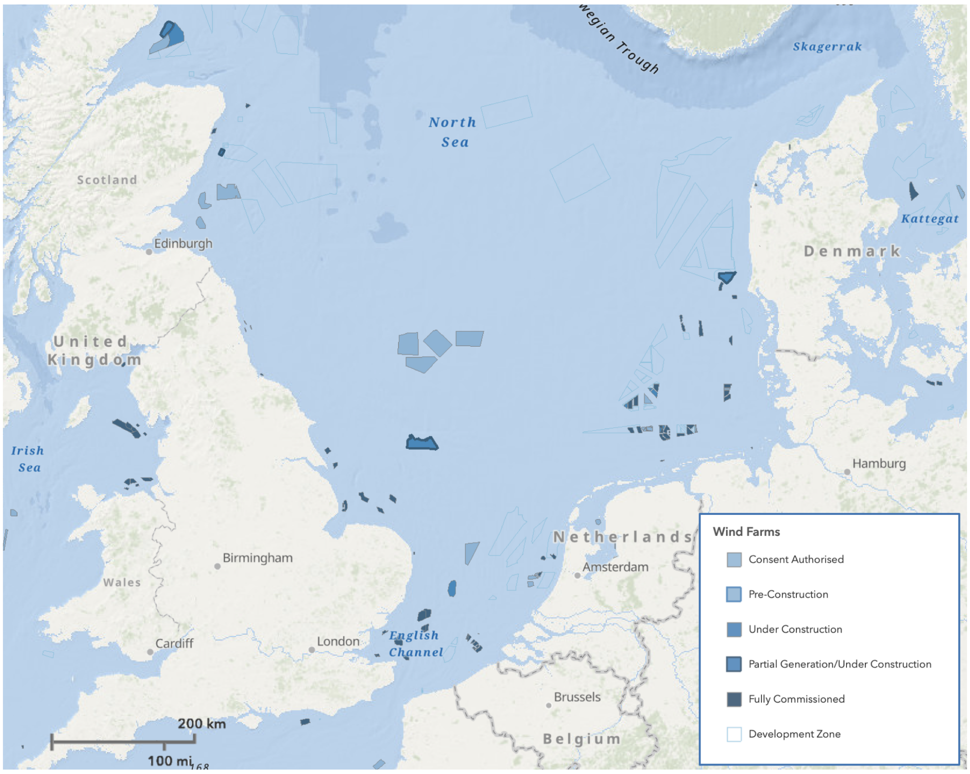

FIGURE 1.3: Offshore wind power projects in the North Sea [9]

Chapter 2

Project Overview

This project contributes to the OffshoreWake project, a joint venture between various disciplines within DTU Wind, and Vattenfall [7]. The OffshoreWake project aims to investigate the impact of wind farm wakes on the power performance of wind farms and consequently on the Danish power system. The site chosen for this project is Vattenfall's SandBank and DanTysk wind farms. These two wind farms are approximately 20 km apart, which the author expects to be close enough to exhibit wind farm shadow effects. SCADA data for both wind farms has been provided by Vattenfall. Analysis will be conducted for the entirety of 2018. The approximate area of interest is indicated with a red rectangle in Figure 2.1, with Sandbank indicated by *SB*, and DanTysk by *DT*.

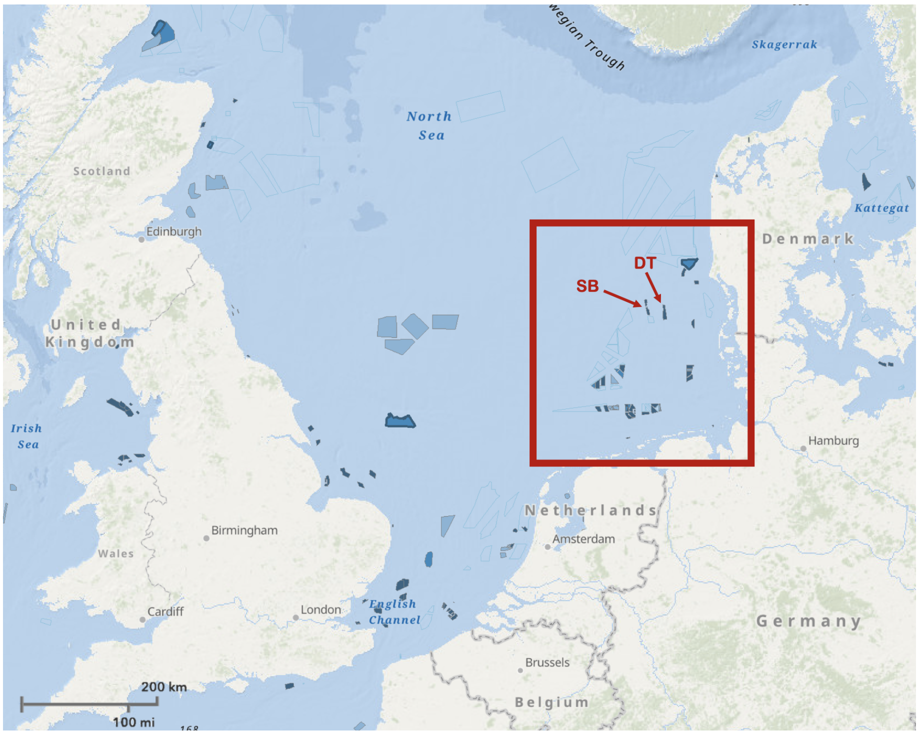

FIGURE 2.1: Area of interest in North Sea [9]

2.1 Research Questions

1. Which climatological factors influence wind farm wakes?
2. Do the wind farm parameterization schemes in WRF accurately model the wind climate?
    (a) Does one scheme (EWP or Fitch) perform better than the other?

2.2 Research Aim & Objectives

Characterize offshore wind farm wakes in terms of meteorological parameters by conducting long-term mesoscale modelling of a region with available power performance data for model validation.

(a) Assess the validity of wind farm parameterizations in WRF
(b) Assess dependence of wind farm wakes on climatological variables

2.3 Research Methodology

The authour will follow a modeling and validation approach in this study. Long term climatological data for the region will be studied and will report the climatology of 2018. Next, SCADA data for 2018 will be studied, specifically looking for evidence of wind farm wakes. WRF simulations will be conducted for the entirety of 2018 using WRF. The simulations will be executed three times: without parameterization of wind farms, using the Fitch wind farm parameterization, and using the explicit wake parameterization scheme. SCADA data will be used once again to validate the WRF simulation results. Finally, the WRF results will be analyzed to determine the influence of various climatological parameters (wind speed, wind direction, etc.) on the generation of wakes and the power performance of the subject wind farms.

Chapter 3

Literature Review

The study of wind turbine wakes is well developed, from the early engineering models of Lissaman [10] and [11] to modern techniques involving LES and CFD models. These models have been used to study wind farm wakes, however these studies tend to focus on the *internal* wind farm wakes [10]. The study of a wind farm far-wake is challenging, as the domain extends by tens of kilometers, in all wind directions (compared to an internal farm wake study). For measurement campaigns, this requires multiple met masts or LiDAR, which can be an expensive endeavour. Even model-based studies can be computationally expensive, and require a certain amount of field measurements for validation. Consequently, the field of wind farm wake modelling suffers from a lack of high quality experimental data which can be used to validate models [12].

Various acquisition methods have been employed to obtain in-situ measurements for wind farm wake studies. For example, Synthetic Aperature Radar (SAR) data is collected from satellites and aircraft and the resultsing wind speed data is used to study wind farm wakes [5], [13], [14], [15]. Satellite SAR-based studies suffer from long repeat-cycles between measurements at a particular location (resulting in few samples), interference in results based on ocean bathymetry and the necessity of wind direction measurements to extract wind speed from the radar signal (NRCS) [14]. Platis and Siedersleben document their *"first in-situ evidence of wakes in the far-field behind offshore wind farms"* after a measurement campaign employing a research aircraft surveyed the wake region behind several wind farms in the German Bight [16], [17]. This study benefits from direct measurement over the 3D wake region, however is limited by the time-delay in measuring the extents of the wake, and ad hoc nature of the the measurement campaign. Both [5] and [16] observed wakes up to 70 km. Though these were observed at different locations in the North Sea, the observed persistence of offshore wind farm wakes suggests that they are likely present in other locations and can have a measurable influence on the regional climatology.

Numerous studies have been conducted to study the accuracy of wind farm parameterizations in WRF [18], [19], [16], [17], [20], [21]. Siedersleben et al. performed a validation study of the Fitch WFP in WRF, using the airborne in-situ measurements, discussed above. The study aimed to provide a validaton of *real* WRF simulations instead of the more common *ideal* mode validation [17]. It was found that the upstream wind speed is under-predicted by the model, by up to 1.9 ms^{-1}. The velocity deficit is well-predicted by the simulation, however the underprediction of the upstream wind speed results in a lower simulated power production. This under-prediction of upstream wind speed has been identified in other studies, [22], [14] and highlighted in [18] as the critical factor in improving WFP. Siedersleben et al. indicate that the deviation in simulated background flow dominates the errors seen between the observed and simulated wake.

Few studies directly comparing the performance of the Fitch and EWP WFP have been conducted [19], [21]. Volker et al. compare ideal simulations using Fitch and EWP to measurements at Horns Rev I. For both schemes, the velocity deficit in the wake agrees well with the measurements. The vertical cross section of TKE is considerably different between the two schemes. The TKE difference is over six times greater for Fitch compared to EWP. For the EWP scheme, TKE increases after the wind farm, with a region of decreased TKE below hub height. The Fitch scheme has a large increase in TKE within the wind farm area, from the lowest model, reaching a maximum at hub height. These results are however not compared against any measurements in the study.

Jimenez et al. conducted WRF simulations of Horns Rev over a 3-year period, to accompany SCADA data available for the same period [23]. The authors performed their simulations using the Fitch scheme, for both the default power and thrust coefficient settings within the model, and using manufacturer data to update these values. The use of manufacturer turbine data improved the agreement of simulation results with the measurements.

Best practices in WRF can also be gleaned from the work of Hahmann et al. [22]. Hahmann et al. conducted several, year-long WRF simulations in the North and Baltic seas and compared the results with high-quality met mast and lidar data over the same area. The study found for the region considered, that the model is insensitive to the model variations in the study, except for the model boundary layer parameterization and the model spin-up time. It is found that the spin up time for offshore conditions is likely larger than 12 hours and should be longer for onshore analyses.

The study of wind farm wakes is dominated by case studies and few long-term studies. Although it is common practice to conduct simulations using WFP in WRF, there are few direct comparisons of the Fitch and EWP schemes. Perhaps because the latter scheme is relatively new. This project aims to contribute to the field of study by offering an analysis of long term measurements and simulations. Through this long-term dataset, the further evidence can support the ability of WFP to model wind farm wakes. The conclusions reached in this project can be integrated into power production models and can provide motivation to further improve current mesoscale models.

Chapter 4

Wakes and Wake Modeling

This section offers a brief intorduction to the key concepts discussed throughout this project, specifically: wakes, wake modelling, WRF and some climatological concepts.

4.1 Wakes

A wake is the region downstream of a flow disturbance, characterized by decreased flow velocity and increased turbulence intensity. In the context of the wind energy industry, the study of wakes has been primarily focused on the wake created by a single turbine.

The magnitude of wind speed reduction downwind of a turbine is determined by the turbine's thrust coefficient, due to the extraction of momentum from the flow (which is ultimately converted to power). Due to the decrease in pressure on the downstream side of the rotor, the region of slower wind speeds in the wake is slightly larger than the rotor diameter (as can be seen in Figure 4.1, A_1 is larger than A). The boundary between slower wake and the free stream wind (represented by the cylindrical outline in Figure 4.1) is a source of shear-induced turbulence, as the two regions begin to mix at this interface. Within the near-wake (generally taken to be the first few rotor diameters downstream, [24]), mechanical turbulence exists due to the shed vortices from the rotor itself.

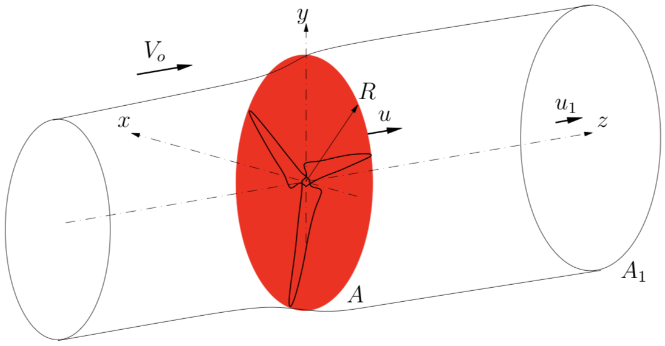

FIGURE 4.1: Actuator disk momentum theory [25]

This mechanical turbulence dissipates relatively quickly, and as the wake propagates downstream, the shear-induced turbulence promotes mixing from the wake and the free stream. This behaviour is visualized in Figure 4.2, where the velocity deficit profile is shown in blue, and the shear-induced turbulence is indicated as "mixing". Effectively, the shear-induced turbulence propagates inwards in the wake region.

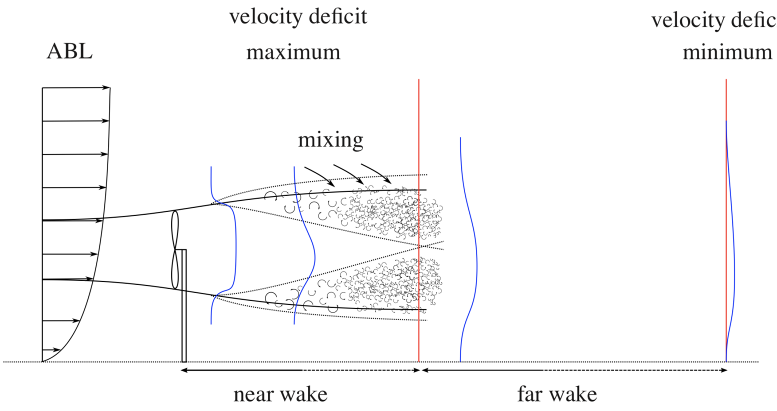

FIGURE 4.2: Wake profile [26]

Sufficiently far downstream, termed the "far-wake", the velocity deficit profile in the wake exhibits an axis-symmetric Gaussian profile and even further downstream, the wind speed eventually returns to the magnitude of the free stream speed. When ambient turbulence intensity levels are high, this creates more favorable mixing and wakes dissipate much more quickly. Ambient turbulence is largely dictated by turbine height, atmospheric stablity condition, surface roughness and complexity [27].

One important application of the study of individual turbine wakes is to determine the necessary inter-turbine spacing in a wind farm. Knowledge of a turbine wake length can ensure optimal power performance output from the entire farm, as well as ensuring that the high-frequency loading associated with turbulence can be minimized.

4.2 Wake Models

Various models have been developed to model wind turbine wakes. These models exhibit the general trend that as the models level of precision increases, so too do the required computational resources. Broadly, wake models can be divided into the following categories:

1. Engineering models
2. Computational Fluid Dynamics (CFD) models
3. Numerical Weather Prediction (NWP)

Engineering models are often highly simplified and can be solved using empirically or theoretically derived constants. Perhaps the oldest and most common Engineering wake model is the Jensen/Park model. The far-wake is approximated with a top-hat profile such that the wake width is proportional to the downstream distance from the wind turbine [11]. This model can be applied in a cascading manner to calculate the energy estimate of a turbine subject to multiple wakes [28]. Figure 4.3 shows results of the Park model in its center frame. It can be seen that this model offers a low spatial resolution, but its results are consistent with those of the higher-fidelity models.

Linearized, RANS, LES and DNS are examples of Computational Fluid Dynamics (CFD) models of varying fidelity. In general, these models deal with solving the

Navier-Stokes equations and tackle model closure in different ways. Linearized models make use of the small-disturbance assumption therefore are applicable in near-wall and far-wake scenarios. The Ainslie model is one such linearized model and uses an eddy-viscosity closure (Figure 4.3, third pane). LES resolves the large eddies, down to a particular turbulence scale (typically 1-1000 m). The eddies smaller than this scale are modeled as sub-grid stresses. When investigating flow in a wind farm environment, a very high resolution can be achieved with LES models(see Figure 4.3, first pane). Finally, DNS solves the unsteady Navier Stokes equations. This is achieved with incredibly fine spatial and temporal resolution and massive computational resources.

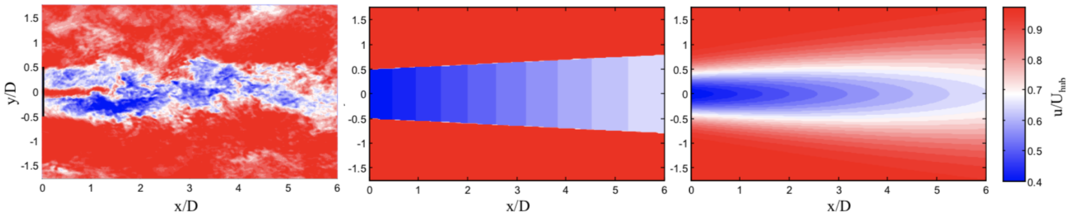

LES snapshot of full unsteady wake

Park

Eddy-Viscosity

FIGURE 4.3: Comparison of wake model outputs [29]

Numerical Weather Prediction (NWP) was first conceptualized by Lewis Richardson in 1922 [30]. In his model, meteorological data at particular spatial locations are summarized in tables, as to give a snapshot of the atmosphere at a particular instant. The physical laws of these quantities (pressure, velocity, etc.) dictate how the tabulated quantities evolve in time [31].

Modern NWP, such as the Weather Research and Forecasting (WRF) model, operate on the same basis as Richardson's initial concept, but with nearly a century of improvements in computer technology and refinment of Richardson's governing equations [32]. NWP models operate at the mesoscale level, capable of resolving the wind resources to scales of $10^3 - 10^6$ meters [33]. The turbulence associated with wind turbine wakes operates on scales much smaller than this resolution and are therefore not resolved in NWP models. In order to capture the influence of wind turbines on the mesoscale level, sub-grid parameterizations have been developed for the open-source NWP model, WRF, developed by NCAR. Early parameterizations have treated wind turbines as an element of increased roughness. More modern parameterizations such as the Fitch scheme and the Explicit Wake Parameterization (EWP) model turbines as an elevated momentum sink, according to the turbine thrust coefficient and local wind speed. Fitch and EWP differ slightly but treat the addition of turbulent kinetic energy (TKE) from the turbine in different ways. This will be discussed in more detail in the latter portion of this chapter.

For this project, it is useful to consider the applicabilty of the wake models discussed in this section, to a wind farm wake application. For such an application, it is important that a large domain be captured and the aerodynamics of the individual turbines be able to influence the surrounding wind climate.

In general, engineering models are specifically designed to model individual wind turbine wakes. However, Katic discusses the use of the Jensen model in a cascading manner so that the influence of multiple wakes can be assessed [28]. On the other hand, CFD models and NWP simulations are applicable in broader situations than just modelling wind turbine wakes. The results from a CFD model are dictated by the chosen domain discretization. To understand the flow in and around a wind farm, it is important that individual turbine dynamics can be modelled, however for investigations such as this master thesis, a very large domain is required in order to model the extents of the wind farm wake. Capturing both of these features using a CFD model would make the analysis of an entire wind farm computationally prohibitive. It then becomes clear that NWP with WFP is well suited for modelling entire wind farms and their wakes. This is also seen in the body of literature as the most common means of simulation of such projects [5], [18], [20].

4.3 WRF

The Advanced Research Weather Research and Forecasting model (ARW) is an open source NWP and atmospheric simulation software created by the National Center for Atmospheric Research (NCAR). This software has been created as a tool for research, industry and teaching, and is suitable for mesoscale applications from O(1 km) to global scales [34]. With a broad range of solver and physics options, a complete description of the software will not be offered in this report, instead readers are recommended to consult [34] for more details including coverning equations.

WRF is used as a limited area model as it relies on external informatino for initial conditions and lateral boundary conditions. WRF offers users the ability to run a simulation in the absence of meteorological boundary conditions. This is referred to as an *ideal* simulation, and takes a constant wind speed and direction as initial conditions, and runs until a steady state is achieved. It is also possible to run a *real* simulation, in which a user passes observations into the program to be used as input to the WRF pre-processing system (WPS). Boundary condition wind climate data and geographic data over the chosen domain represent the most significant inputs to the WRF program. The program begins in the WPS with the geogrid subroutine. This subroutine deals with setting the simulation domain and aligning it with the relevant static geographic data. Then the "real" data is interpreted in GRIB format in the ungrib subroutine. Next, metgrid performs a 2-dimensional interpolation of the outputs of ungrib (the meteorological input data) to the grid defined in geogrid. This WRF process is visualized in Figure 4.4.

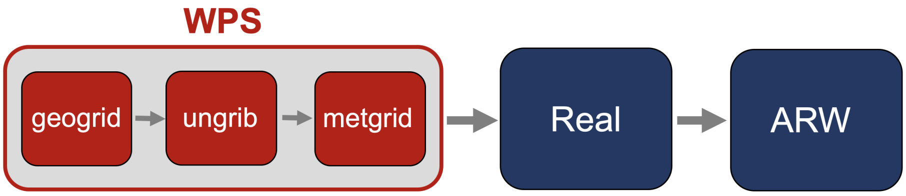

FIGURE 4.4: Flowchart of WRF processes

The *Real* routine deals with interpolating the outputs of the WPS to the vertical grid. WRF defines a terrain following "mass vertical coordinate", η, as the vertical coordinate. Defined by equation 4.1, p_h is the pressure at a given height, p_{ht} is the constant pressure at the model top, and p_{hs} is the surface pressure . η varies from 1 at the surface, to 0 at the model top. The model top pressure is defined by the user. Figure 4.5a visualizes this concept.

$$\eta = \frac{p_h - p_{ht}}{p_{hs} - p_{ht}} \tag{4.1}$$

WRF uses Arakawa C-grid staggering, shown in Figure 4.5b. The reader can see that this simply specifies the location at which variables are stored along the model grid. This is important to understand when using the model outputs to calculate, for example, total wind speed for a grid cell. U and V should be interpolated to the center of the grid cell before calculating the net wind speed. This also introduces small potential sources of error due to the interpolations.

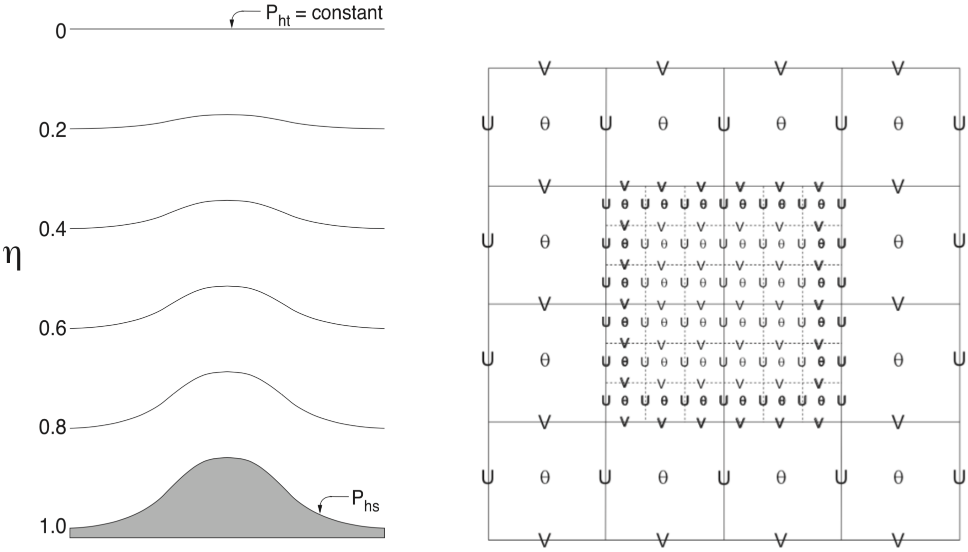

(A) Mass vertical coordinate [34]   (B) Arakawa C-grid staggering [34]

FIGURE 4.5: Demonstration of select WRF parameters.

The actual simulation in time and space takes place in the ARW block of the program. The dynamics are determined through integration of the compressible, non-hydrostatic Euler equations while the time integration is generally achieved using a third-order Runge-Kutta time integration scheme.

The vertical resolution of the WRF simulation domain is small enough to resolve the influence of a wind turbine, however the horizontal resolution is not small enough (O(1 km)). Wind farm parameterization schemes help remedy this by parameterizing the impact of wind turbines on the kinetic energy and momentum balance. The user specifies the power and thrust curves, turbine dimensions and the latitude/longitude coordinates of each turbine. The WFP only uses the position of each turbine to determine how many turbines are in a given grid cell. The influence of the turbines in a grid cell acts at the grid cell center. Therefore the wake effects between wind turbines in the same cell are not captured. The WFP also makes the assumption that all turbines are oriented perpendicular to the flow.

4.3.1 Fitch Scheme

The Fitch Scheme is the wind farm parameterization which comes "built-in" to the WRF software, first released in WRF version 3.3 [35] . When activated by the user, this wind turbine parameterization models the drag force of wind turbines as a momentum sink on the flow. The basic drag equation is shown in equation 4.2, indicating that the drag force is proportional to the turbine thrust coefficient. In this euqation, C_T is the thrust coefficient, A is the rotor area, ρ is the air density, and V is the horizontal velocity, defined by $V = (u, v)$.

The Fitch scheme uses the local wind speed and the turbine thrust curve to update the thrust coefficient as the simulation evolves in time. Previous wind turbine parameteriations assumed a constant thrust coefficient. From the drag force, follows the rate of loss of kinetic energy from the flow for a single turbine, shown in equation 4.3. The integral in this expression accounts for the variation in wind speed over the rotor area.

The loss of kinetic energy from the flow is converted to turbine power and non-productive drag (equations 4.4 and 4.5, respectively). This non-productive drag comprises mechanical and electric turbine losses (which are assumed to be negligible), and a source of turbulent kinetic energy (TKE). The turbine power calculation uses the power curve to determine the power coefficient based on local wind speed. The coefficient of TKE is therefore the remaining fraction of the momentum sink which remains after the power is produced. Represented by C_{TKE}, this quantity is the difference between the thrust and power coefficients (equation 4.6).

In the cases where there is more than one turbine in a grid cell, the horizontal turbine density parameter, N^{ij} is used to magnify the local effect of the turbnies. It is important to note that sub-grid scale interaction of turbines is not captured in this scheme. Therefore, when there are multiple turbines operating in a grid cell, the rate of production of power and the rate of added TKE will be scaled by the turbine density parameter, and will act at the grid cell center point. It should also be noted that the subscripts i, j, k in equations 4.4 and 4.5 refer respectively to the zonal, meridonal, and vertical coordinate indices. z_k indicates the height at the i^{th} vertical level.

$$F_{drag} = \frac{1}{2} C_T A \rho |V|^2 V \tag{4.2}$$

$$\frac{\partial KE_{drag}}{\partial t} = -\frac{1}{2} \int_{A_R} C_T \rho |V|^2 V dA \tag{4.3}$$

$$\frac{\partial P_{ijk}}{\partial t} = \frac{\frac{1}{2} N_t^{ij} C_P |V_{jik}|^3 V_{ijk} A_{ijk}}{(z_{k+1} - z_k)} \tag{4.4}$$

$$\frac{\partial TKE_{ijk}}{\partial t} = \frac{\frac{1}{2} N_t^{ij} C_{TKE} |V_{jik}|^3 V_{ijk} A_{ijk}}{(z_{k+1} - z_k)} \tag{4.5}$$

$$C_{TKE} = C_T - C_P \tag{4.6}$$

4.3.2 Explicit Wake Parameterization

The Explicit Wake Parameterization (EWP) scheme is a newer parameterization, developed at DTU and first published in 2015 [19]. Similar to the Fitch scheme, the EWP scheme treats wind turbines as individual drag devices and applies a grid cell-averaged drag force to represent individual turbines. Similar also to the Fitch scheme, when there are multiple wind turbines in a grid cell, the EWP scheme places them at the grid cell center and superimposes the thrust force from the individual turbines.

The key difference between the EWP and Fitch schemes is their treatment of TKE. The EWP scheme defines the sink of momentum due to TKE based on the velocity fluctuations about the ensemble averaged mean. This results in a much smaller quantity, which Volker et al. choose to neglect in their scheme. The additional generation of TKE is therefore generated by shear production which evolves through the PBL scheme.

The vertical expansion of velocity deficit is not captured in the mesoscale model and its explicit estimation is implemented in EWP. Interested readers can refer to Section 2 of [19] for the derivation. Essentially, the turbine thrust force is equated to the sink of momentum due to the entire expanded wake (equation 4.7). A relation for velocity deficit profile is defined (equation 4.8), based on the research of Tennekes and Lumkey, and incorporates an initial length scale (σ_o) to capture the near-wake expansion while describing the far wake expansion (equation 4.9). Through combination of these relations, and some manipulation of the applicable domain, an effective thrust force is defined. This effective thrust force defines the average wake expansion within a grid cell. This term is manipulated to grid averaged acceleration components which are used in the governing RANS equation.

$$\frac{1}{2}\rho C_T \pi r_o^2 \overline{u}_o^2 = \int_{-\infty}^{\infty}\int_{-\infty}^{\infty} \rho \overline{u}_o \overline{u}_d dz dy \tag{4.7}$$

$$\overline{u}_d = \overline{u}_s \, exp\left[-\frac{1}{2}\left(\frac{z-h}{\sigma}\right)^2 - \frac{1}{2}\left(\frac{y}{\sigma}\right)^2 \right] \tag{4.8}$$

$$\sigma^2 = \frac{2K}{\overline{u}_o} x + \sigma_o^2 \tag{4.9}$$

4.4 Atmospheric Stability

Atmospheric stablity refers to the stratification of the atmosphere. Specifically, it is the ratio of thermal to mechanical turbulence. Atmospheric stability can be quantified in many different ways, but is generally discussed using the following terms: stable, unstable, or neutral. A stable atmosphere is one in which vertical mixing is surpressed. Smoke from a chimney in a stable almosphere will remain in a small cross sectional area as it convects downstream. An unstable atmosphere on the other hand, will have billowy smoke from a chimney and will rapidly disperse in the downstream and vertical direction.

The Bulk Richardson number will be used in this study as the parameters are available within the data. Equation 4.10 defines the Bulk Richardson number, where

$g = 9.81\,ms^{-1}$ is the gravitational constant, T_z is the temperature at height z, U_z is the wind speed at height z and T_w is the temperature at the surface of the water. Different formulations of Richardson number have different ranges of boundary values. The values used in thie study are provided below [36].

$$Ri_B = \frac{g}{\overline{T}} \frac{(T_z - T_w)}{z} \Bigg/ \left(\frac{U_z}{z}\right)^2 \tag{4.10}$$

$$\begin{aligned} \text{unstable: } & Ri_B < -0.015 \\ \text{unstable to neutral: } & -0.015 \leq Ri_B < 0 \\ \text{neutral to stable: } & 0 \leq Ri_B < 0.015 \\ \text{stable: } & Ri_B \geq 0.015 \end{aligned}$$

Chapter 5

Data

5.1 Test site

The wind farms being investigated in this project are SandBank and DanTysk, both owned by Vattenfall. These farms are located approximately 100 and 75 km from the west coast of Denmark, in the North Sea. The details of these two wind farms are outlined in Table 5.1.

TABLE 5.1: Details of the relevant assets in the region

Asset Name	**Center Latitude [^{o}]**	**Center Longitude [^{o}]**	**# Turbines**	**Turbine Model**
FINO3	55.20	7.16	1	Met Mast
Høvsøre	56.44	8.15	1	Met Mast
SandBank	55.19	6.86	72	SWT-4.0-130
DanTysk	55.00	7.23	80	SWT-3.6-120

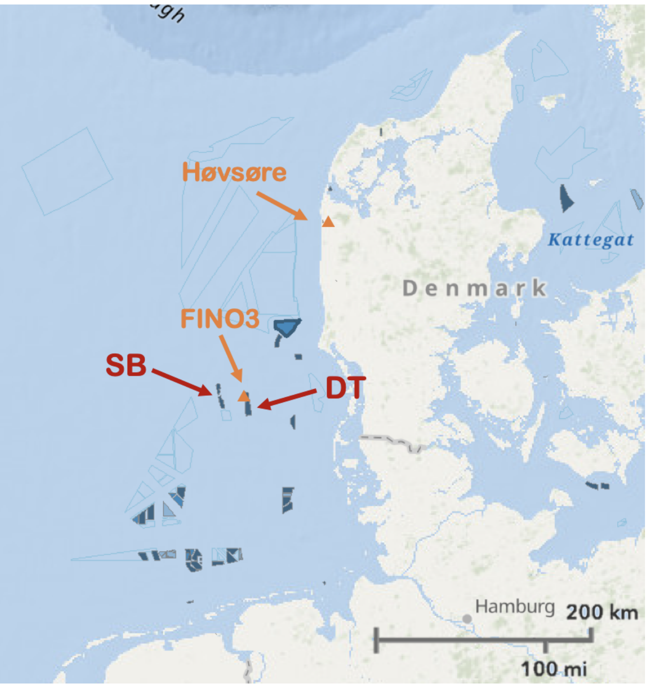

FIGURE 5.1: Data sensor locations.

5.2 Data Sources

Numerous datasets will be used in this project. This section will present each dataset, the data used in this project from each project, and if applicable, from where the data is collected. The data sources are summarized in Table 5.2 and are indicated on Figure 5.1.

First, met mast data from the FINO3 metstation [1] is used to inspect the long-term climate at the subject location. This met mast is located along the northwest edge of the DanTysk wind farm, and approximately 20km east of the SandBank wind farm. Conveniently, this dataset is collected within the subject location of this project, however the data is used with caution as the nearby wind farms likely influence the measurements. DanTysk began producing power in 2015 and SandBank began producing power in 2017. These dates will be considered when analysing this data for the long-term climate at the subject location.

Bearing in mind the possible limitations in the FINO3 measurements in the period following the construction of SandBank and DanTysk, the long-term dataset at Høvsøre has been used as a basis for comparison with FINO3. Høvsøre is an onshore test site in northwestern Denmark which is run by DTU Wind Energy. The measurements used in this thesis have been collected from a mast located onshore, 1.7km from the sea. The mast is located approximately 2m ASL and the roughness lengths surrounding the site are very low, with values in the winter which approach levels of an offshore site [37]. This dataset will only be used as a comparison with the long-term dataset from FINO3.

SCADA data from the DanTysk and Sandbank wind farms have been provided by Vattenfall for nearly all of 2018. There is a long gap in data covering the month of June, and the dataset ends on 4 December, effectively giving a second gap in the month of December. When conditioned to remove the error-flagged measurement fields, the dataset covers 78.8% of 2018 with a 10-minute sample rate. It should be noted that in lieu of a wind direction measurement, the nacelle direction measurement is presumed to indicate wind direction as measured at hub height.

The SCADA data, combined with met mast data at FINO3, makes up the in situ data that will be used to validate the WRF simulations. These data represent point sources of information within the domain simulated in WRF.

CFSv2 data (Climate Forecast System version 2) is used to initialize the meteorological fields and to provide lateral boundary conditions to the WRF Preprocessing System (WPS). CFSv2 is a fully coupled atmosphere-ocean-land reanalysis model and is initialized 4 times per day (i.e. the CFSR data is provided every 6 hours). The data is provided in GRIB format and a horizontal resolution of 0.5 and 0.2 degrees, depending on the parameter. The sea-surface temperature data from this model is also used to setup the WRF simulation.

---

[1] FINO data provided by: BMWi (Bundesministerium fuer Wirtschaft und Energie, Federal Ministry for Economic Affairs and Energy) and the PTJ (Projekttraeger Juelich, project executing organization)

TABLE 5.2: Data sources used in the project.

Name	**Data**	**Start Date**	**End Date**
FINO3	Wind speed, wind direction, SST, temperature, at numerous heights	2009-09-01 00:00	2019-01-01 00:00
Høvsøre	Wind speed, wind direction	2006-01-01 00:00	2018-12-31 00:00
DanTysk SCADA	Turbine power, wind speed, nacelle direction	2018-01-01 00:00	2018-12-04 11:40
Sandbank SCADA	Turbine power, wind speed, nacelle direction	2018-01-01 00:00	2018-12-04 11:50
CFSv2 Reanalysis	Atmospheric, SST	2017-12-31 00:00	2018-12-31 18:00

Chapter 6

Methodology

Generally, this project seeks to parameterize wind farm wakes through a modelling and validation approach. The method of this study can be briefly described by the tasks listed below. This chapter will describe in further detail the approaches used in preparing and executing the WRF simulations.

1. Prepare WRF simulations
2. Execute WRF simulations
3. Analyse in-situ data
4. Validate simulaion results
5. Wake analysis
6. WFP comparison

In this modelling and validation approach, WRF is used to simulate the atmosphere in the 3D extents of the simulation domain, over a one-year period. A wind farm paramterization is employed in order to capture the sub grid-scale influence of wind turbines on the flow. In fact, two different wind farm parameterization schemes are used so their performance can later be compared. The in situ data used in this study is in the form of year-long SCADA datasets from 2 wind farms, and long term data from 2 regional meteorological masts (approx. 10 years each). This in situ data is used to study the regional climatology and to validate the quality of WRF simulations. Once validated, the WRF results can be analysed to identify wind farm wakes and determine methods to characterize the wakes on wind speed, wind direction, stability condition and turbulent kinetic energy. Throughout the wake analysis, the results of the WFP are presented side-by-side, but their respective performance will also be addressed in a seperate analysis.

6.1 Prepare Simulations

6.1.1 North Sea Wind Farms

In addition to SandBank and DanTysk, there are numerous wind farms operating in the North Sea. Though these wind farms are on the order of tens of kilometers away from SandBank and DanTysk, it is possible that the presence of these wind farms might influence the performance of the subject wind farms, through changes to local meteorology or the direct influence of their wakes. Analytical and numerical flow models have predicted wake lengths of up to 100km [16], whereas case studies have reported measured wake lengths of 70km and above [5], [16]. Based on these figures, a conservative region covering a 150 km radius has been considered, in which all wind farms present during the year of study have been included in the wind farm parameterizations (Figure 6.1).

FIGURE 6.1: 150 km radius from center fo Sandbank and DanTysk

In order to parameterize a wind farm within WRF (using Fitch or EWP), the turbine locations and turbine data (power curve, thrust curve, hub height, rotor diameter, etc.) must be known, else they can be assumed as default values. Based on the research of [23], it is decided to use manufacturer turbine data in order to improve the accuracy of the simulations. This manufacturer data has been provided by the project partner, Vattenfall, for Sandbank and DanTysk; however, the surrounding wind farms are owned by many different companies. Unfortunately turbine locations and turbine performance data are not publicly available for many of the surrounding wind farms at the time of writing. Available to the author is a database of Satellite Synthetic Aperature Radar (SAR) images in which large objects (ferries, wind turbines, etc.) return an abnormally high radar signature thus revealing their location in satellite images. With this knowledge, SAR images taken over the wind farms of interest have been used to determine the geographical coordinates of the individual turbines in the wind farms. Publicly available data published on the the website 4C Offshore [9], such as approximate wind farm center coordinates and number of wind turbines, aided in the processing of satellite SAR data. Table 6.1 reports some of this data. Using this information, the author filtered the database of SAR images in the DTU Wind Energy database[1] to images containing the desired wind farms. These search results were inspected for cases with predominantly low

---

[1] https://satwinds.windenergy.dtu.dk

wind speeds and stable conditions. This way, the radar signals on the sea surface are relatively consistent and the jump in signal at a wind turbine location is more pronounced. The satellite SAR data files are in NetCDF format and have been processed in Matlab. From the SAR images, it is quite easy for the reader to pick out the location of the wind farms (see Figure 6.2). For each wind farm, the corresponding Satellite SAR image is cropped tightly around the bounds of the wind farm. Then, the threshold value of radar signature is tweaked until the number of cells greater than the threshold value is equal to the number of turbines in the wind farm. The result of this analysis is the latitude and longitude coordinate of every wind turbine in each of the wind farms described in Table 6.1. The results are visualized in Figure 6.3 with turbine locations shown in yellow and domain locations without turbines shown in blue. The reader can compare Figure 6.2 and Figure 6.3 to observe the agreement between the determined locations of the southern wind farms with the SAR image.

It is important to note that the uncertainty in turbine location will not be a large source of error in the final results. Regardless of the provided coordinates for each wind turbine in WRF, the wind turbine is presumed to act at the grid cell center. This immediately adds uncertainty in position on the order of one grid-cell width to the location of each turbine. Nevertheless, this method is an easy way to obtain turbine locations, and yields relatively certain results.

TABLE 6.1: Wind farm details for all wind farms to be parameterized.

Wind Farm	**# Turbines**	**Wind Farm Area [km^2]**	**Turbine Model**
Sandbank	72	47	SWT-4.0-130
DanTysk	80	66	SWT-3.6-120
Butendiek	80	33	SWT-3.6-120
Horns Rev I	80	21	V80-2.0
Horns Rev II	91	33	SWT-2.3-93
Amrumbank West	80	33	SWT-3.6-120
Nordsee Ost	48	36	6.2M126
Meerwind Sud/Ost	80	40	SWT-3.6-120
Global Tech I	80	42	M5000-116
BARD Offshore I	80	59	Bard 5.0
Veja Mate	67	51	SWT-6.0-154
Gode Wind 1 and 2	97	70	SWT-6.0-154
Nordsee One	54	31	6.2M126
Alpha Ventus	12	4	M5000-116 and Senvion 5MW
Borkum Riffgrund I	78	36	SWT-4.0-120
Trianel Windpark Borkum I	40	23	AD5-116
Gemini	150	70	SWT-4.0-130

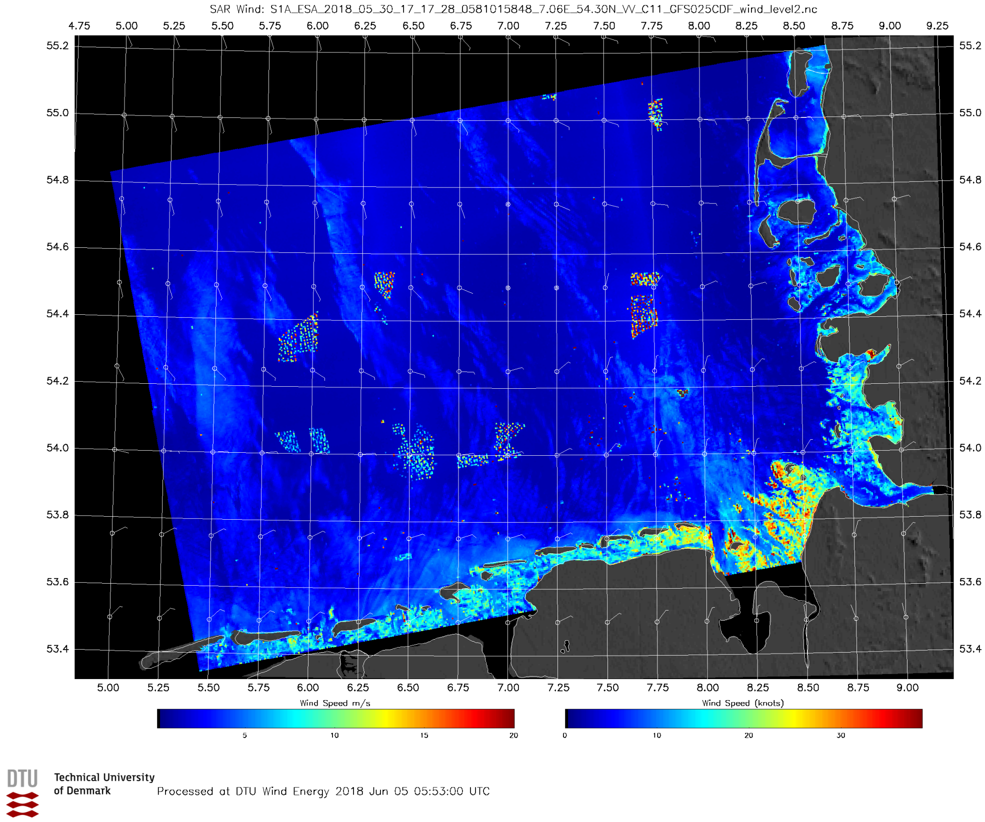

FIGURE 6.2: Sample Satellite SAR image

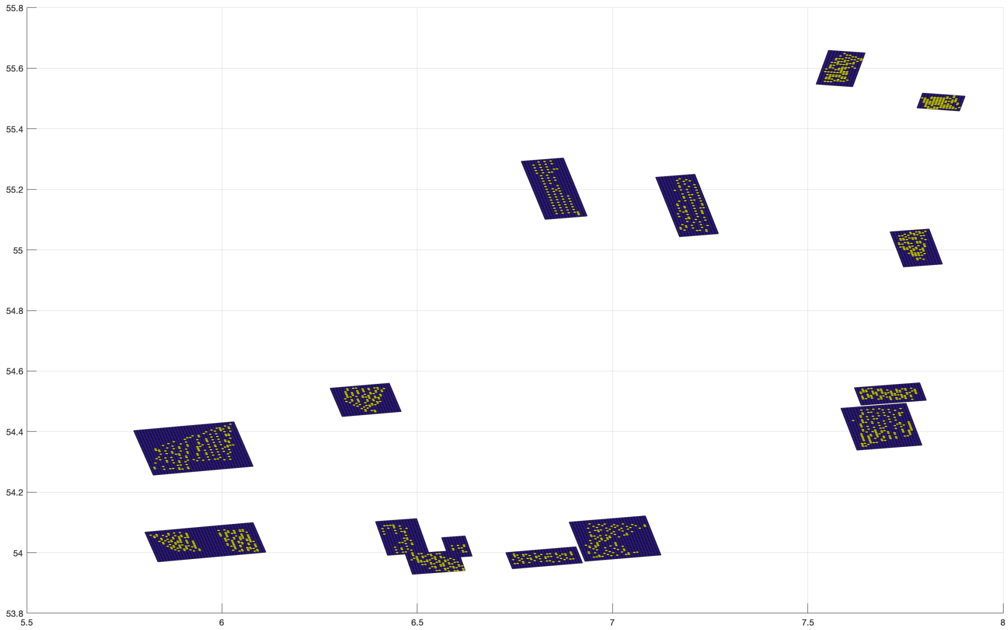

FIGURE 6.3: Output of turbine locations fron SAR graphical analysis

6.1.2 Turbine Power Curves

As mentioned in this section, there exists an option in WRF to use default wind turbine parameters, however this is less accurate than using manufacturer parameters.

It can be seen in Table 6.1 that there are 12 different turbine models used in this region, ranging from 2.3 to 6.2 MW. Most of the power and thrust curve information was obtained from the database in WindPRO [2], however the 5MW and 6.2MW turbines were unavailable in this database. Instead, the 5MW turbines were all approximated as an Adwen M5000-116 turbine, with power and thrust curves scaled from the NREL 5MW turbine. The Senvion 6.2M126 turbine was similarly scaled from the DTU 10 MW reference turbine. These approaches were used by [38] and [39] for approximating the same models of turbine.

6.2 Simulations

The intent of this project is to analyse a long-term dataset to investigate wind farm wakes, therefore simulations will be conducted for one year. Two WFP are being compared, plus one complete year will be simulated without any WFP. This control simulation will provide a basis for the behaviour of the background flow. When investigating wakes, the difference between the results of the control simulation (NOWF) and the WFP simulation (EWP or Fitch) will be used to identify the behaviour which can be attrbuted to the wind farms.

To summarize, the year 2018 will be simulated three times:

1. With no wind farm parameterizations
2. With all wind farms parameterized using the EWP scheme
3. With all wind farms parameterized using the Fitch scheme

---

[2] windPRO – EMD International A/S. [Online]. Available: https://www.emd.dk/windpro/.

Chapter 7

Model Setup

The Wind Research and Forecasting model (WRF), version 3.7 will be used for the simulations in the project, with accompanying winf farm parameterization models. A domain of 1440 km × 1260 km has been selected and will be simulated over an entire year and repeated for three different simulation configurations. The first will not include any wind farms. The second will parameterize the wind farms the Fitch scheme [35]. The third, year-long simulation will parameterize the wind farms using the Explict Wake Parameterization scheme [19]. The results from the simulation without wind farms will be subtracted from the simulations with parameterized wind farms in order to examine the impact of the presence of turbines on the local wind climate. The output of these simulations will contain instantaneous data reported every 10-minute averaged data.

Figure 7.1 shows the domain configuration for all of the simulations. The grid size in the x-direction and y-direction are equal for each domain, set to 18 km, 6 km, and 2 km for domain 1, domain 2 and domain 3, respectively. In the same order, the number of cells in the west-east direction for each domain is 81, 163 and 253. In the south-north direction, there are 71, 145 and 235 cells. The domain center is located at latitude: 55.5^o and longitude: 6.0^o. Domain 2 receives boundary condition information from domain 1 and begins at grid index (14,12) (i and j, respectively). Domain 3 receives boundary condition information from domain 2 and begins at grid index (40,34).

CFS reanalysis data will be used to initialize the simulations. Sea surface temperature inputs will also be taken from CFSR. This data is available at 6-hour intervals, therefore simulations must be multiples of this time period. The MYNN PBL scheme will be used. The model top is specified at $\eta = 50$ hPa. Runs will be initialized at 0:00 UTC and run for 11 days, which includes a 24 hour period of spin-up time, to be discarded. This practice is based on practices recommended by A. Hahamann in her study of sensitivities in offshore WRF simulations in the North and Baltic Seas [22]. The authors of the study conclude that WRF is largely sensitive to the choice of boundary layer parameterization and choice of spin-up time. Due to the regional relevance of this study, the recommendations have been heeded in this project. Figure 7.2 demonstrates the overlap in time periods achueved in these 11-day simulations. This results in 37 individual simulations for each wind farm parameterization case, totalling 111 11-day simulations. Each simulation produces a considerable amount of data, therefore the WRF model outputs which are ultimately exported to the file will be limited to domain 3 and variables pertaining to the calculations. A test case shows this results in approximately 2 GB of data per 11-day simulation. Consequently, the data will be stored on the supercomputer cluster and post-processing and analysis will also be conducted in this location.

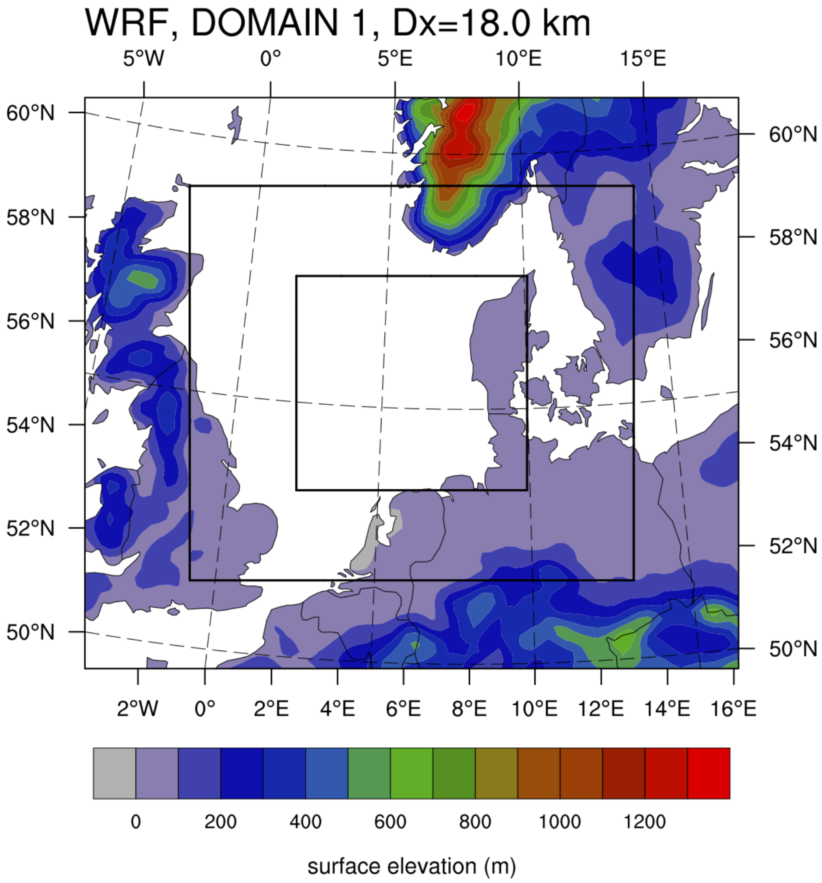

FIGURE 7.1: Domain settings for domain 1 (outer), 2 (middle), and 3 (inner).

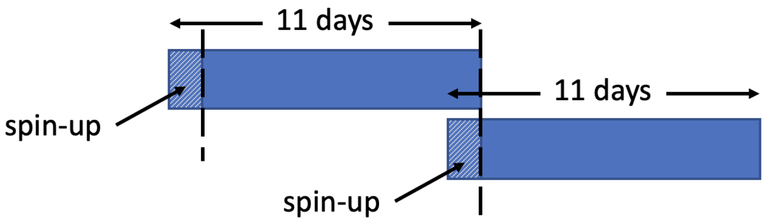

FIGURE 7.2: Set-up of consecutive simulations.

Chapter 8

Climatological Study

This section will present the results of the climatological study of the region, including analysis of 2018 data and long-term datasets from multiple data sources. 2018 is analysed in this section as the available SCADA data for the project is provided only for 2018.

8.1 2018 Climatology

8.1.1 FINO3

Figure 8.1 shows the local climatology at the FINO3 met mast for 2018, for a height of 61 m ASL. Data coverage for this year is 100%, among which 86.0% has been recovered. This results in measurements covering 86.0% of 2018 at a frequency of one measurement every 10-minutes. It should be noted that the sea surface temperature measurements occur every 30 minutes, therefore the distribution of Bulk Richardson number is constructed from approximately one third of the samples of the other statistics. The raw SST data covers 80.9% of 2018, among which 74.6 % is recovered. This results in data covering 60.4% of 2018. Figure 8.1d shows that these gaps in data are a period from April, into May, as well as the latter three months of the year.

The Weibull distribution of the 2018 data has a scale parameter of 10.4 ms^{-1} and shape parameter of 2.2. The Weibull curve is plotted with the histogram of data, showing good agreement in Figure 8.1a. The distribution of turbulence intensity (TI) in Figure 8.1b shows the values to be skewed to the lower end of the range. The annual mean value of TI is 0.09. Figure 8.1c shows a wind rose plot of wind direction, in which each bin of wind direction shows the distribution of wind speeds occurring at those wind directions. It is clear that nearly 7% of wind speeds come from the NW, with approximately 4% of wind speeds (including the largest proportion of wind speeds over 20km/h) coming from the E-NE. Finally, Figure 8.1d shows the distribution of Bulk Richardson number over 2018. Due to a low availability of SST data (sampled every 30 minutes, and 2 long gaps in data during 2018), this distribution might show some seasonal bias and has therefore been used with caution. It will be compared to a long-term dataset in the following section, where it is seen to exhibit a similar distribution to other years of better data coverage.

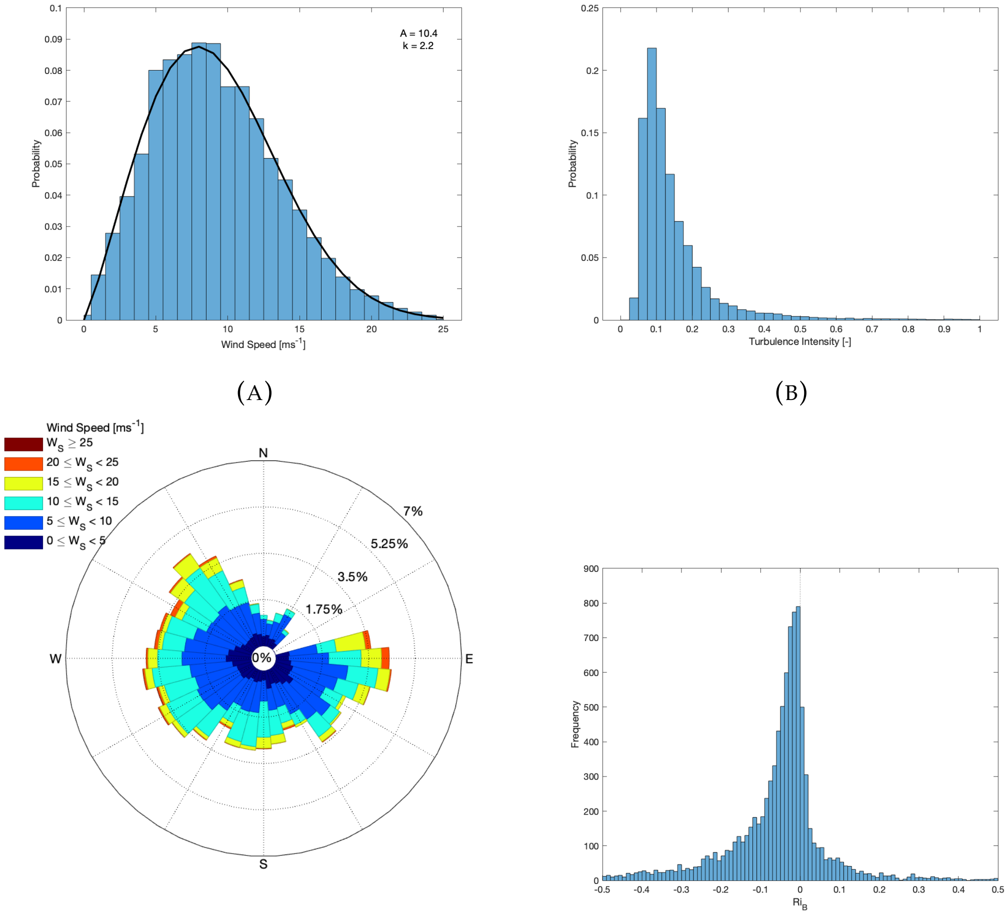

(A) (B)

(C) (D)

FIGURE 8.1: Wind resource characteristics as determined from measurements at FINO3 at a height of 61m ASL in 2018. (A) Wind speed distribution, (B) Turbulence intensity histogram, (C) Wind rose plot weighted with wind speeds, (D) Bulk Richardson number distribution.

Based on the stabilty classes discussed in the stability analysis, Figure 8.2 shows the monthly distribution of stability classes at FINO3 during 2018. As mentioned above, this dataset is missing 4-5 months of data and will therefore be considered alongside the long-term distributions of stability classes at this site. However, based on the results in Figure 8.2, the ABL is most often unstable and unstable to neutral. The frequency of unstable conditions wanes in the summer, compared to the winter months.

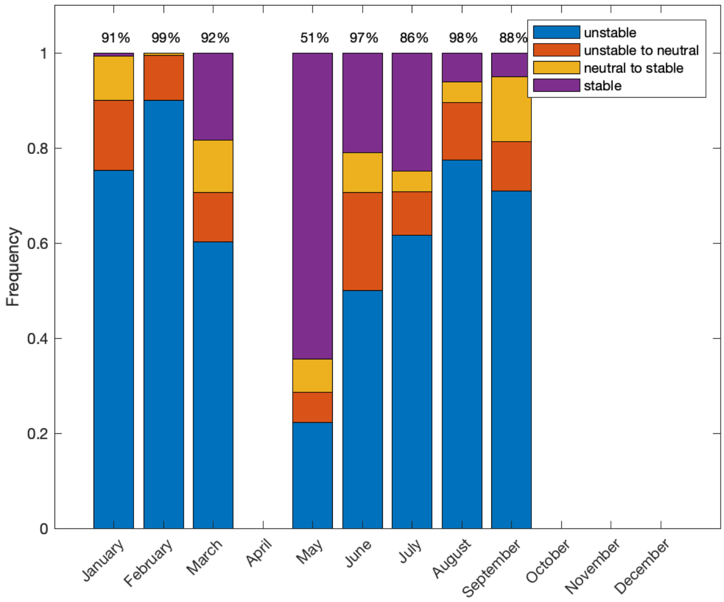

FIGURE 8.2: Distribution of stability classes at FINO3 from 2018

8.1.2 SCADA

The SCADA data provided by Vattenfall spans 1 January 2018 00:00 to 4 December 2018 11:40 and is stored at 10-minute intervals. These variables are considered in the following analysis: park curtailment setpoint, average active power, nacelle direction, average wind speed, and standard deviation of wind speed. Filtering was conducted to remove time steps containing error-flagged data. The raw dataset covers 100% of the time period, and based on the filtering, 91.4% of the available data was recovered. This results in a total coverage of 91.4% over the time period.

Figure 8.4 shows the climatological study of the wind farms. The data in this dataset comprises one sample at each wind turbine, therfore the SandBank wind farm has 72 datapoints at each time step and DanTysk has 80 per time step. The measurements taken at the internal wind turbines in the wind farm are affected by the flow through the wind farm and do not represent the free stream conditions. Therefore four *probe* locations have been chosen in each wind farm (Figure 8.3). One wind turbine is chosen on the North, East, South and West sides of the wind farm and the wind direction is examined at each of these cardinal probe locations for each time step. The Northern probe location is chosen such that winds from 315-45^o will seen directly by this turbine with little interference from any other turbines. Similarly, the Eastern probe point is unobstructed for wind directions 45-135^o. The Southern probe point covers 135-225^o, and the Western probe point covers 225-315^o. At each time step, the wind direction at each probe point is assessed (for each wind farm) and the wind direction closest to the bin center value for that quadrant is determined to be the prevailing wind direction. The wind speed at this probe point is also taken to be the prevailing wind speed. The data presented in Figure 8.4 is therefore tracking the prevailing winds, instead of presenting the climatology at a single point.

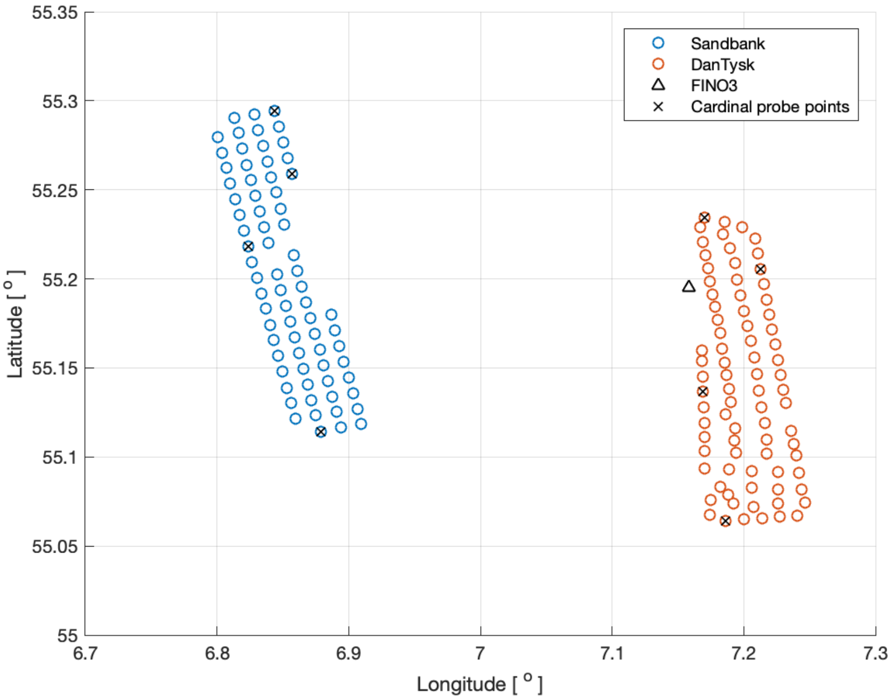

FIGURE 8.3: Map showing cardinal probe locations on each wind farm.

Figure 8.4a shows the histogram of 10-minute average wind speeds for Sandbank (blue) and DanTysk (orange). A Weibull distribution has been fit to each dataset and plotted on this figure in the same color. The shape and scale parameters for the Sandbank distribution are 10.3 ms^{-1} and 2.1, respectively. For the DanTysk distribution, these parameters are 10.5 ms^{-1} and 2.0. The distribution at Sandbank fits the histogram considerable worse than the DanTysk distribution. Looking at Figure 8.4c, the frequency of wind speeds in the 5-10 ms^{-1} range is lower in the S-SE region, as compared to Figure 8.4d. This could be due to the winds prevailing from the East and SandBank is then found in the wake of DanTysk.

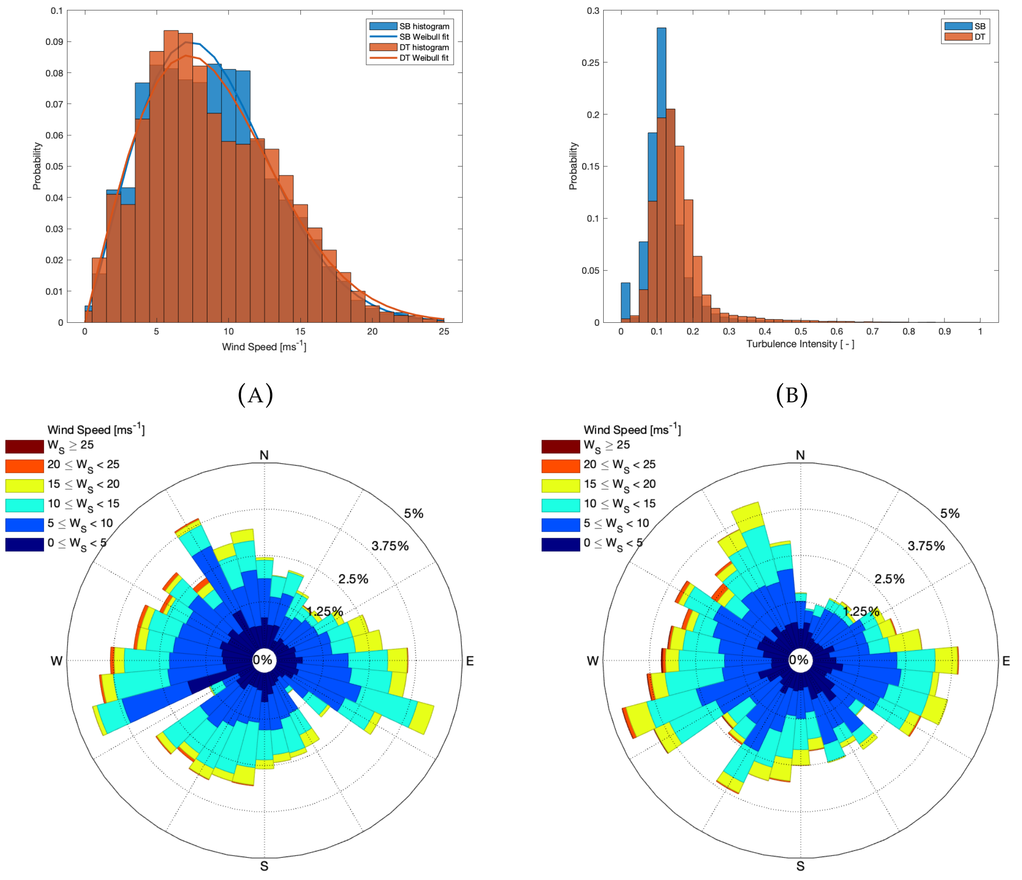

(A) (B)

(C) (D)

FIGURE 8.4: Results of climatological analysis of SCADA data at SandBank and DanTysk. (A) wind speed distribution at SandBank and DanTysk, (B) turbulence intensity distribution at SandBank and DanTysk, (C) wind rose at SandBank, (D) wind rose at DanTysk.

8.2 Long-term Climatology

To understand the 2018 climate in relation to a typical year at this location, a study of available long term datasets has been conducted, namely FINO3 and Høvsøre.

Being situated between the two subject wind farms, measurements at FINO3 are the most relevant study for the long-term climate at the subject location. However, it is possible that once SandBank and DanTysk were installed, they influenced the measurements at FINO3. For this reason, long-term data at Høvsøre has also been investigated as a means to comment on the annual trends observed at FINO3 as likely natural occurrences of possibly influenced by nearby infrastructure.

The data coverage for each annual dataset at FINO3 is shown in Table 8.1. It can be seen that the data coverage is quite high for each year (i.e. there are few gaps in the data compared to a complete data series sampled every 10 minutes). The recovery of this data (non-error flagged data) remains quite high, with a net data coverage of >85% for all years. It should be noted that this analysis applies only for wind vane measurements at 61 m and cup annemometer wind speed measurements at 61 m. The data coverage for the values used in calculations of Bulk Richardson number are shown on the relevant figures below, and are much lower than the values in Table 8.1.

TABLE 8.1: Coverage and data recovery per year at FINO3 (for wind speed and wind direction at h=61 m).

Year	**2010**	**2011**	**2012**	**2013**	**2014**	**2015**	**2016**	**2017**	**2018**
Coverage	99.2	97.1	99.3	99.99	99.99	98.9	96.7	91.5	99.99
Recovery	93.1	91.6	50.4	97.1	97.5	97.7	95.0	98.9	92.0
Total	92.3	89.0	50.0	97.1	97.5	96.7	91.8	90.5	92.0

Figure 8.5 shows the local climatology at FINO3 for a period of 9 years, from 2010-2018 (inclusive). The coefficients of the Weibull distribution are scale parameter, 10.1 ms^{-1}, and shape parameter, 2.3.

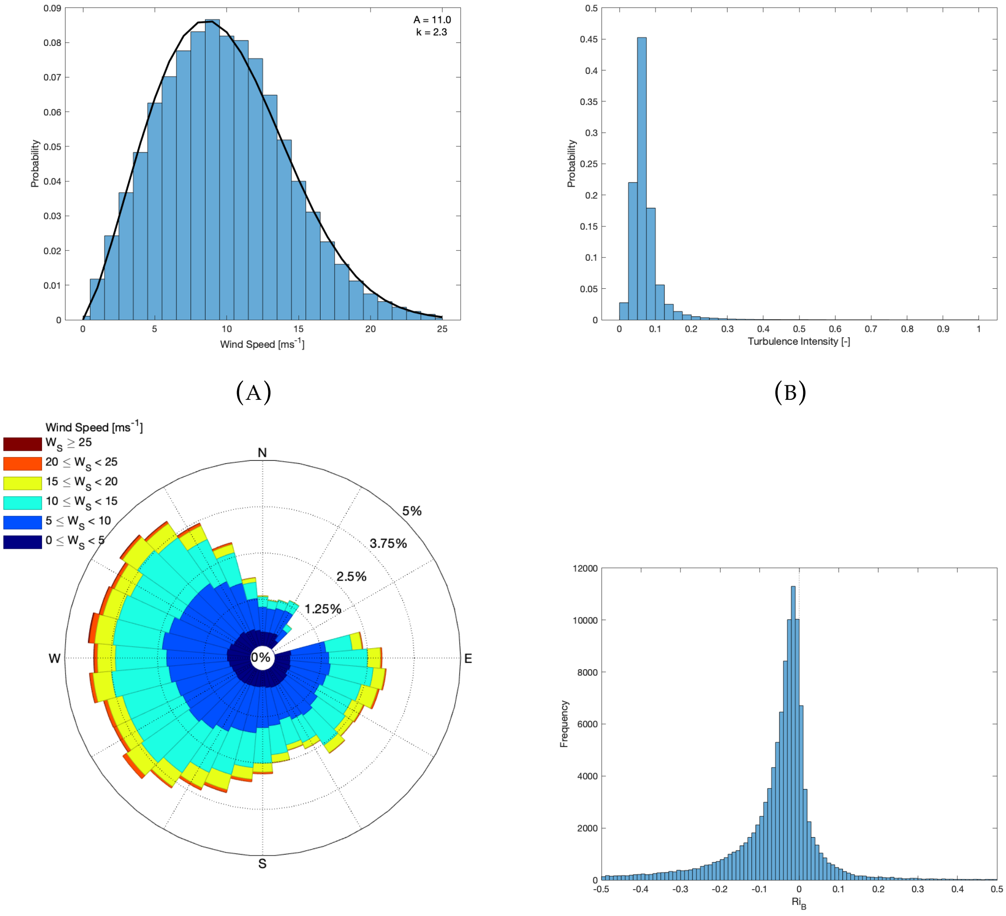

(A)

(B)

(C)

(D)

FIGURE 8.5: The above 4 plots show the wind resource characteristics as determined from measurements at FINO3 at a height of 30m ASL from 2010-2018 (inclusive). (A) Wind speed distribution, (B) Turbulence intensity histogram, (C) Wind rose plot weighted with wind speeds, (D) Richardson number distribution.

Figure 8.6 shows the same wind direction plot with wind speed distribution for that wind direction in each bin, however one plot is presented for each year from 2010-2018. In the first 5 years, there is a spread of less frequent winds which span the remainder of the wind rose (except for approximately [355^o,35^o]). DanTysk begins producing in January 2015, after which point the frequency of E-SE winds above 15 ms^{-1} decrease. This is a logical consequence as DanTysk is constructed to the East of FINO3. SandBank begins producing in January 2017 and is located on the west side of FINO3. The frequence and magnitude of winds from the W-SW decrease after this point, but remain at approximately 3-4%.

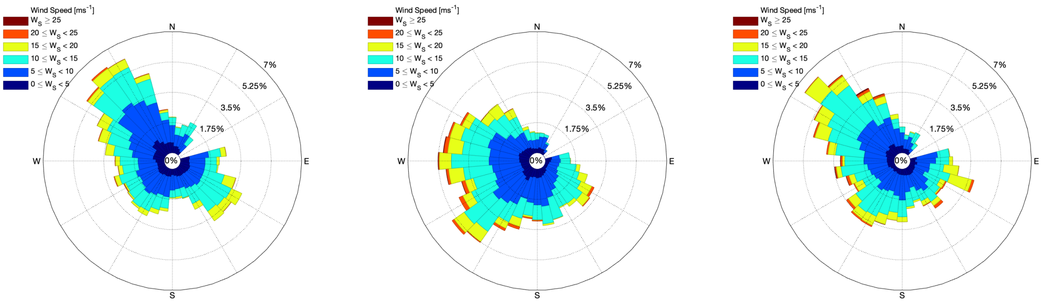

(A) 2010 (B) 2011 (C) 2012

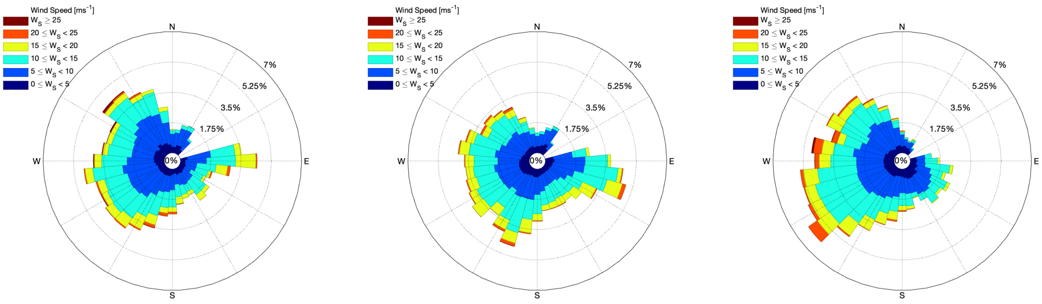

(D) 2013 (E) 2014 (F) 2015

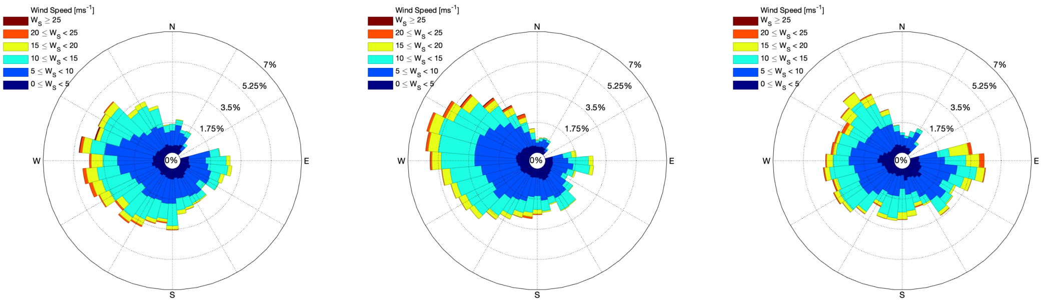

(G) 2016 (H) 2017 (I) 2018

FIGURE 8.6: Wind direction and wind speed distributions for every year from 2010-2018.

Figure 8.7 shows the histogram of data and the Weibull fit curve to the data. It can be seen that each year has good agreement between data and the Weibull fit. The last frame shows the Weibull fit of each year (2010-2018) plotted on the same axes. This shows little spread between all 9 years. In the corner of each frame is printed the data coverage for the data used in the figure for that year.

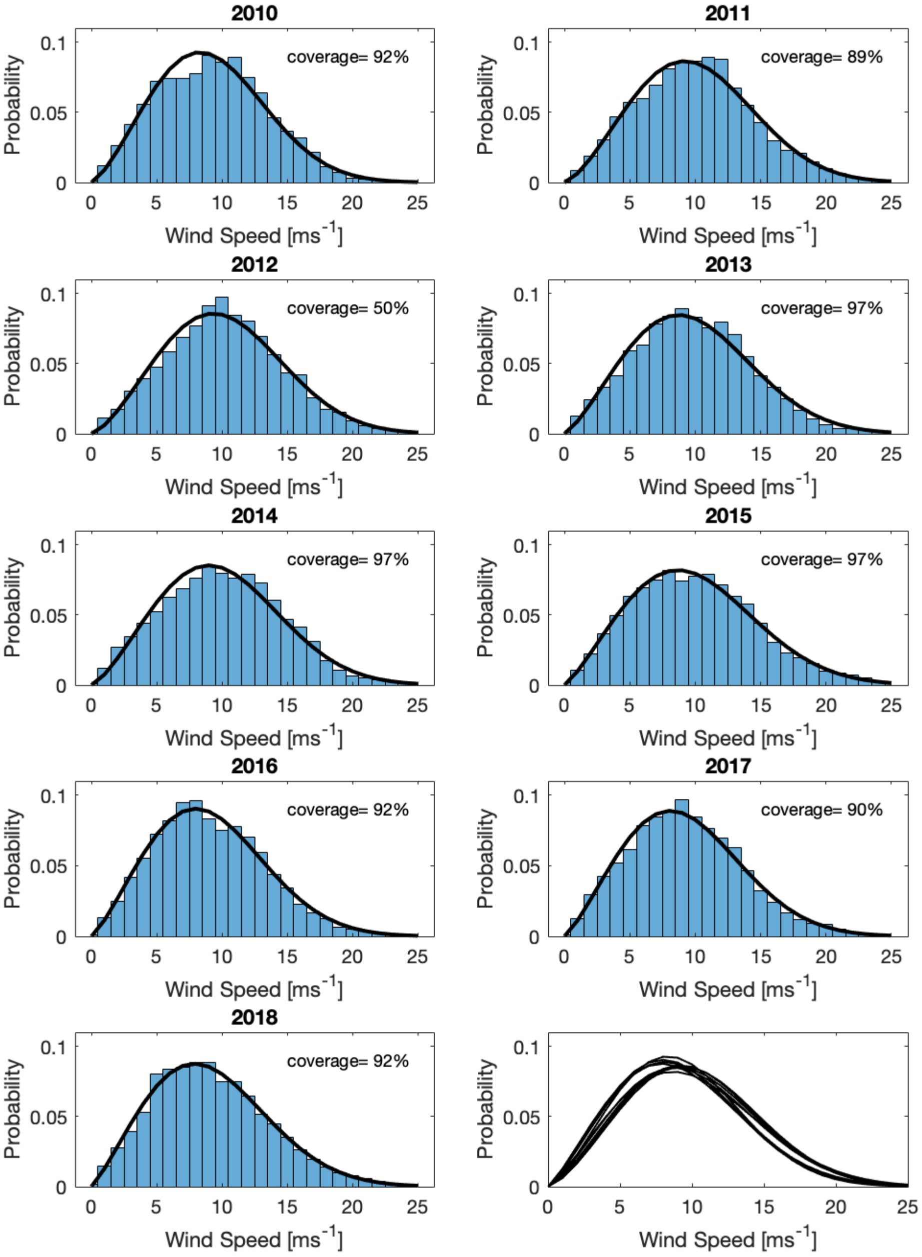

FIGURE 8.7: Long term wind speed distribution

Figure 8.8 shows the distribution of turbulence intensity for each year from 2010-2018. In the upper right corner of each frame is printed the annual mean turbulence intensity in percentage. An increase in annual mean can be seen in 2015, which persists until 2018 (and increases again in 2016). DanTysk began operation in 2015, when a small change in the direction and magnitude of wind speeds was observed. It is possible that this increase in turbulence seen at FINO3 is also due to the operation of the DanTysk Wind farm. The same effect is not seen in 2017 at the completion of SandBank, however this wind farm is approximately 20 km away, whereas FINO3 is on the edge of DanTysk.

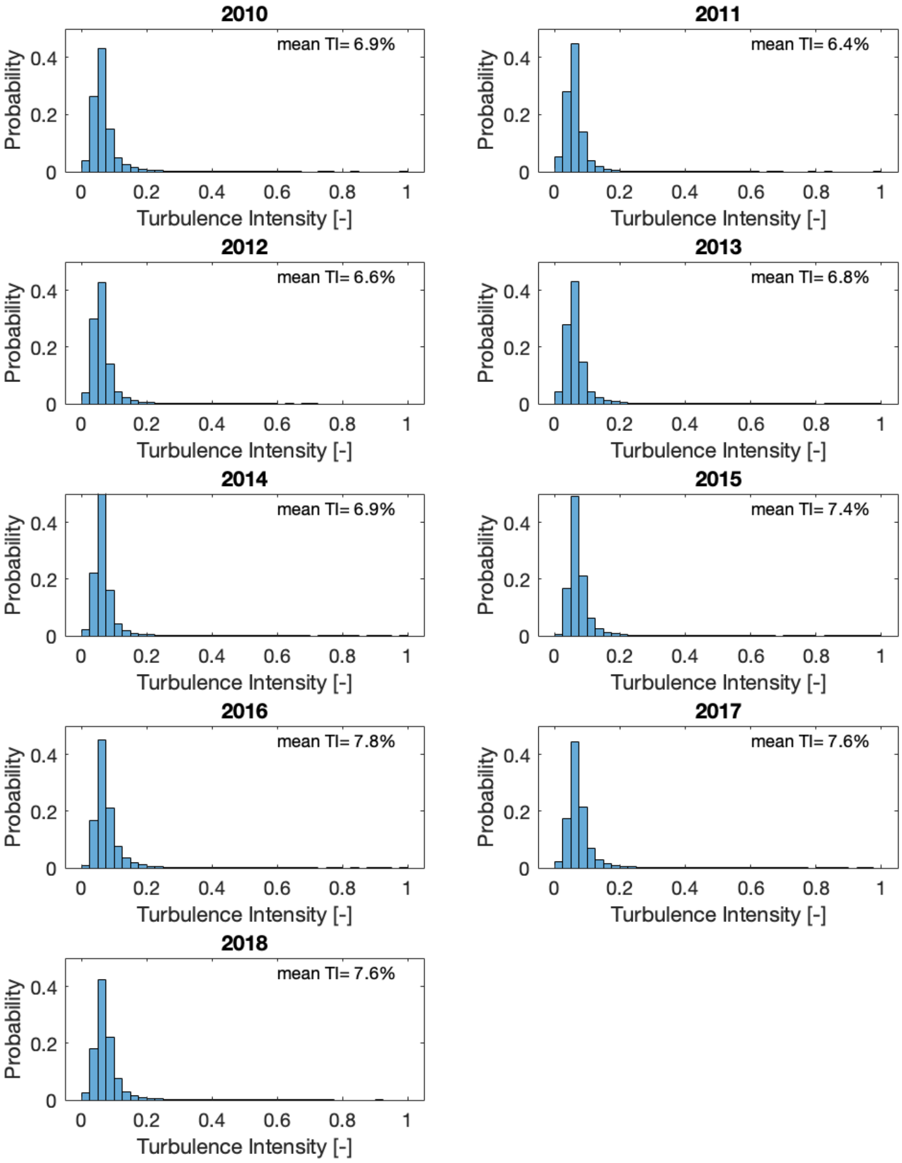

FIGURE 8.8: Long term turbulence intensity distribution

Figure 8.9 shows the distribution of stability classes for each year from 2010-2018. On top of each stacked bar is the data coverage over that year. Years with less than 75% coverage have been shaded to highlight that they are less reliable datasets. Despite the lower coverage of this dataset, a clear trend emerges in the distribution of stability classes. It is typical to see 70-80% of cases in the unstable range. Comparing 2018 to this trend, it may exhibit a slightly lower than average proportion of unstable cases. Looking now to Figure 8.10 the same data is presented but the stratification of stability classes for every month is shown. January and February have very low coverage rates (near 50%) and are thus unreliable. Considering the months with coverage over 75%, a trend of more unstable conditions in the winter months is visible (and comparitively more stable in the summer months). Knowing that the latter 3 months of 2018 are unavailable, it is thus possible that the 2018 data in Figure 8.9 is skewed towards less unstable conditions due to the lack of data from 3 of the typically most unstable months of the year.

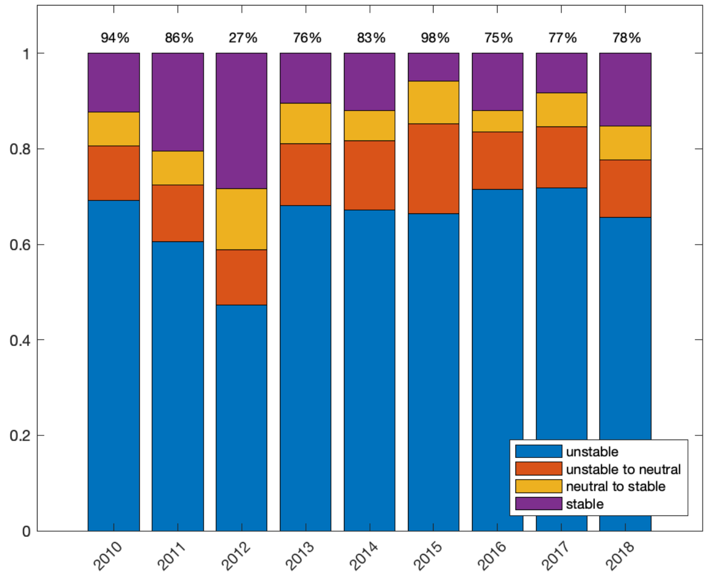

FIGURE 8.9: Distribution of annual stability classes at FINO3 from 2010-2018

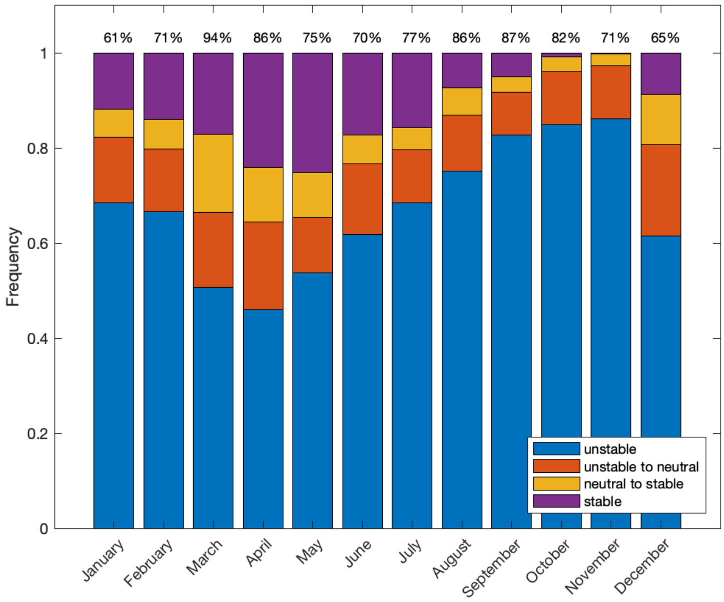

FIGURE 8.10: Distribution of monthly stability classes at FINO3 from 2010-2018

As mentioned above, there are some uncertainties in the FINO3 data, associated with the poor coverage of SST data and the construction of wind farms near the

FINO3 met mast during the measurement period. For this reason, a 13-year period from 2006-2018 has been investigated at Høvsøre. Høvsøre is located on the coast of North-West Jutland, Denmark. Although Høvsøre is an onshore met mast, it lies on a nearly coastal farmland 1.7km from the North Sea and approximately 2m ASL. The roughness lengths surrounding this site are very low, with values in the winter approaching levels of an offshore site [37]. This is why Høvsøre has been considered a suitable comparison for the trends observed st FINO3.

Across the 13 years of data collection, each year boasts over 96% coverage and over 98% data recovery. Figure 8.11 shows the 13-year weibull distribution and histogram of data in blue, overlaid with the same for 2018 in orange. It can be seen that both curves have their peak at the same location, however the 2018 corve is shifted a little to the right. To take a close look at how the 2018 data compares to the other 12 years, Figure 8.12 plots the shape and scale parameters for each annual Weibull distribution. The dashed lines on each frame show the mean value of each parameter over the 13-year period, with a spread of $\pm\sigma$. This shows that 2018 is on the low end of normal for both of these parameters.

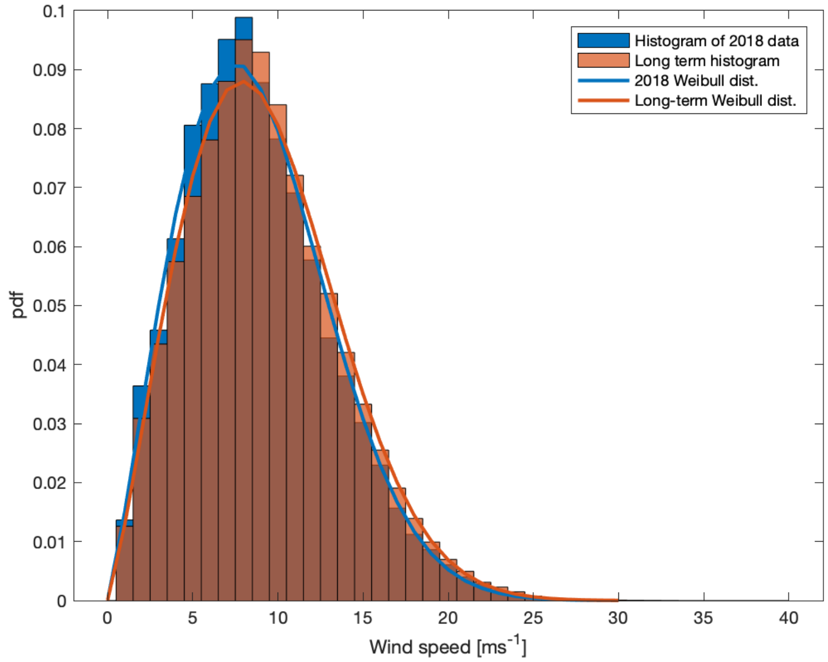

FIGURE 8.11: Long term Weibull distribution versus 2018 Weibull distribution at Høvsøre at a measurement height of 100 m

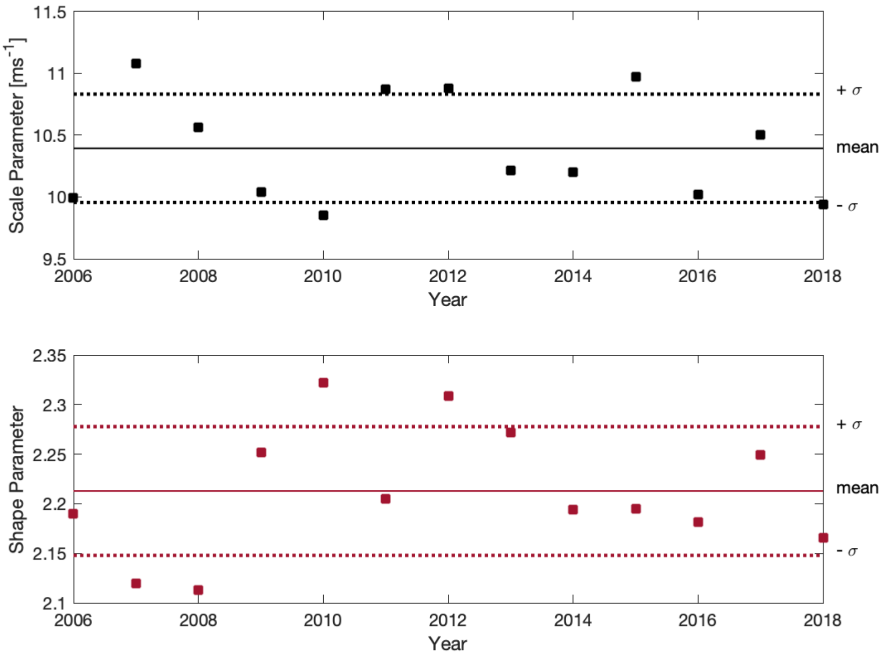

FIGURE 8.12: Høvsøre annual A,k parameters at a measurement height of 100 m

Chapter 9

In-Situ Analysis

This chapter will present an analysis of the SCADA data for SandBank and DanTysk. The purpose of this analysis is to look for possible evidence of a wake effect between the two wind farms. This contributes to the goals of this project and will help steer the analysis of WRF results.

As previously described, this dataset comprises data collected at the turbines in SandBank and Dantysk by the SCADA system, throughout 2018. The measurands used in this analysis include wind speed, measured by a nacelle-mounted annemometer; wind direction, approximated by the nacelle direction; and active power measurements. Figure 9.1 shows the relative agreement of the nacelle direction with actual wind direction measurements. The data shown is of the DanTysk turbine closest to the FINO3 met mast against a wind direction measurement taken at a 61m height at FINO3.

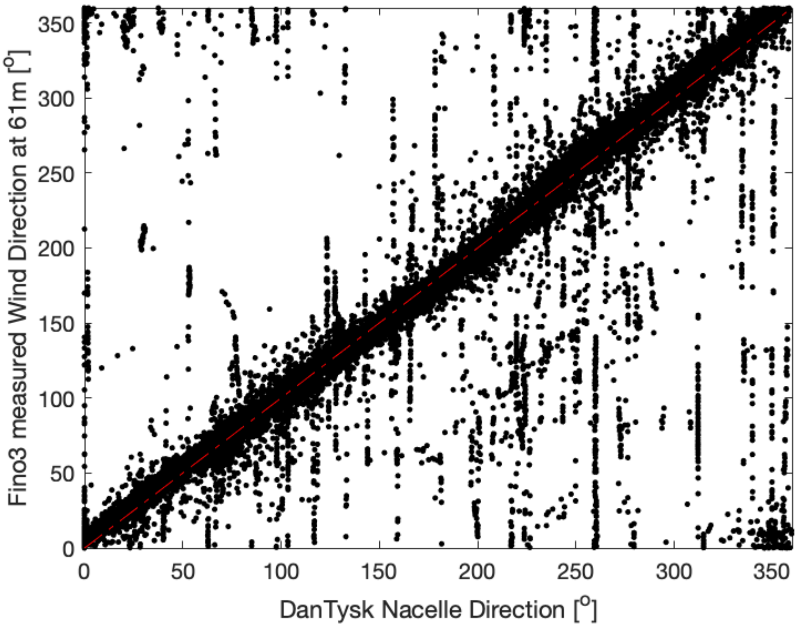

FIGURE 9.1: Comparison of Nacelle angle measurement with FINO3 wind direction measurement at 61m, y=x is plotted in red for reference

The data have been pre-processed by Vattenfall before being recieved by the OffshoreWake project. Nevertheless, pre-processing was conducted again in order to better understand the dataset and to remove any erroneous data. It was seen that there is a large gap in late August where all turbines across both wind farms were not producing any power for approximately ten days. There are also sporatic instances of a single turbine producing no power for a number of days. There are eight particular turbines in the DanTysk wind farm which had sustained periods of no production for approximately two months each. This is reflected in the turbine-wise plot of annual availability of active power measurements (Figure 9.2) as a few turbines have much lower availability than their neighbouring turbines. The annual availability of active power data for each wind farm is nearly identical, at approxiamtely 87.8% and 87.4% for SandBank and DanTysk, respectively.

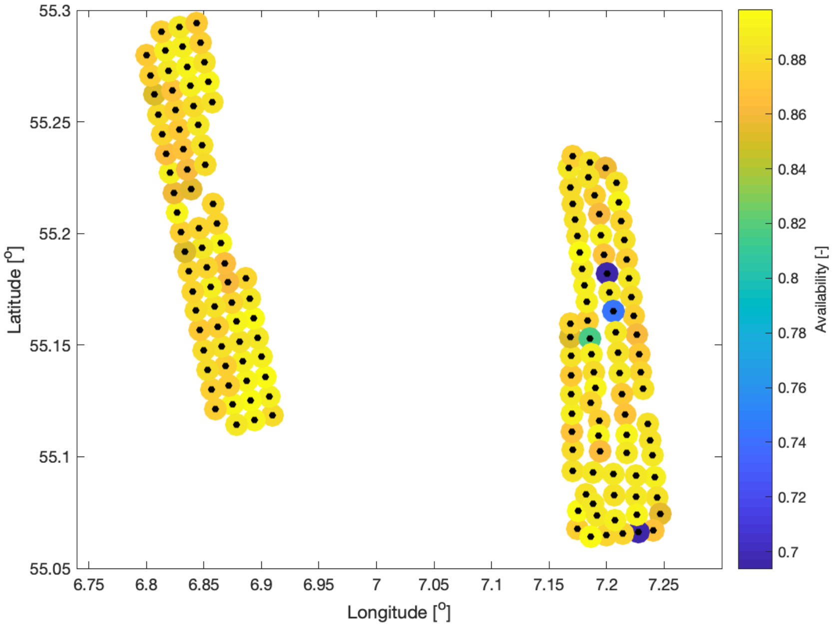

FIGURE 9.2: Annual turbine-wise availability of active power measurements

When comparing the data at SandBank and DanTysk, it is important to keep a few of the physical characteristics of the wind farms in mind. The total installed capacity of each wind farm is exactly the same (288 MW) therefore the total power produced by each wind farm can be directly compared. However, SandBank has 72 4.0 MW turbines whereas DanTysk has 80 3.6 MW turbines, therefore capacity factor has been used to quantify turbine productivity, where possible. On account of the respective wind farm areas and turbine sizes, SandBank has a marginally higher power density of 6.1 Wm^{-2}, compared to DanTysk's 4.4 Wm^{-2}. This could affect the relative strength of the wake of each wind farm, with the wake from DanTysk being weaker than SandBank (strictly from a power density point of view). Finally, the likely influence of one of these wind farms on the other is highly directional. Based on the relative positions of the wind farms and the layout of each, it is expected that east-southeasterly winds will place SandBank in the wake of DanTysk. Conversely, west-northwesterly winds are likely to see DanTysk in the wake of SandBank. Both wind farms should be free from the other's shadow during northerly or southerly winds. The climatological analysis revealed that this site experiences winds from all directions and thus is will be important to consider wind direction in a wake characterization.

Looking first at annual power production, the annual mean capacity factor for each turbine is illustrated in Figure 9.3. SandBank generally exhibits higher mean capacity factors, with its highest values at the North, West and South edges of the wind farm layout. These turbines are more productive than any of the turbines in DanTysk. The general higher productivity of SandBank comapred to DanTysk could be due to any of many factors. The wind farm is further offshore, and could naturally experience higher wind speeds due to coastal gradients. Recalling the wind rose for this site (Figure 8.1), the highest magnitude winds tend to come from the west-northwest and there are often winds in this sector. The turbines at SandBank could be more optimal for the wind conditions, or the wake shadow from SandBank on DanTysk could be impacting the power output of the wind farm. Further information is required to determine the cause, however this analysis confirms that there is a difference in performance of these adjacent wind farms.

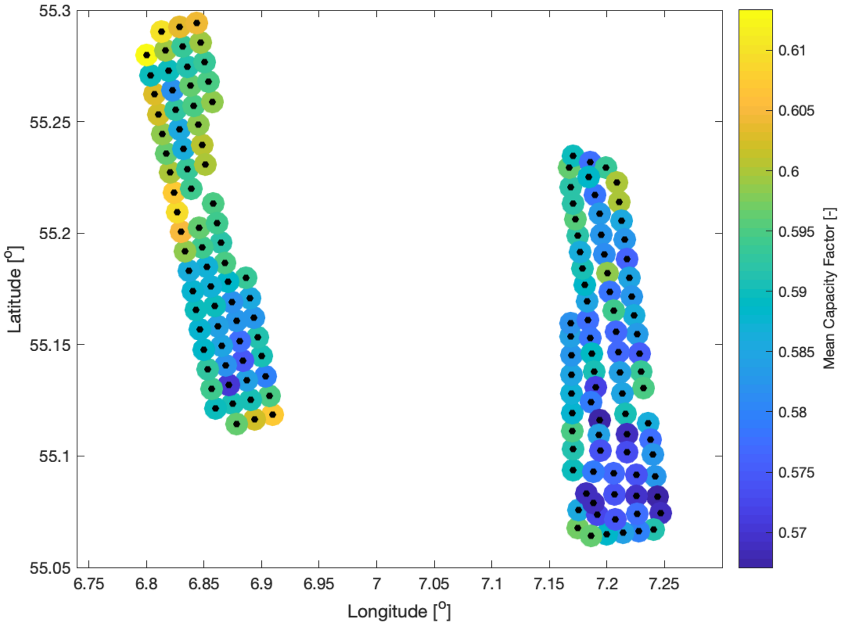

FIGURE 9.3: Annual mean capacity factor for each turbine in SandBank and DanTysk

Looking at the annual mean wind speed distribution (Figure 9.4), there is no evidence that there is a coastal gradient which blows stronger winds upon SandBank. This plot of course shows the wind speed measured within the wind farm and is also a mean quantity over the whole year. Some seasonal and diurnal behaviour is washed away by taking an average over the entire annual period.

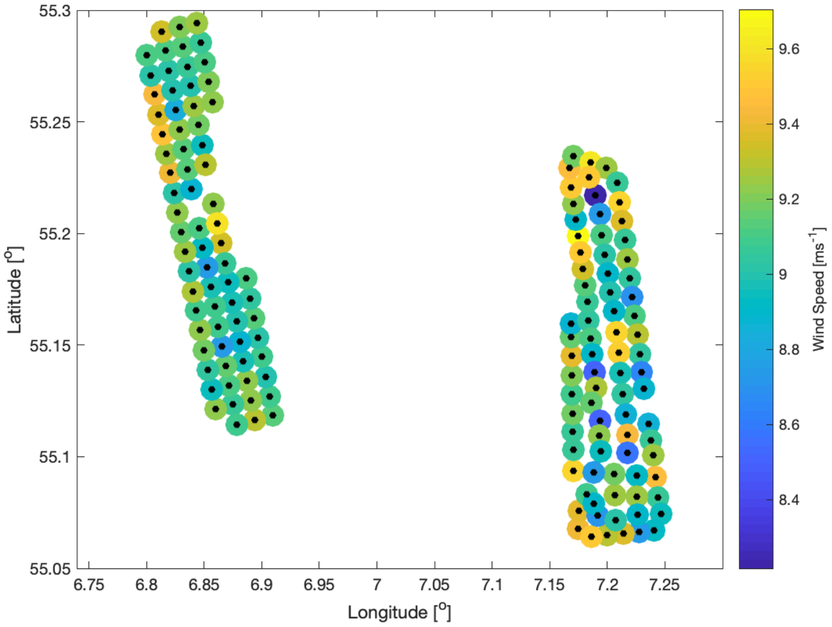

FIGURE 9.4: Annual mean wind speed considering all prevailing wind directions

Figre 9.5 depitcts the annual mean wind speed distribution for wind directions coming from the south-southeast. The magnitude of wind speed is relatively constant from east to west over both wind farms, which suggests that there is no coastal gradient acting on these wind farms in this range of wind directions. This range of wind speeds occurred approximateld 7% of the year are characterized by mid-range wind speeds. Looking to the plot of capacity factors for this same wind direction bin (Figure 9.6), there is clear evidence of an internal wind farm wake. The southern wind turbines of both wind farms see mean wind speeds over 10 ms^{-1} with corresponding capacity factors over 65%. Although a few turbines are performing very well, the wind is flowing across the wind farms in their least efficient direction according to the wind farm layout. As a results, the internal wake effect is evident in this sample of the data as the northern turbines get progressively darker in color.

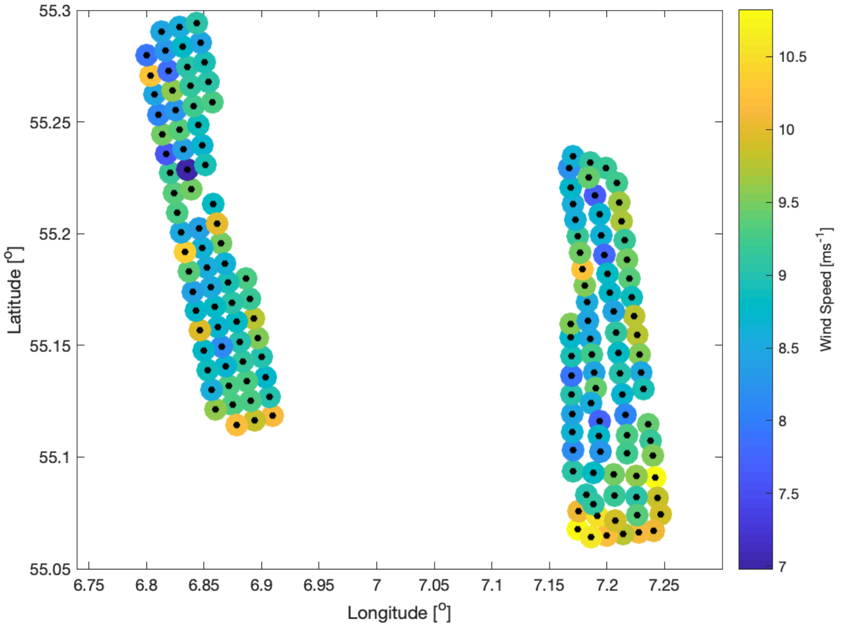

FIGURE 9.5: Annual mean wind speed for prevailing winds between 150 and 180^o

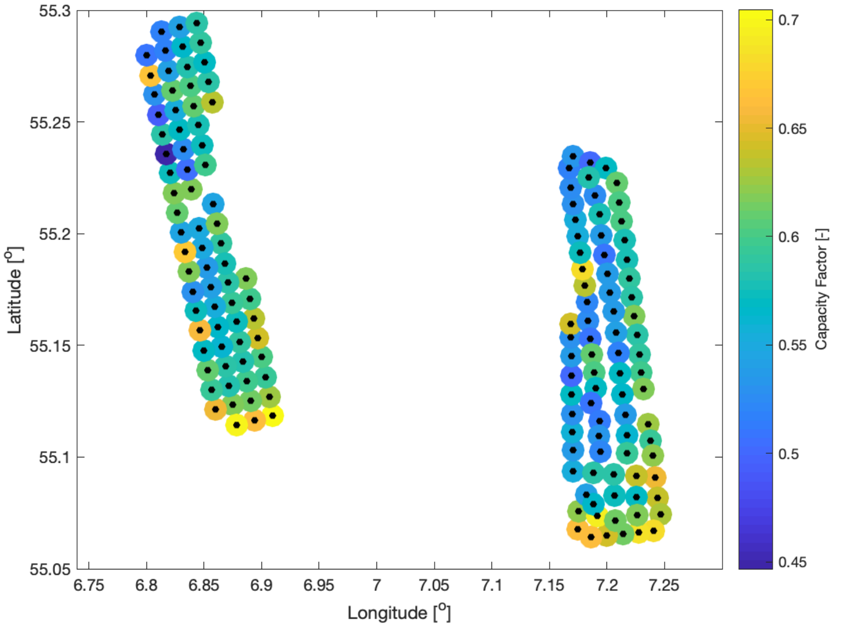

FIGURE 9.6: Annual mean turbine capacity factor for prevailing winds between 150 and 180^o

Figure 9.7 depicts the first evidence of a possible wind farm wake effect. This subset of the annual data comprises easterly winds from 60 to 90^o. The reader should imagine winds passing by the northen tip of DanTysk at an angle of 60^o to see that the southern tip of SandBank will be in path of the wake behind DanTysk. Indeed, the data agrees with this thought experiment. The mean wind speeds are highest along the east side of DanTysk and along the north east side of SandBank. There are few explainations for the wind speed reduction at the southern end of SandBank save a wake effect. The spatial distribution of capacity factor agrees with with the wind speed data, presenting a clear gradient of decreasing capacity factor towards the south end of SandBank. DanTysk also exhibits some exidence of internal wake effects at the southwest corner of the wind farm, with decreased wind speeds and capacity factor. This wind direction bin shows good agreement between wind speed and power data as an indicator of the presence of wake effects. It shold be noted that this wind direction occurred during approximately 8% of the 2018 data.

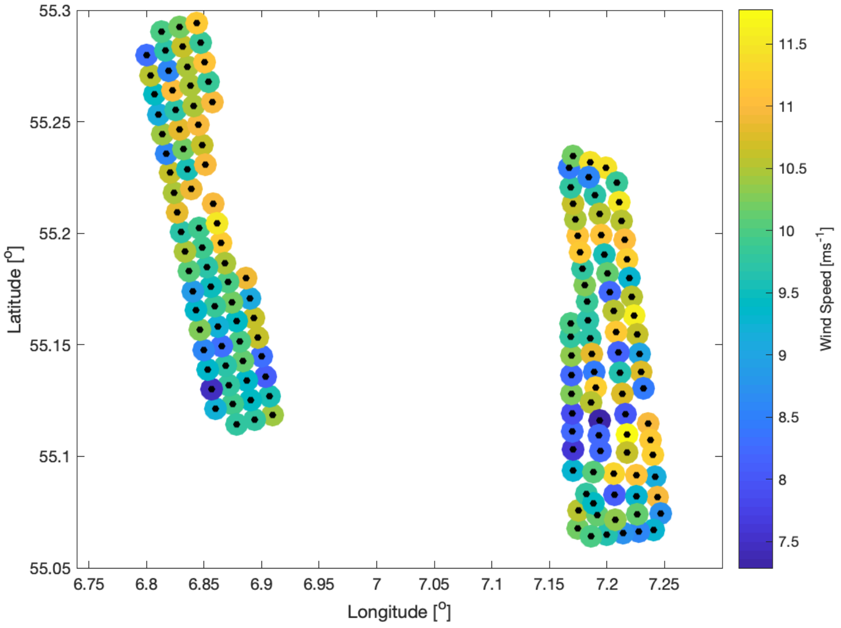

FIGURE 9.7: Annual mean wind speed for prevailing winds between 60 and 90^o

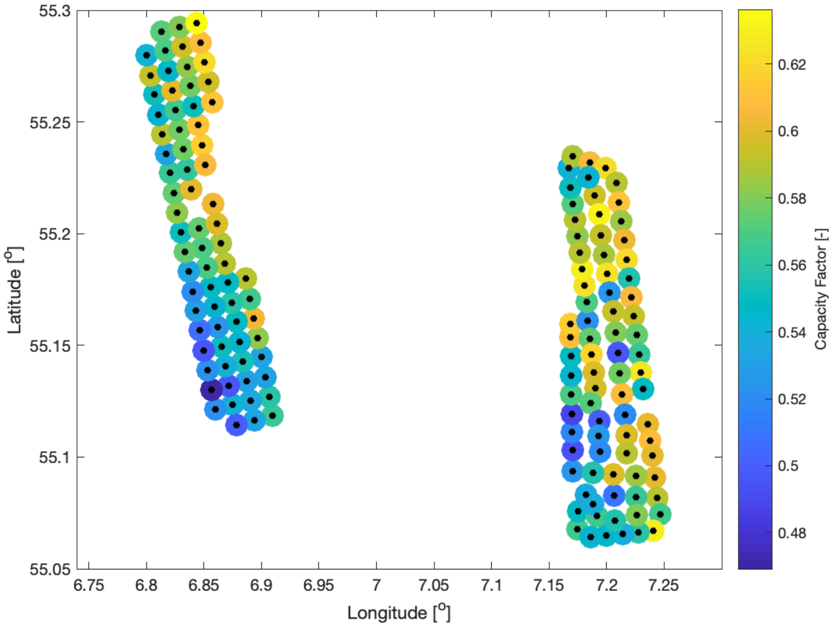

FIGURE 9.8: Annual mean capacity factor for prevailing winds between 60 and 90^o

Figure 9.9 illustrates a wake effect which acts in the opposite direction, compared to the previous figure. A prevailing westerly wind occurring approximately 12% of the time is the most frequently occurring wind direction. The wind speeds are unexpected here, as the upwind wind farm, SandBank, has consistently lower wind speeds than the supposed waked wind farm, DanTysk. Recall that the wind speed and capacity factor results from 60-90^o showed strong agreement among both metrics. This case is quite the opposite. Figure 9.10 illustates a plausible wind farm wake scenario, where the west side of Sandbank performs well, as does the southwest corner of DanTysk. The region of DanTysk in the shadow of SandBank presents with decreased capacity factors, consistent with being in its shadow.

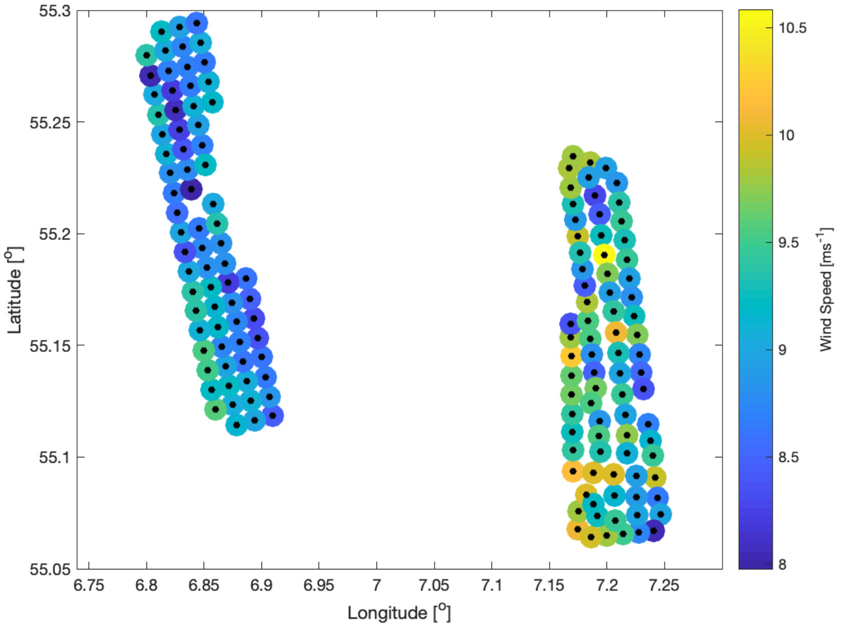

FIGURE 9.9: Annual mean wind speed for prevailing winds between 240 and 270°

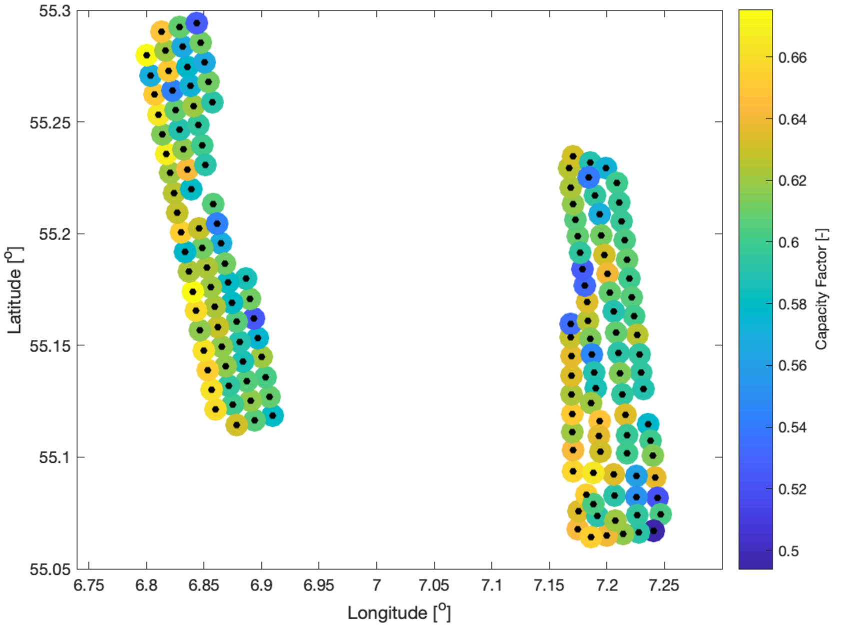

FIGURE 9.10: Annual mean capacity factor for prevailing winds between 240 and 270°

The results presented in this section suggest that a wind farm wake scenario is plausible at this location, particularly for easterly winds. It is possible that wind farm wakes could also occur for westerly winds, however further evidence is required.

Chapter 10

WRF Validation

To determine the accuracy of the WRF simulations compared to the actual behaviour at the subject wind farms, a validation study has been conducted. For the purposes of comparison, the time periods of each dataset have been trimmed to match one another. This results in data spanning 1 Jan 2018 to 4 December 2018, with a few short gaps throughout the year. WRF assumes all turbines to be operating at full capacity at all times, therefore an effort has been made to scale the WRF outputs to mirror the lower availability seen in the SCADA data. For negative or 0 values of POWER, WS or WD in the SCADA data, the value in both SCADA and WRF is set to NaN. This is done on a turbine-basis, for every time step. There may be cases of turbines in the measured data which are operating at a low (but not null) capacity, however that can not be determined from the data available in this study.

For this validation, comparisons are made between the measured and simulated power outputs, and the measured and simulated wind speeds. Results of wind direction and turbulence intensity have not been presented in this section but are presented in Chapter 8.

Figure 10.1 shows the monthy mean wind speed over the entire wind farm for both WFP and the SCADA data. The upper frame of the figure shows results for SandBank and the lower frame presents results for DanTysk. It can be seen that there is good agreement in the general trend of the data. The mean wind speeds for both wind farms, and all curves, show a tendency for higher wind speeds in the winter and lower wind speeds in the summer months. The range of wind speed values is generally the same for both wind farms. For both wind farms, it can also be seen that the SCADA data reports the highest wind speeds in the winter months, while it has the lowest values in the summer months. Comparing the two WFP schemes, EWP consistently reports higher wind speeds than Fitch (for both wind farms).

TABLE 10.1: Annual mean wind speed bias in [ms^{-1}]

WFP scheme	SandBank	DanTysk
EWP	+ 0.18	+ 0.16
FITCH	-0.19	- 0.22

TABLE 10.2: Annual mean power bias in [GW]

WFP scheme	SandBank	DanTysk
EWP	+ 46	+ 34
FITCH	- 11	- 19

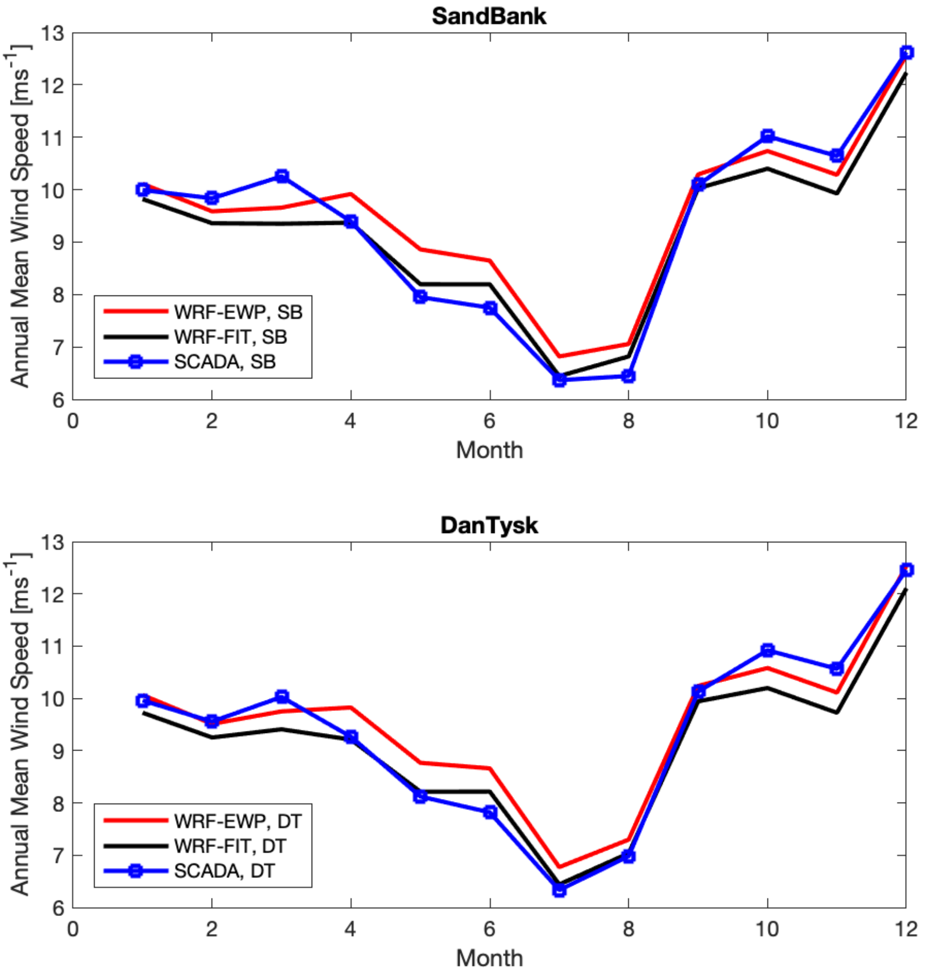

FIGURE 10.1: Monthly comparison of mean wind speed between measurements and simulations. SCADA data is measured at hib height and WFP data is extracted at 89 m height.

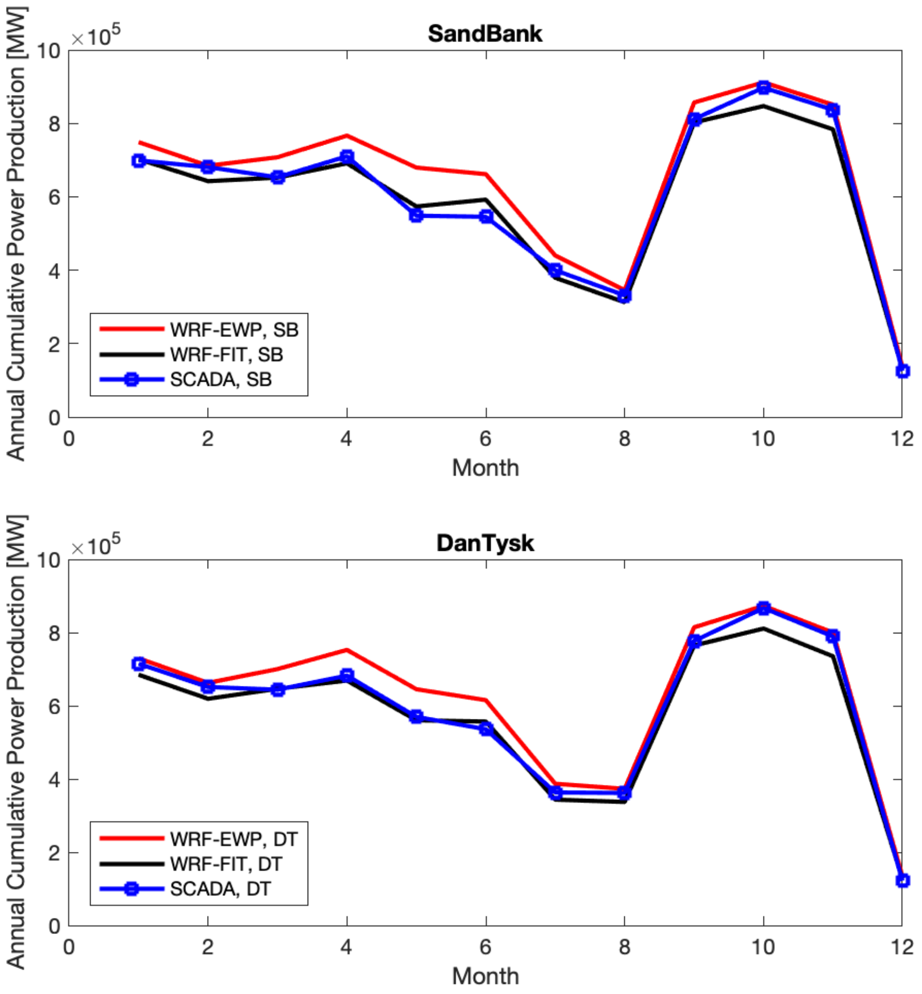

FIGURE 10.2: Monthly comparison of cumulative power production

In a 2017 validation study comparing a 4-day WRF simulation using the Fitch scheme to measurements, Lee and Lundquist [18] found a correlation between power bias and wind speed bias, but not between power and wind direction or TKE. A similar analysis is conducted, with results for power bias as a function of wind speed bias presented in Figure 10.3. Here, the average power bias for each time step is plotted against the average wind speed bias for each time step. It can be seen that generally, as the wind speed bias approaches 0, so too does the power bias. However, the present results differ from those of Lee and Lundquist as there are a portion of cases which have a near 0 wind speed bias yet have a large, negative power bias. These deviations are only seen for a negative power bias, meaning the measured power is lower than the simulated power. It is likely that many of these cases are situations in which the turbines are operating at low capacity, but the measurements are reporting some power (perhaps a fraction of a MW). As the turbines simulated in WRF always operate at full capacity, the bias in these cases would produce a negative bias which is a function of a poor data comparison and not necessarity an indication of poor WFP performance.

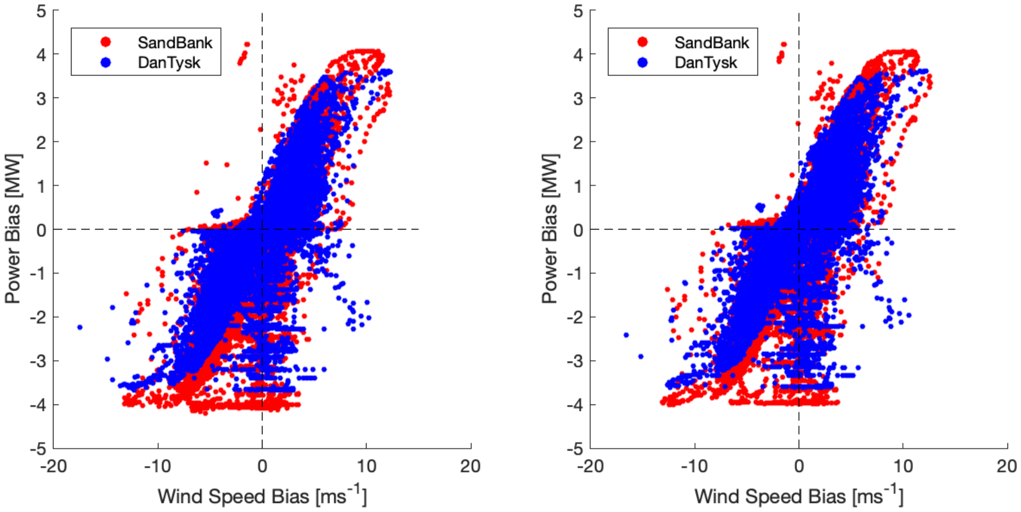

(A) Bias for EWP simulation (B) Bias for Fitch simulation

FIGURE 10.3: WS and Power bias relation

Chapter 11

WRF Wake Analysis

This chapter will discuss the wake behaviour findings from the WRF simulations. This analysis includes all of the simulation results, which is slightly different from the results presented in the WRF validation section. The reader is reminded that the availability of SCADA data is approximately 86%, largely due to missing most of the month of December. There is one hole in the WRF simulation results. The Fitch scheme was unable to simulate 24 January 2018, which has resulted in a 1.5 day period which has been omitted from all simulations. This is the only gap in the simulation data and can be expressed by a data availability of 99.6%. In many cases in this section, a mean quantity is taken over the simulation domain. Unless otherwise stated, all values are reported at 89 m ASL (a representative hub height for SandBank and DanTysk).

11.1 Climatology

This section describes the climatology determined from the WRF simulation results. The grid cell in which FINO3 is located is chosen as the point at which to report the climatology from the simulation results. This aligns with the earlier analysis of the climatological conditions at FINO3. The statistics presented herein are taken at a height of 55 m ASL and the measurements at FINO3 were taken at a height of 61m.

Figure 11.1a shows the histogram of wind speeds and the Weibull distribution fit to this data, from both the EWP and Fitch simulations. The figure indicates very good agreement between the two schemes. The Fitch scheme simulates slightly more wind speeds less than 7 ms^{-1}, and EWP has marginally more occurrences of higher wind speeds, these differences are however impreceptible between the wind rose plot for each scheme (Figure 11.1c and 11.1d). The agreement of wind speed and direction distributions between the two schemes is to be expected, as both use the same driving reanalysis dataset. For reference, the measurements at FINO3 for 2018 fit to a Weibull distribution with scale parameter $A = 10.4ms^{-}1$ and shape parameter $k = 2.2$. On this basis, the WRF results for both simulations are in good agreement with the FINO3 data, especially considering the shorter dataset in the FINO3 measurements.

The results for the no-WFP simulation are pitcured in Figures 11.1b and 11.1e. Both show higher wind speeds than the WRF results. These results also exhibit the expected trend, as the wind speeds increase when the surrounding drag devices (wind turbines) are removed from the simulation. The fitted A and k at FINO3 for 2018 are not a relevant comparison in this case, however the a comparison with a year before the wind farms were constructed would be a reasonable comparison. Table 11.1 reports the Weibull fit parameters from 2010-2018, and it can be seen that before the construction of SandBank and DanTysk (before 2015), the mean wind speeds were higher, characterized by a difference in scale parameter of up to 1.1 ms^{-1} compared to 2018. The long term climatological at Høvsøre indicates that 2014 is the most similar to 2018 (of the years available), in terms of wind speed. The overprediction of annual mean wind speed at FINO3 is approximately 0.3 ms^{-1} compared to the 2014 data.

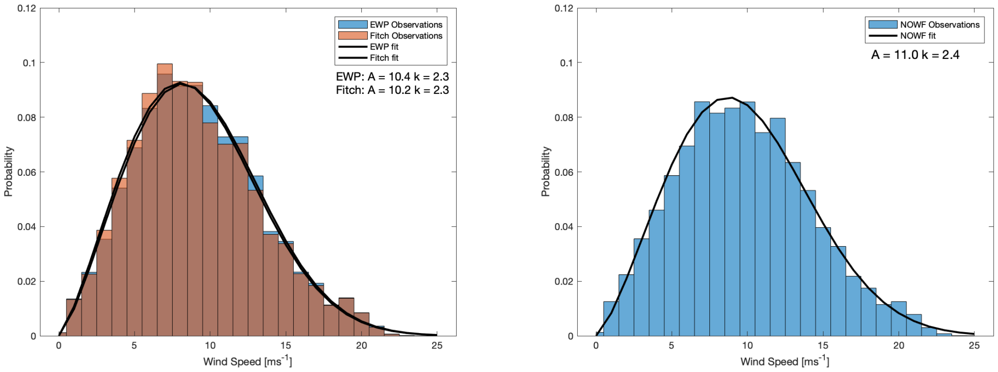

(A) EWP and Fitch (B) No WFP

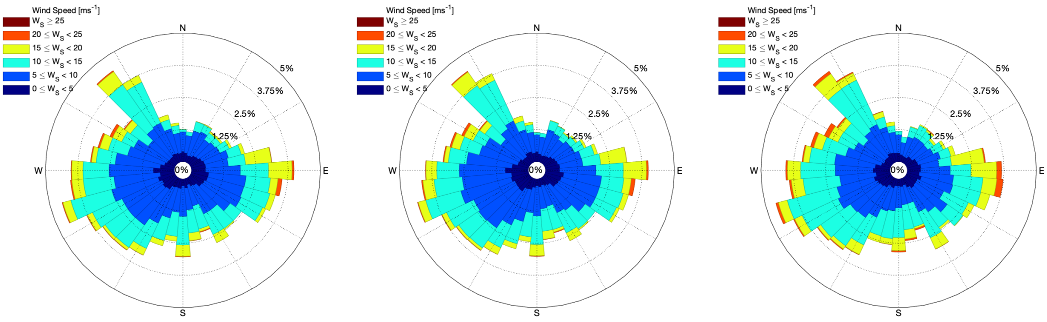

(C) EWP (D) Fitch (E) No WFP

FIGURE 11.1: WRF climatology at representative hub height for 2018

TABLE 11.1: Weibull fit parameters for long-term FINO3 measurements at height 61 m ASL

	2010	2011	2012	2013	2014	2015	2016	2017	2018
A [ms^{-1}]	10.5	11.4	11.6	11.2	11.3	11.3	10.3	10.5	10.4
k	2.4	2.4	2.4	2.3	2.4	2.2	2.3	2.3	2.2

11.2 Wind Speed Visualization

It can be challenging to interprert the trends in data from such a long dataset as in the current study. This analysis will therefore begin by simply examining the mean wind speed profiles over the inner most simulation domain (domain 3). Figure 11.2 presents the monthly average wind speed distribution over the domain. The reader is reminded to look at the colorbar as it changes for each subfigure. The left figure in each row depicts the results from the EWP simulation and the right figure depicts the Fitch scheme.

The results agree with the above climatological analysis, consistently showing mean wind speeds around 9 and 10 ms^{-1}. In autumn months (September through December), the wind speeds are relatively consistent over the entire domain, and higher than average. In October and November, a coastal gradient can be observed, from the west Danish coast and the north German coast. The winds slow in the summer, reaching their lowest speeds in July and August.

All of the parameterized wind turbines can be clearly seen in these plots, as spots of sharp decreases in wind speed. The decrease in wind speed is consistently greater for the Fitch scheme than for the EWP scheme. There are, however no classical visualization of wakes (as a trail behind the wind farm) visible in these plots. This is because of the directional dependence of wakes. These figures have averaged each grid gell in time, over a one-month period. As the previous climatological studies have shown, this site sees prevailing winds from nearly all directions. As a result, the presence of wakes in different directions over the course of the month effectively cancel one another out of the monthly mean spatial plots.

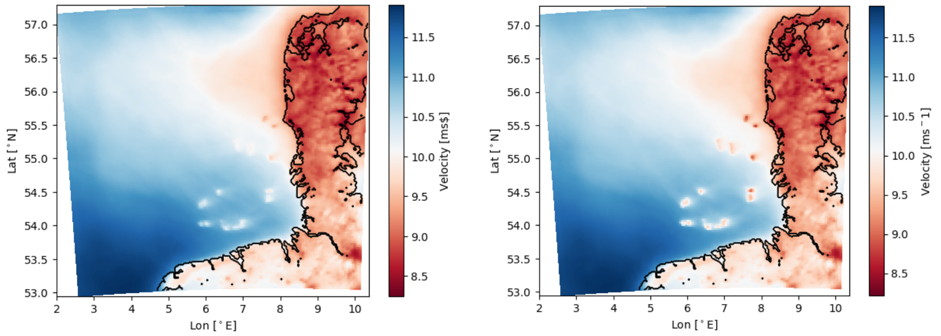

(A) EWP - January

(B) Fitch - January

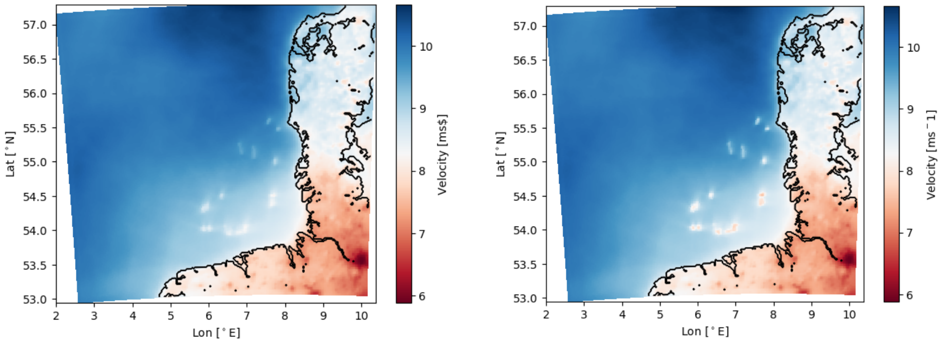

(C) EWP - February

(D) Fitch - February

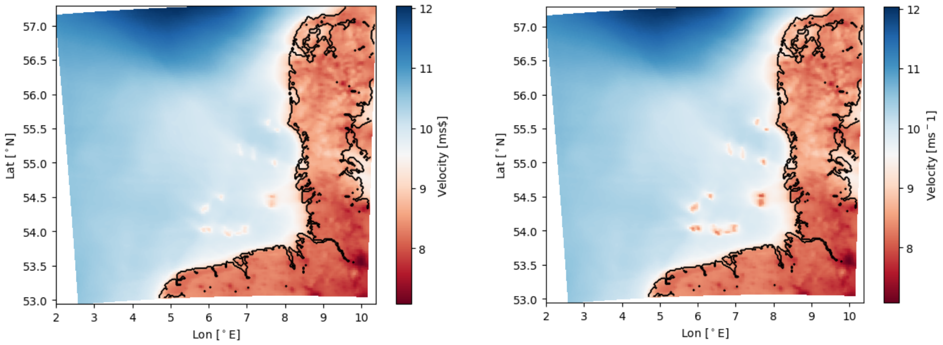

(E) EWP - March

(F) Fitch - March

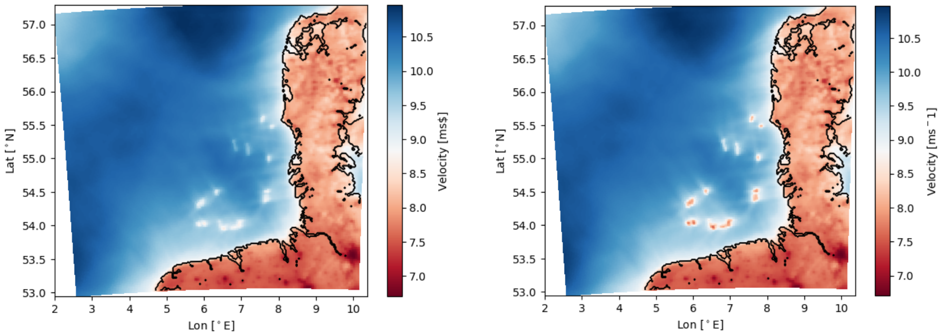

(G) EWP - April

(H) Fitch - April

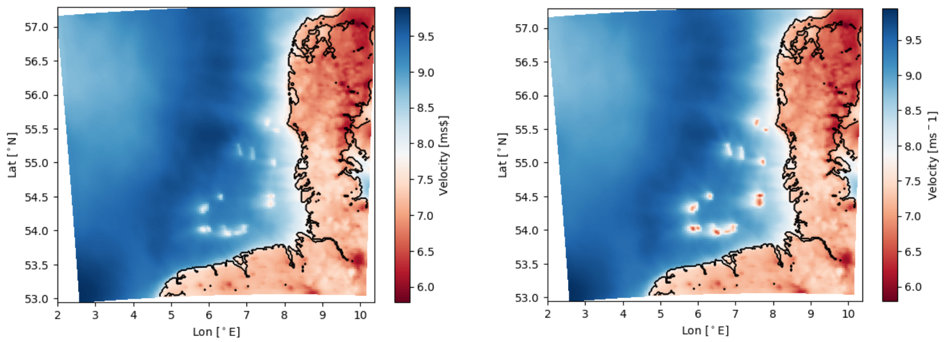

(I) EWP - May

(J) Fitch - May

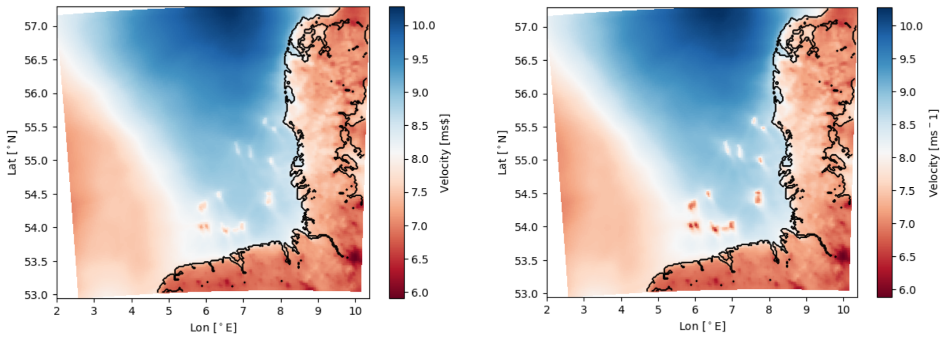

(K) EWP - June

(L) Fitch - June

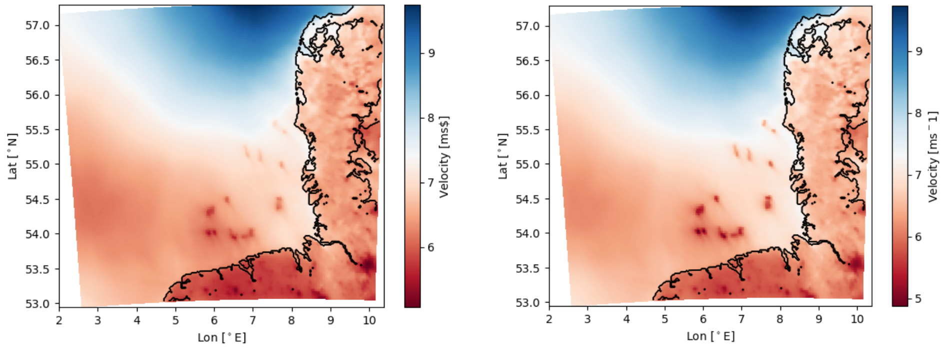

(M) EWP - July

(N) Fitch - July

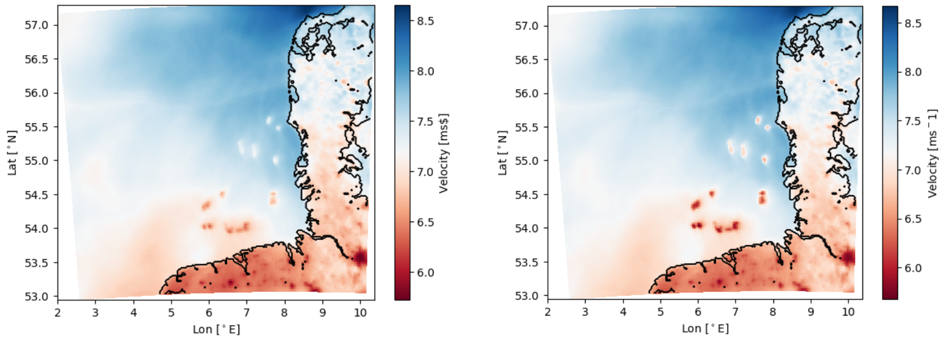

(O) EWP - August

(P) Fitch - August

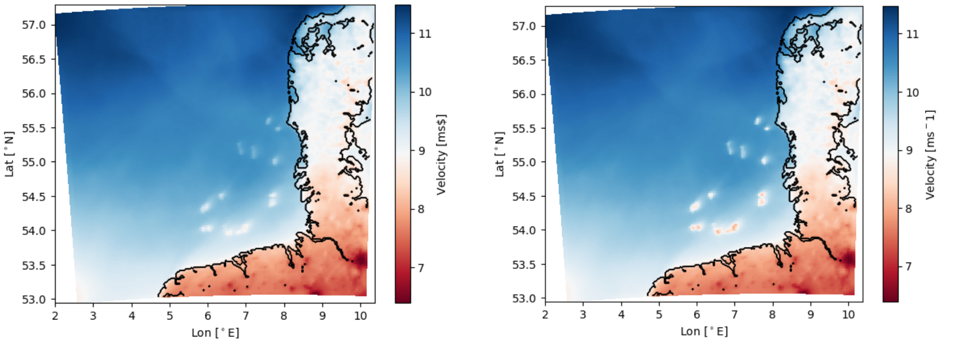

(Q) EWP - September (R) Fitch - September

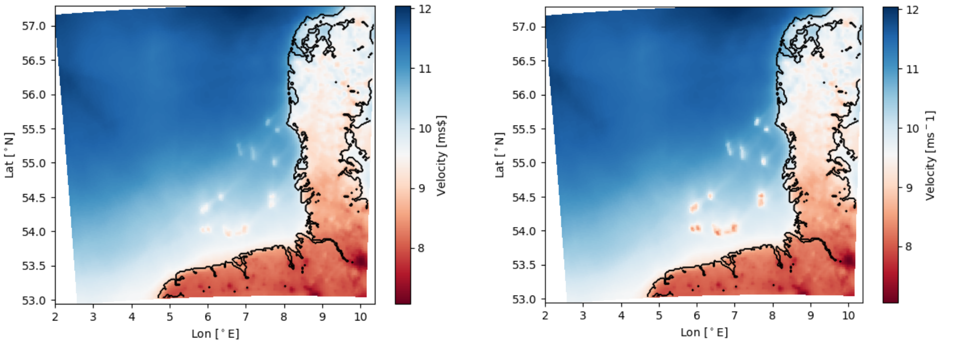

(S) EWP - October (T) Fitch - October

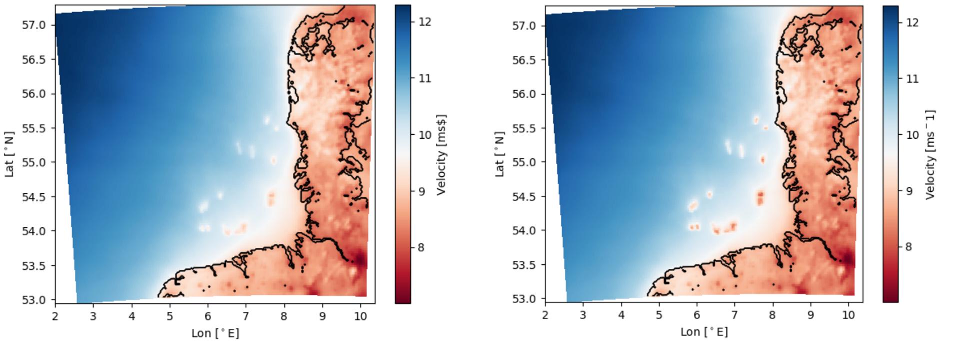

(U) EWP - November (V) Fitch - November

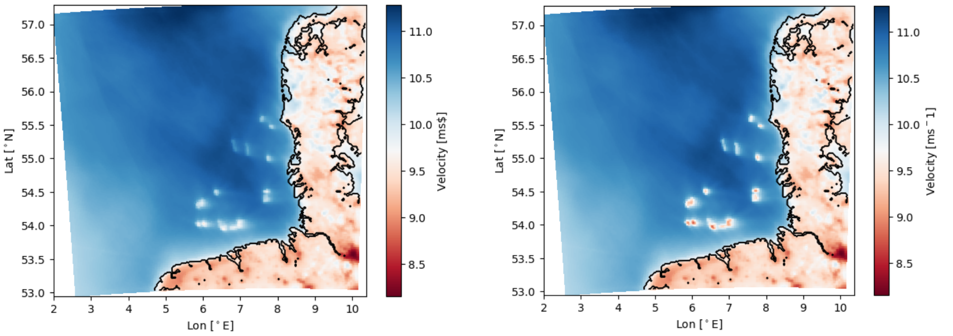

(W) EWP - December (X) Fitch - December

FIGURE 11.2: Monthy mean velocity profiles for EWP and Fitch schemes

11.3 Velocity Deficit

The velocity deficit (VD) is typically defined as the difference between the undisturbed wind speed and the affected flow, typically expressed as percentage of the ambient wind speed [24]. This expression is given in Equation 11.1. In this analysis, WS_{WFP} is the wind speed from simulations from either the EWP or Fitch scheme, and WS_{NOWF} is the ambient condition obtained from the no-WFP simulation. By conducting teo idential simulations, and reporting a velocity deficit, the background flow should be effectively removed and the wakes clearly visible when present.

Figure 11.3 depicts the monthly mean wind speed deficit for the EWP and Fitch schemes. The velocity deficits clearly indicate the wind farm locations in the figures. The deficits tend to be stronger in the spring time (April to June), compared to the other seasons. In these months, the region of velocity deficit grows in area immediately surrounding the wind farms. These months of higher velocity deficit correspond to the months with generally lower mean wind speeds. This will be considered in later analysis. It can be noted once again that few wake paths are visible in this figure. It is clear that the dependance of wakes on prevailing wind direction will need to be considered.

The reader will notice high positive velocity deficit values in the open ocean regions of the domain for some months. Specifically, January, May and June. These positive deficits generally do not exceed the magnitude of the velocity deficit in the wake. However in June, a large positive deficit is seen over a large portion of the open ocean. It is expected that these are the results of unsteady flows across the domain, which are unlikely to be syncronized between the WFP and No-WFP simulations. This leads to momentarily high reported values of velocity deficit, which can skew the monthly mean flow higher. While the author does not completely understand the cause for these large differences in the ambient and parameterized flow, these positive deficits can be up to 20% (roughly 2 ms^{-1}).

$$VD = 100\% * \frac{(WS_{WFP} - WS_{NOWF})}{WS_{NOWF}} \tag{11.1}$$

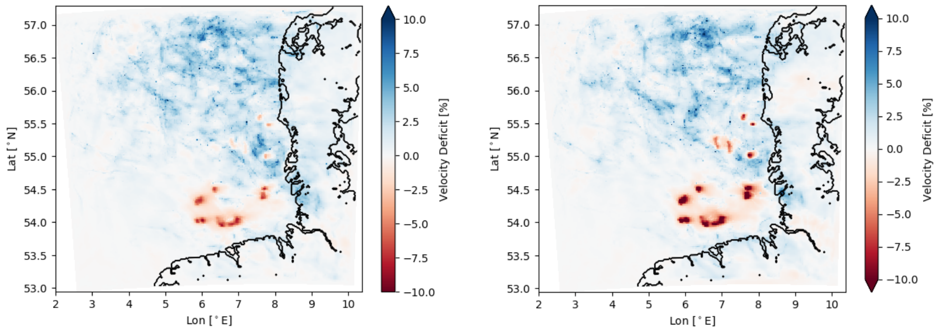

(A) EWP - January (B) Fitch - January

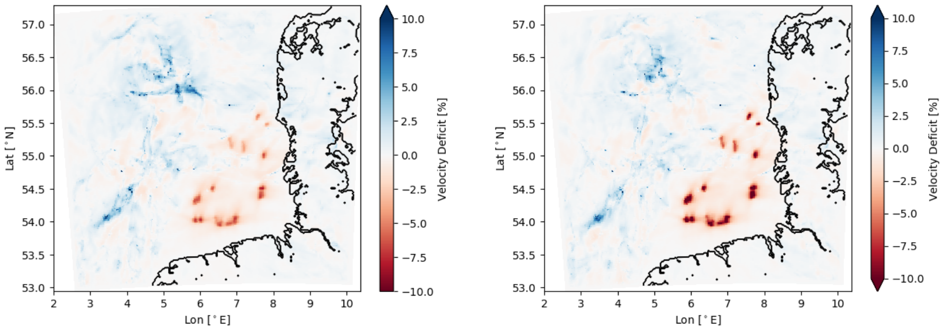

(C) EWP - February (D) Fitch - February

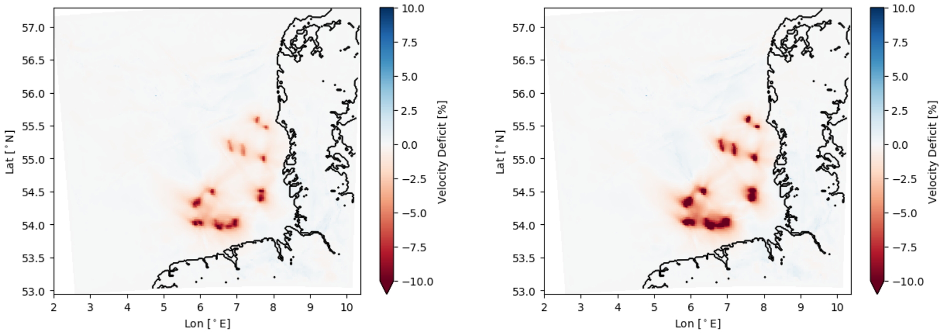

(E) EWP - March (F) Fitch - March

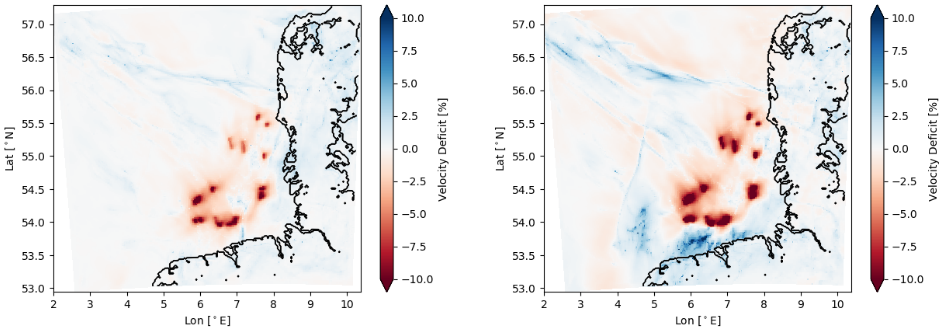

(G) EWP - April (H) Fitch - April

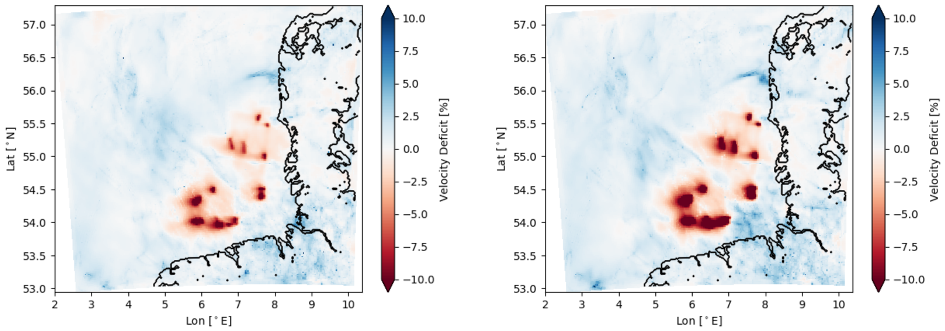

(I) EWP - May

(J) Fitch - May

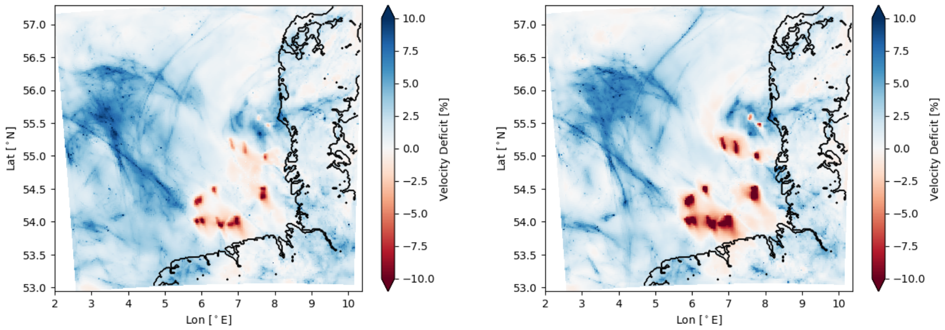

(K) EWP - June

(L) Fitch - June

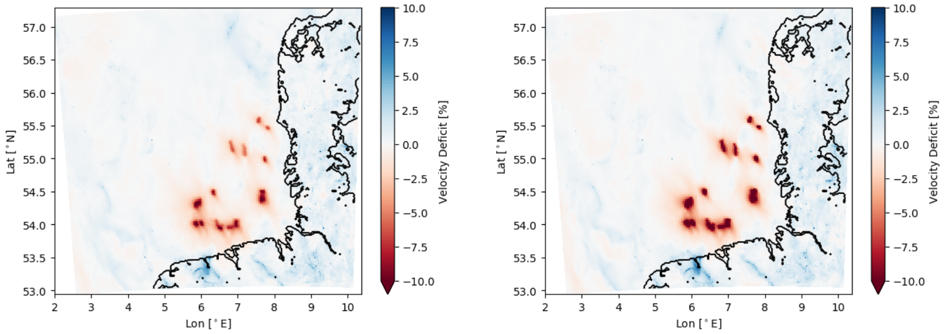

(M) EWP - July

(N) Fitch - July

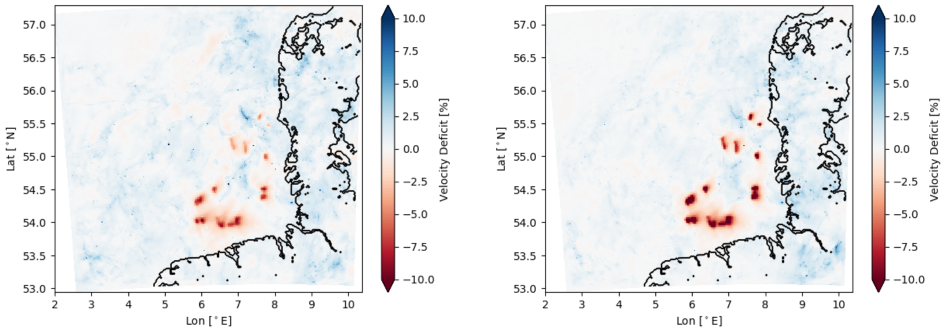

(O) EWP - August

(P) Fitch - August

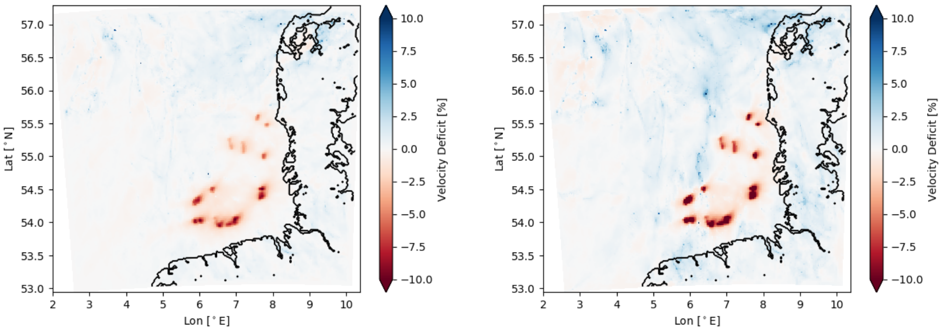

(Q) EWP - September (R) Fitch - September

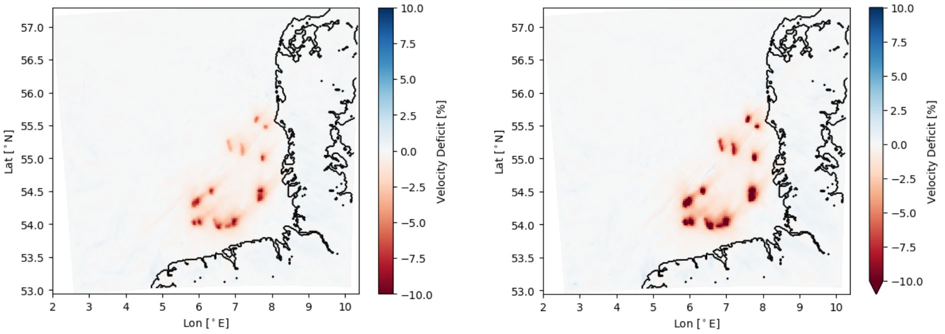

(S) EWP - October (T) Fitch - October

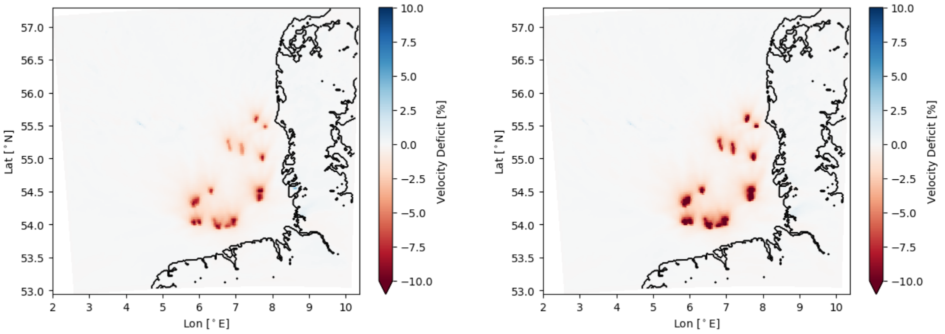

(U) EWP - November (V) Fitch - November

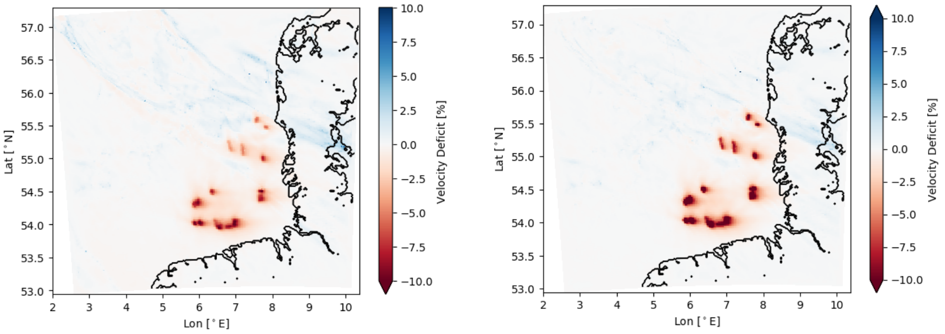

(W) EWP - December (X) Fitch - December

FIGURE 11.3: Monthy mean velocity deficit for EWP and Fitch schemes

The previous plots in this chapter of mean velocity profile and mean velocity deficit profile showed clear reduction in wind speed in and around the wind farms, but wind farm wakes have not yet been observed behind the wind farms. To investigate the results further for such evidence, the velocity deficit is depicted once again. In Figure 11.4, the monthly mean wind speed for each bin of wind direction is reported, for the month of May. May was selected as the first test case as the previous plots indicated high velocity deficits for this month. The domain has been cropped to approximately 2% of its original area in order to more closely inspect the wakes at SandBank and DanTysk, and to attempt to crop out the neighbouring wind farms, without cutting out too much of the downstream wake. The reader can see that there are five wind farms contained in this domain, with the two most western wind farms (centrally located in the domain) being SandBank and DanTysk. Immediately, it is clear that there is a significant degree of interation between all of the wind farms in this sub-domain. For prevailing winds from 120^o to 240^o, the wakes from either Global Tech I, BARD Offshore I or Veja Mate persist to the edge of SandBank and DanTysk. This is a distance of 70-100 km. Through this presentation, it is clear that it is not possible to isloate the characteristics of a single wind farm wake.

This presentation of data can be compared with the SCADA data analysis which was presented in Chapter 9. Figure 11.4 depicts only the month of May using the Fitch scheme. From the long term climatological study at FINO3, it is known that March, April and May are typically the most atmospherically stable months of the year. With evidence of high velocity deficits and stable conditions approximately 50% of the month, the conditions are favorable for persistent wind farm wakes in this month. Subfigure (C) depicts the bin of wind speeds between 60^o and 90^o. In the SCADA analysis, the turbine-wise measured wind speed and turbine capacities suggested that the wake from DanTysk was shadowing the south end of SandBank. The simulation results for the month of May support this conclusion. The wake region between the two wind farms is shaded and the southern end of SandBank can be seen in a darker shade than the north end of the wind farm.

The reader may recall interesting results from SCADA analysis for the wind speed bin from 240^o to 270^o. The SCADA data showed the wind speeds at DanTysk to be approximately 1 to 1.5 ms^{-1} higher than at SandBank, despite SandBank's unwaked position relative to DanTysk. The results presented for the month of May do not support the SCADA results. The measurements showed above average capacity factors at both wind farms and wind speeds between 9 and 10 ms^{-1}. The simulation results for May show faint wakes, which is not indicative of favorable power extraction. This is supported by the frequency of occurrence of this wind speed bin throughout the year (see Table 11.2).

TABLE 11.2: Distribution of frequency of occurrence of wind speed bin 9 on a monthly basis, reported in percentage occurrence

Jan.	Feb.	Mar.	April	May	June	July	Aug.	Sept.	Oct.	Nov.	Dec.
21.7	9.4	4.1	17.7	2.8	9.1	7.9	24.9	31.8	12.7	3.9	17.9

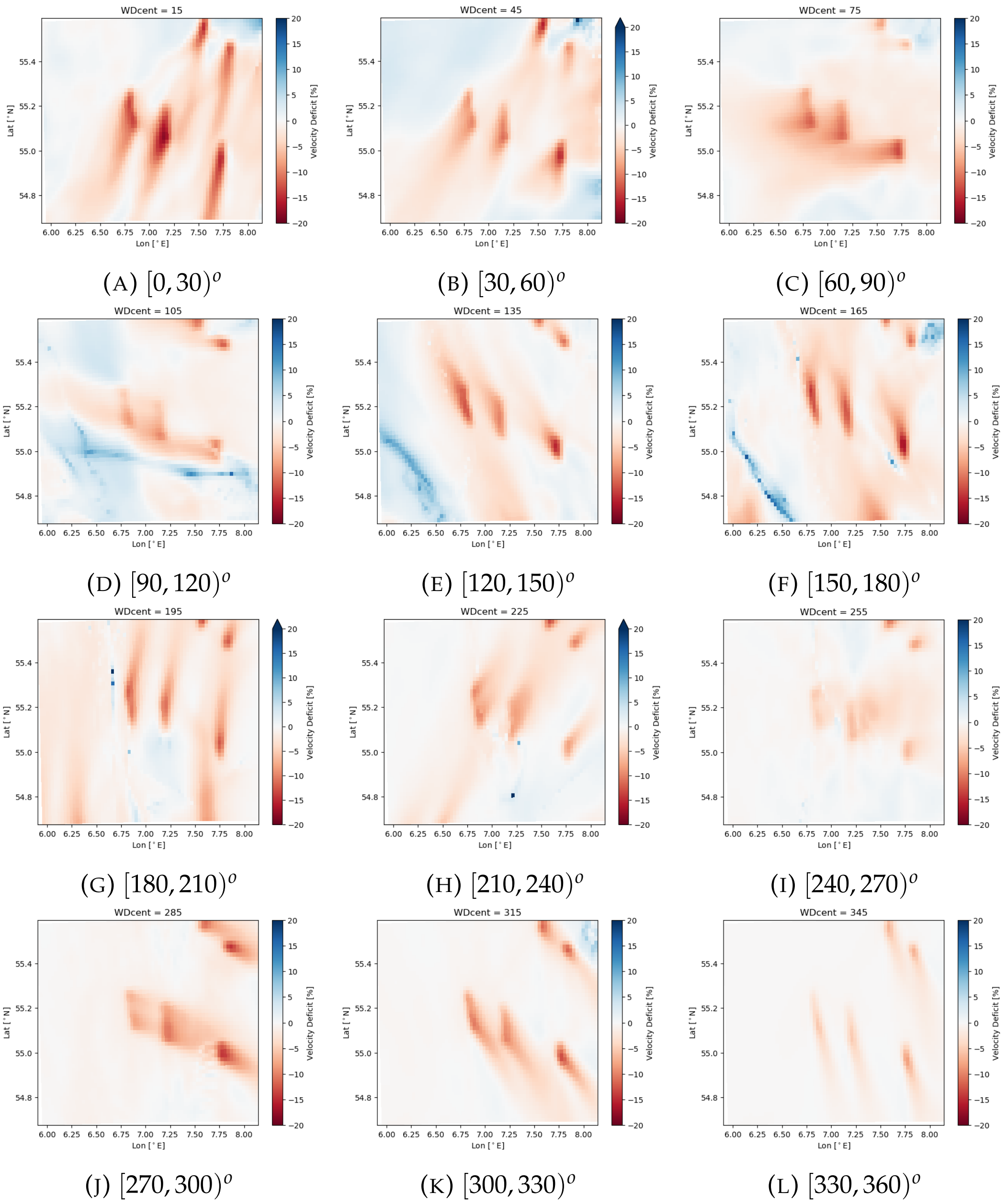

(A) $[0,30)^o$ (B) $[30,60)^o$ (C) $[60,90)^o$

(D) $[90,120)^o$ (E) $[120,150)^o$ (F) $[150,180)^o$

(G) $[180,210)^o$ (H) $[210,240)^o$ (I) $[240,270)^o$

(J) $[270,300)^o$ (K) $[300,330)^o$ (L) $[330,360)^o$

FIGURE 11.4: Month mean wind speed deficit at representative hub height for the month of May using the Fitch scheme based on prevailing wind direction

It is not possible to show all of the monthly mean velocity deficit plots binned by wind direction in this report, however the entire year of plots have been analyzed by the author. The wind speed deficit tends to be greatest when the prevailing wind direction is along the long axis of the wind farms. Southerly winds often results in SandBank or DanTysk being shadowed by the wind farms to the south. Northerly winds (particularly bin 1) produce long wakes at Horns Rev which extend to the region of SandBank and DanTysk. Figure 11.5 shows the same wind speed bin, $[270,300)^o$, for every month of the year. The analysis earlier in this chapter indicated that March, April and May exhibit low mean wind speeds and strong wakes. In terms of frequency of occurrence of thie wind direction bin, it most often occurs from June through the winter and in January. Occurrences in April, May and June each account for approximately 5% of occurrences.

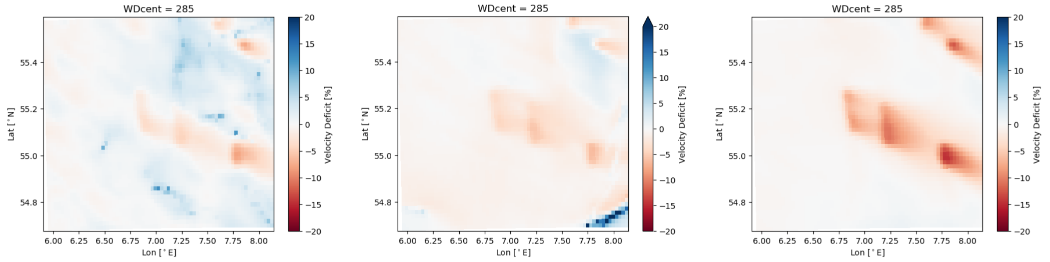

(A) January (B) February (C) March

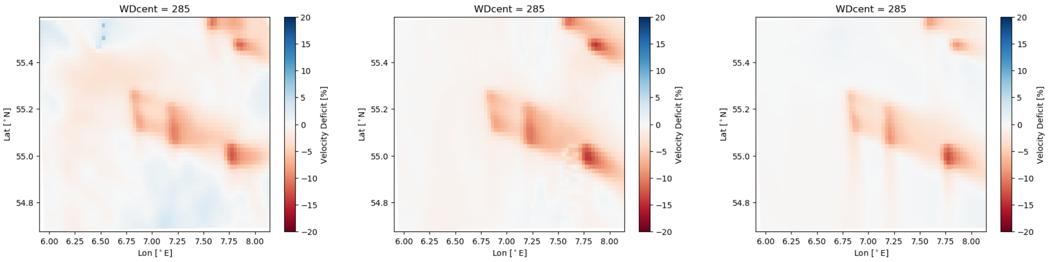

(D) April (E) May (F) June

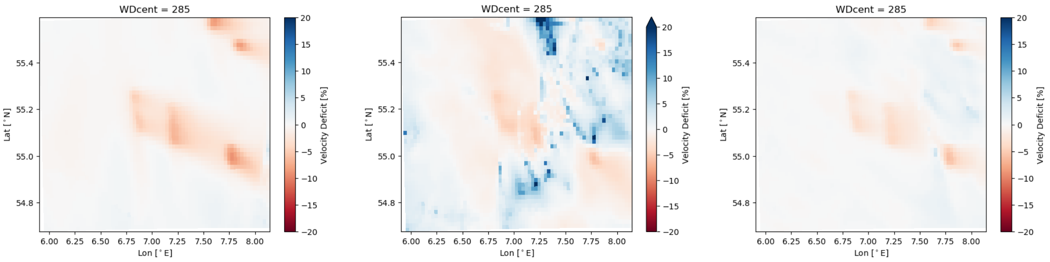

(G) July (H) August (I) September

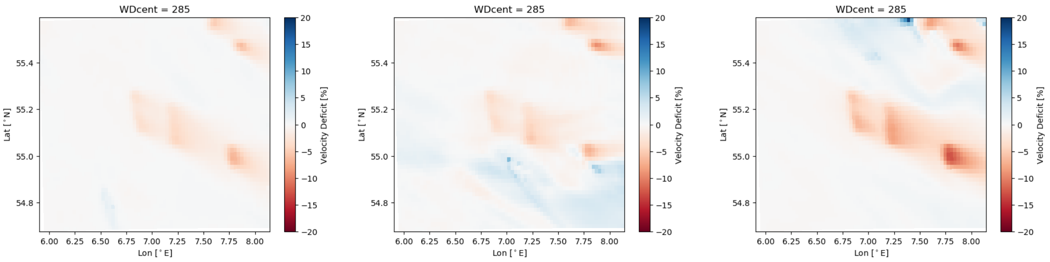

(J) October (K) November (L) December

FIGURE 11.5: Month mean wind speed deficit at representative hub height for all months in wind direction bin 10, $[270, 300)^o$, using the EWP scheme based on prevailing wind direction

Studying velocity deficit fields for independent wind directions sectors has been very effective in this author's study of wind farm wakes. It preserves the directional dependence of the wakes, and does not blur the wakes in the way that a long-term temporal average does. Particularly when armed with statistics of the frequency of occurrence of parameters such as wind direction, wind speed and stability condition, the results provide a great understanding of the behaviour of the wind. This analysis has also revealed that it is not possible to isolate one wind farm wake in a region so densely packed with wind farms as the current study. Therefore it is impossible to quantify characteristics such as wake length or width. Instead, the author has attempted to quantify the entire area of the 60 km × 60 km sub-domain (the same sub-domain which was studied in Figures 11.4 and 11.5). The velocity deficit has been discretized into bins of 1% between ±100%. Each grid cell in the domain adds a tally to the appropriate velocity deficit bin, and that tally is equal to the grid cell area (4 km^2). This tally is executed for a particular month and a particluar bin of wind direction. The result is then divided by the total time, to give a representative snapshot in time of the penetration of wakes in the domain. This analysis is essentially a histogram, shown in Figure 11.6. This analysis considers five model levels, z = [29,55,89,120,150] m. Both EWP and Fitch schemes are represented on the same figure. Depicted in Figure 11.6 are all wind direction bins for December 2018. The vertical axis is a log scale. The reader is reminded that affected areas less than 4 km^2 are less than one grid cell, therefore are so infrequent in the simulations as to not make up one grid cell over a one month period. These data can practically be ignored. For all wind direction bins, a sharp peak exists at 0% velocity deficit. This is expected, as a large portion of the domain is unaffected by the wind farm wakes. Bins 1,2,3,6,7,11 and 12 exhibit a vertical line at or near 0% velocity deficit. This indicates that there are consistently no positive velocity deficits in the sub-domain. The other bins drop quickly back to zero, but it is clear that some positive velocity deficits cropped up in these simulations, whether they may be real phenomena or artifacts of the simulation method.

In the region of negative velocity deficits, the Fitch curves typically lie above the EWP curves. This is indicative of a larger area affected by wind farm wakes. These curves also cross the 4 km^2 line at greater magnitudes of velocity deficit. The 5 heights considered agree well over height (all heights follow the same trend). In the Fitch scheme, when one curve lies above the others, it is the curve at hub height (green curve). The next two are the next levels above, and below hub height. This agrees with the results of P. Volker that the velocity deficit profile in the Fitch scheme reaches a maximum just above hub height [19].

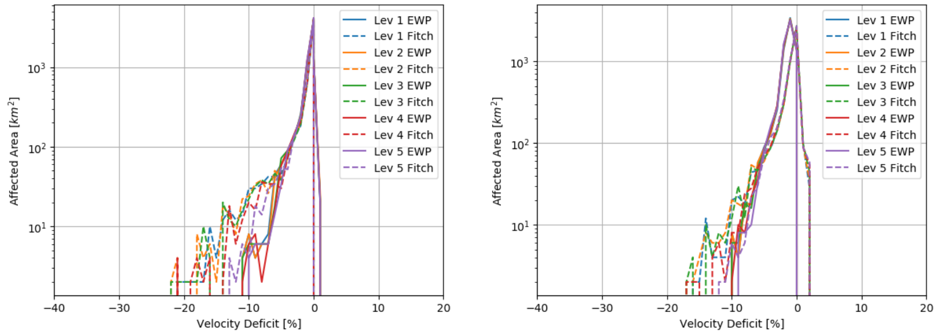

(A) $[0, 30)^o$ (B) $[30, 60)^o$

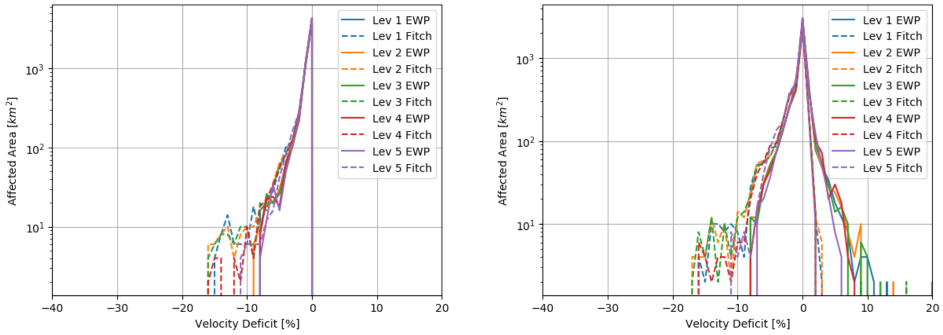

(C) $[60, 90)^o$ (D) $[90, 120)^o$

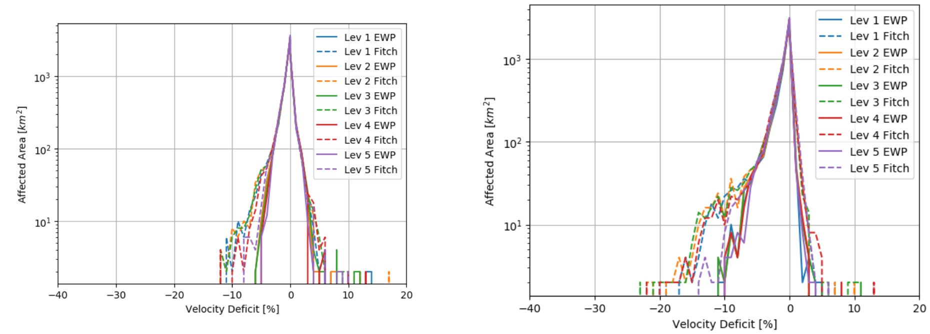

caption$[120, 150)^o$ (E) $[150, 180)^o$

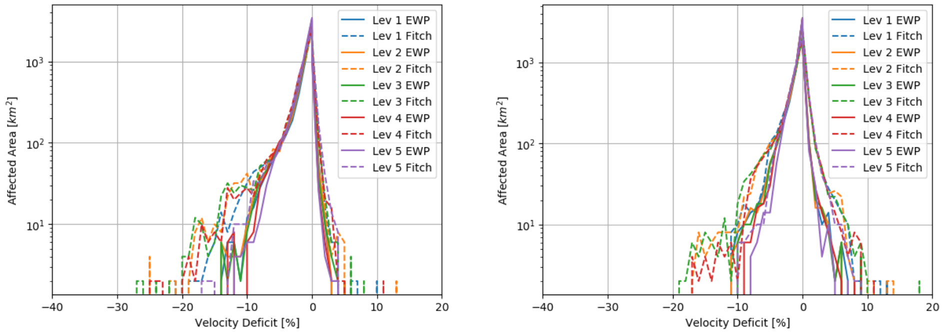

(F) $[180, 210)^o$ (G) $[210, 240)^o$

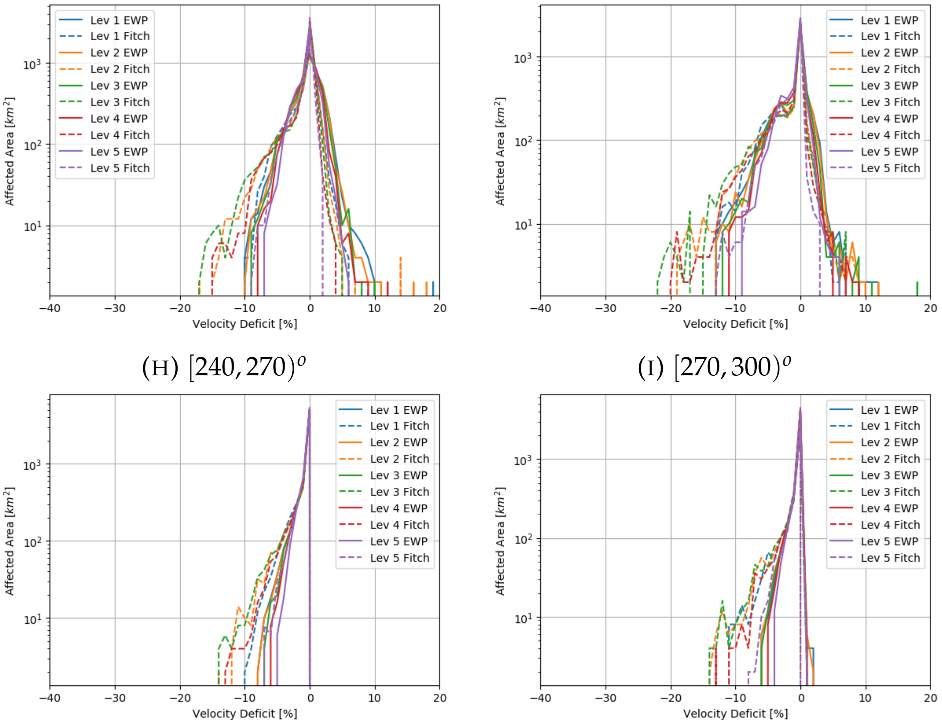

(H) $[240, 270)^o$ (I) $[270, 300)^o$

(J) $[300, 330)^o$ (K) $[330, 360)^o$

FIGURE 11.6: Velocity deficit area histogram for December, filtered by wind direction, including both WFP and 5 model heights

Chapter 12

Conclusion

The goal of this study was to characterize offshore wind farm wakes in terms of meteorological parameters by conducting long-term modelling. The region of study was chosen due to the likely occurrence of wind farm shadow effects and the availability of wind farm power performance data available for study and model validation.

The analysis consisted of a quantitative analysis of numerous sources of climatological data to characterize the surrounding climatology. This climatology was then studied in the context of long term data to find that the chosen year of study is quite representative of the long term climate. Determined quantities were wind speed distribution, wind speed direction distribution, turbulence intensity and atmospheric stability. The general trend observed in the stability data in this region was the tendancy for stable conditions to persist in the summer and more unstable conditions to be present in the winter. One challenge when working with insitu data is the reality of working with measurements. Sometimes the data recovery is poor, or the placement of the measurement device is not ideal. Fortunately this study benefitted from many available sources of data to compensate for poor availability or uncertainties in the cause of certain trends in the data.

Next, long term simulations were conducted by executing simulations in WRF. Two wind farm parameterization schemes can be used to model wind farms in WRF, however there is no consensus in the industry on which one performs better than the other. For this reason, an aim of this project was to use the two parameterization schemes and compare their relative performance. Metrics of performance were considered to be power bias relative to SCADA data and the ability of WRF to replicate the measured climatology in the region. In the WRF validation phase of this project, the Fitch and EWP schemes were directly compared with the SCADA measurements from each wind farm. The EWP scheme consistently under-reported wind speed and mean power, while the Fitch scheme consistently over-reported these same quantities. In this analysis, care was taken to "turn off" turbines in the WRF results which were not operating in the SCADA data. This changed the results relating to the performance of the WFP schemes and would be a recommended practice for similar analyses in the future . The final piece of the validation analysis was to test a finding seen by Lee and Lundquist in their WRF-Fitch validation using 4-days of measured data [18]. The authors of that study observed a trend in their power and wind speed biases such that as one approached 0, so to did the other. This is an example of the power of a large dataset such as the one used in this thesis. The author observed the same trend, but with many more outliers. Two important conclusions are drawn from this particular exercise - the errors in this correlation could likely be minimized with more advanced treatment of the measurement and simulation data, and improvements in WRFs ability to model the background flow might consequently reduce the errors seen in power predictions.

The WRF data was expressly analysed to investigate the dependence of wind farm wakes on climatological variables. The paired analysis of SCADA data, offering turbine-level resolution of data, to the larger scale data available in the WRF simulations permitted lots of exploration into the cause of various curious behaviour seen in the results. Firstly, the author hypothesized that DanTysk would suffer a greater influence from SandBank than vice versa. However the results show that the opposite is true. The strongest wakes were observed in the summer months, which coincides with the most frequent stable atmospheric conditions. Looking into both SCADA data and velocity deficit profiles in the wind speed bin from [240,270)^o, lower wind speeds are seen at SandBank as compared to DanTysk. Meanwhile both wind farms perform with above average capacity factory. This disproves the author's original hypothesis. An important opservation from analysing the North Sea region is that the wind farm wakes from many wind farms are interacting with one another. This makes the isolation of a single wake very challenging. It also reqires a researcher to be aware that there can be a myriad of reasons for the flow patterns they observe. Finally, an important learning from this analysis is that wind farm wakes are dependent on wind direction. This is also true of the analysis of wakes. As a results, it can be cumbersome to present statistics, determine wake length or visalize the data.

This study has contributed to the body of research on wind farm wakes by conducting a year-long simulation of wind farm wakes in the North Sea. The survey of literature indicates that few such studies have been condcted for long time periods. It can be challenging to make decisive conclsions from a short dataset, however long term studies such as this master thesis can help to validate shorter studies.

12.1 Recommendations and Future Work

This project has provided evidence to support the dependence of wind farm wakes on atmospheric stability and wind direction. There are however many parameters at play in the atmosphere and it was seen in the present study that the interdependence of numerous variables dictate the wake behaviour. The uncertainty associated with the background flow was a complicating factor in the present analysis. It is unreasonable to expect that subtracting instantaneous data points will produce a zero velocity deficit plane, however an improved method to filter out these fluctuations can lead to much clearer analyses of the wake behaviour. At present, these positive fluctuations can be ignored, however it is uncertain to what extent they also impact the wake behaviour.

The present work be improved by validating the background flow modelling. As discussed early in this report, researchers are beginning to report that the error associated with the modelling of the background flow has been greater than the errors associated with a wind farm parameterization. WFP studies often report a discrepancy in wind speed compared to a known quantity however this might be wrong to attribute the entire error to the WFP. Validation studies of the background flow model could improve confidence in the model.

As mentioned above, there are many factors at play in the atmosphere surrounding a wind farm. When attempting to understand wind farm wakes, it helps to understand the behaviour of each piece of the puzzle on its own. In the present study for example, WRF simulations could be conducted to gain a better understanding of the internal wind farm wake. This reasoning could also be applied to a study of wind farm wakes in the North Sea. In this study, a lot of interaction between wind farm wakes was observed and it could lead to a very interesting analysis if the entire North Sea were studied.

Finally, Lundquist et al. [6] recently conducted a study which presented an analysis of the fiscal implications of wind farm wakes on power production revenues, bygone carbon credits and sunk costs to purchasing fossil fuels. This is one such practical example of quantifying the path and shape of wakes.

Appendix A

SCADA Analysis

A.1 Annual Mean Capacity Factor

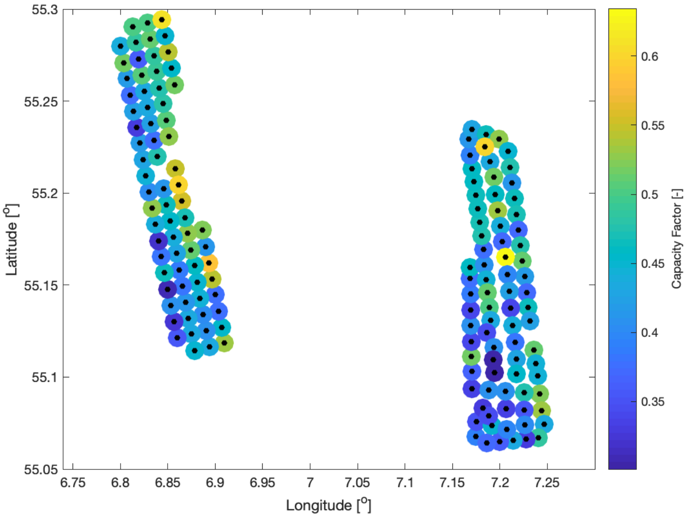

FIGURE A.1: Annual mean Capacity Factor for WD bin [0,30)]

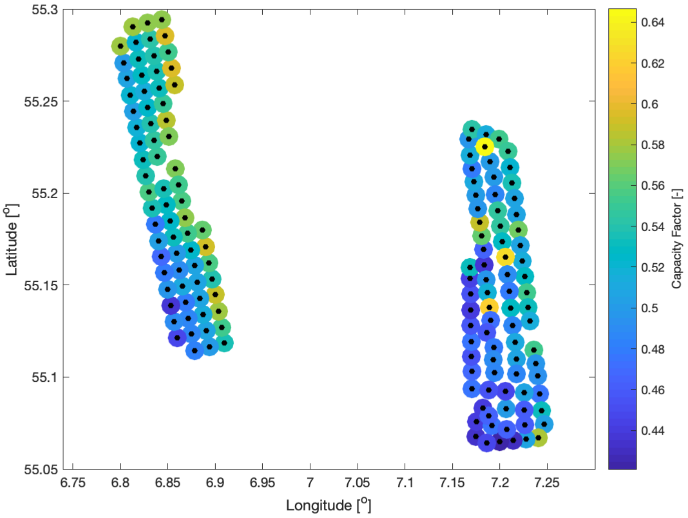

FIGURE A.2: Annual mean Capacity Factor for WD bin [30,60)]

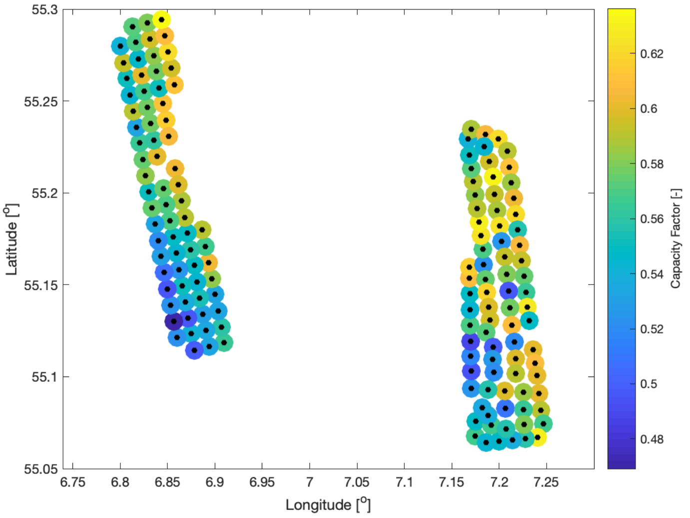

FIGURE A.3: Annual mean Capacity Factor for WD bin [60,90)]

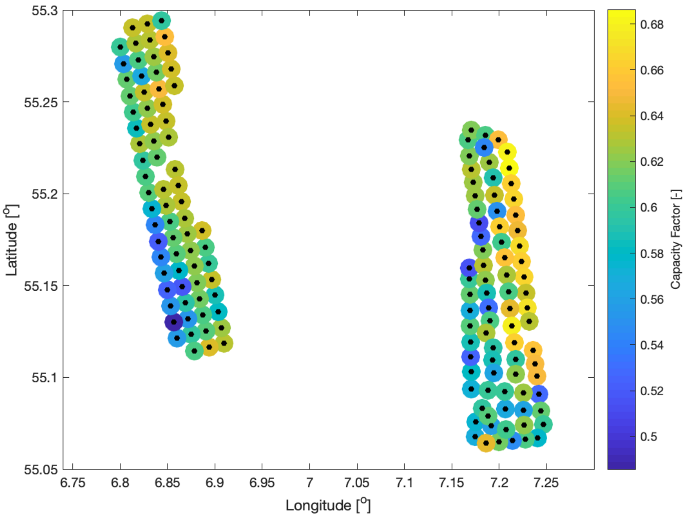

FIGURE A.4: Annual mean Capacity Factor for WD bin [90,120)]

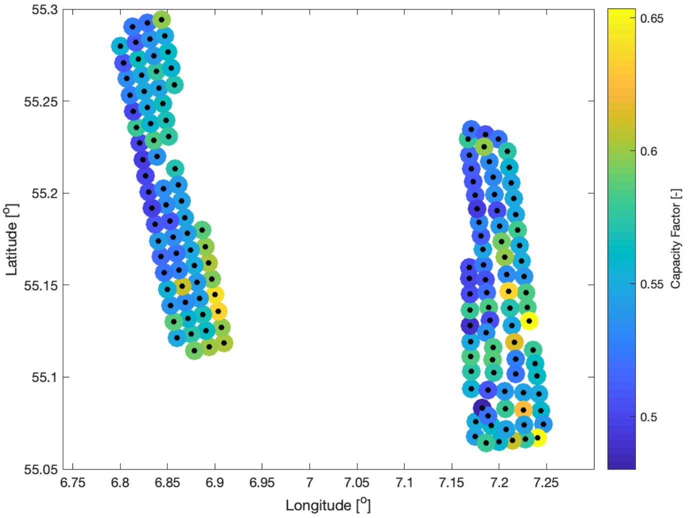

FIGURE A.5: Annual mean Capacity Factor for WD bin [120,150)]

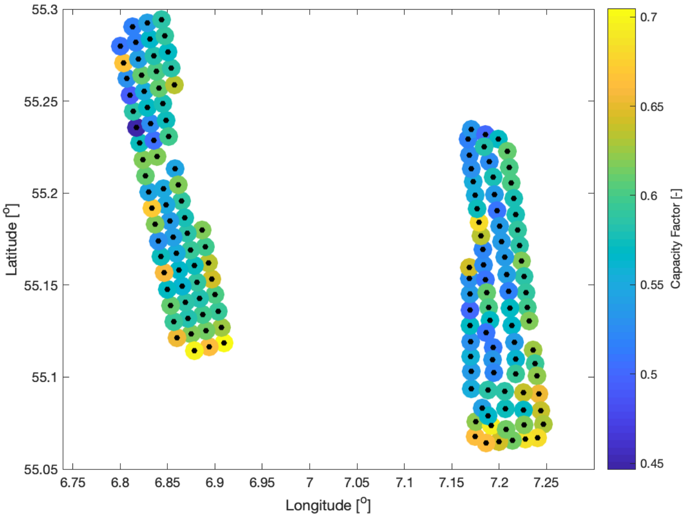

FIGURE A.6: Annual mean Capacity Factor for WD bin [150,180)]

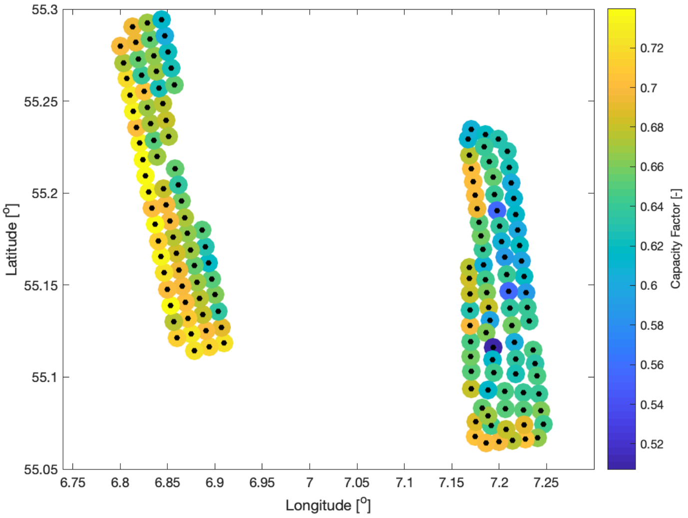

FIGURE A.7: Annual mean Capacity Factor for WD bin [180,210)]

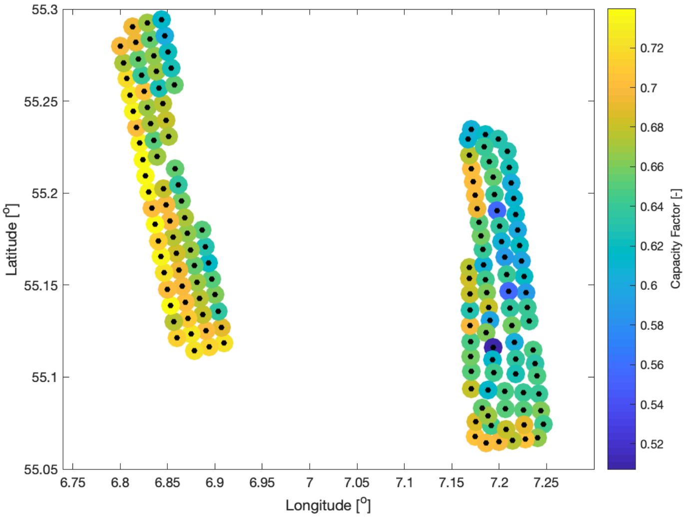

FIGURE A.8: Annual mean Capacity Factor for WD bin [180,210)]

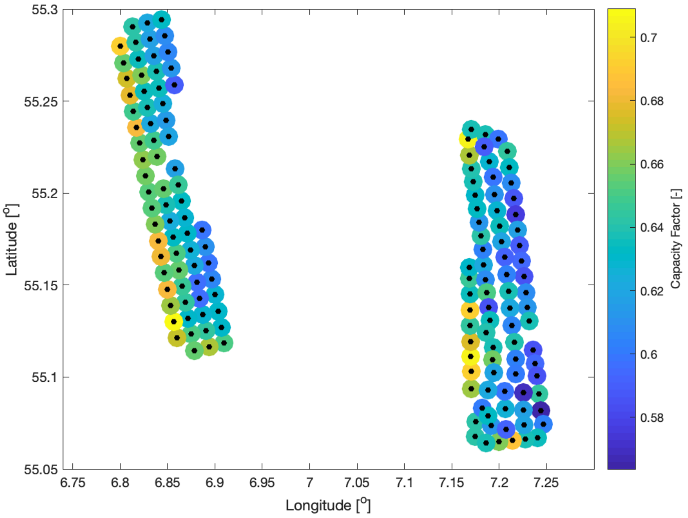

FIGURE A.9: Annual mean Capacity Factor for WD bin [210,240)]

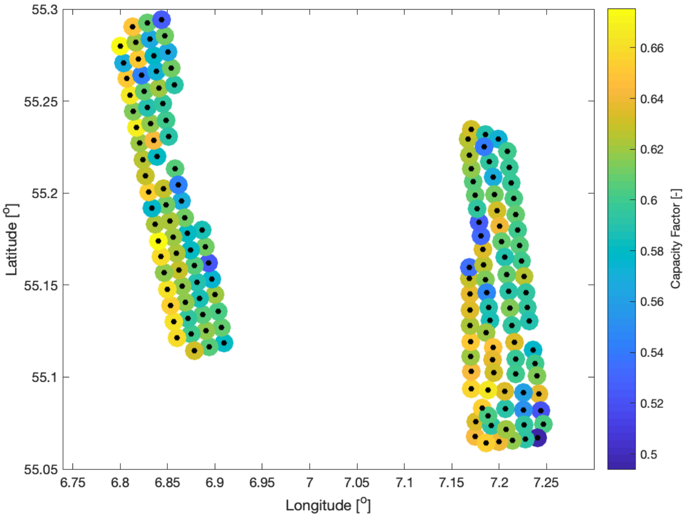

FIGURE A.10: Annual mean Capacity Factor for WD bin [240,270)]

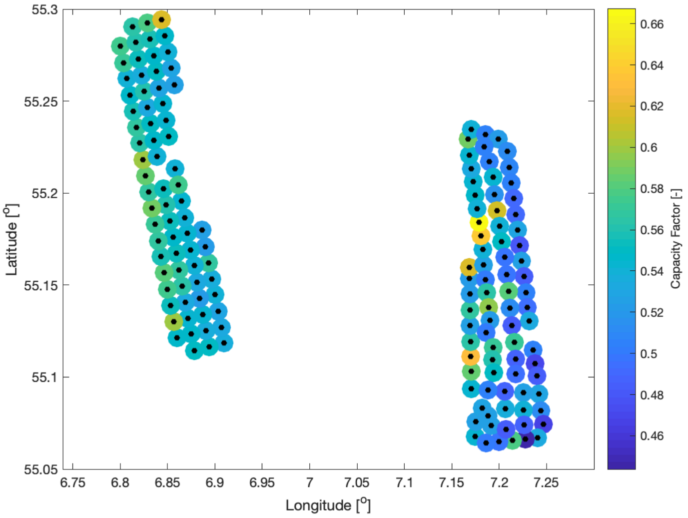

FIGURE A.11: Annual mean Capacity Factor for WD bin [270,300)]

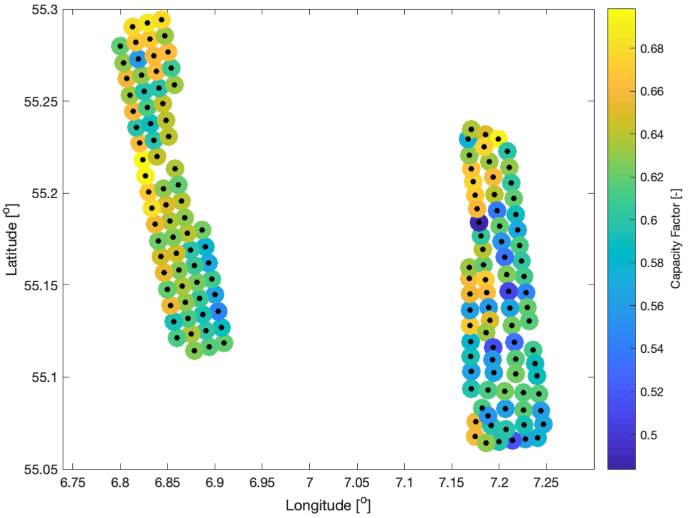

FIGURE A.12: Annual mean Capacity Factor for WD bin [300,330)]

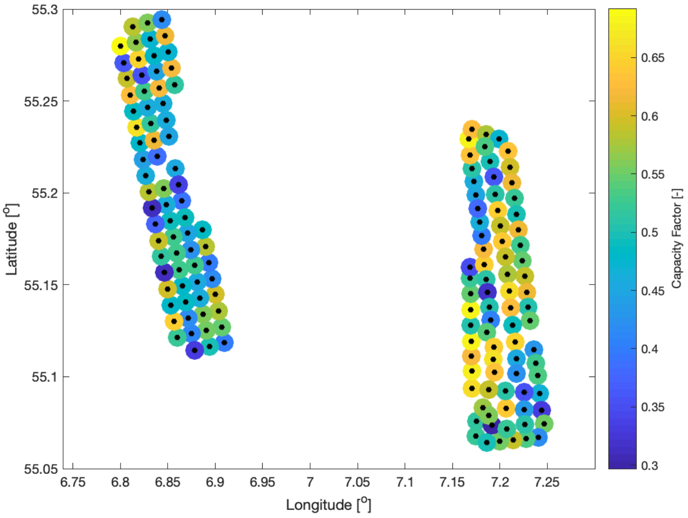

FIGURE A.13: Annual mean Capacity Factor for WD bin [330,390)]

A.2 Annual Mean Wind Speed

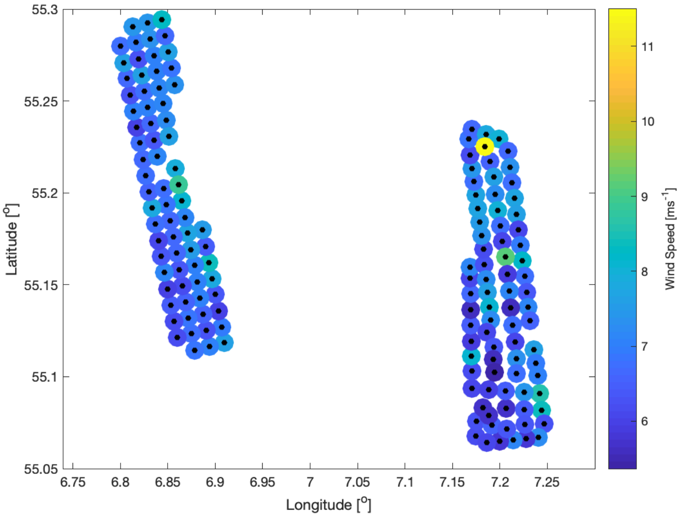

FIGURE A.14: Annual mean wind speed for WD bin [0,30)]

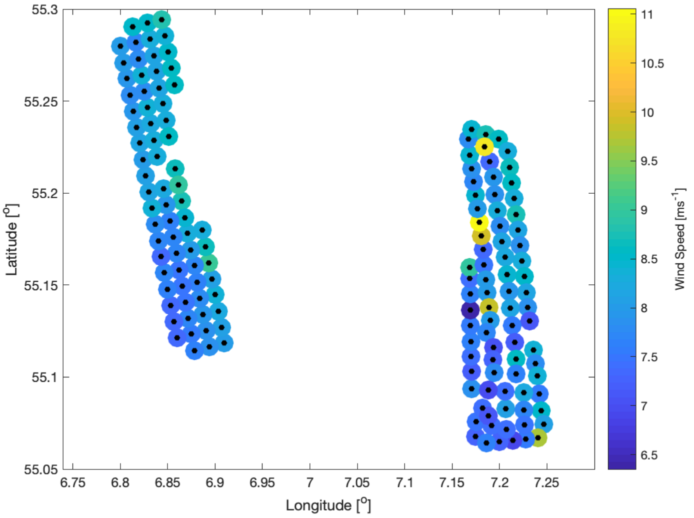

FIGURE A.15: Annual mean wind speed for WD bin [30,60)]

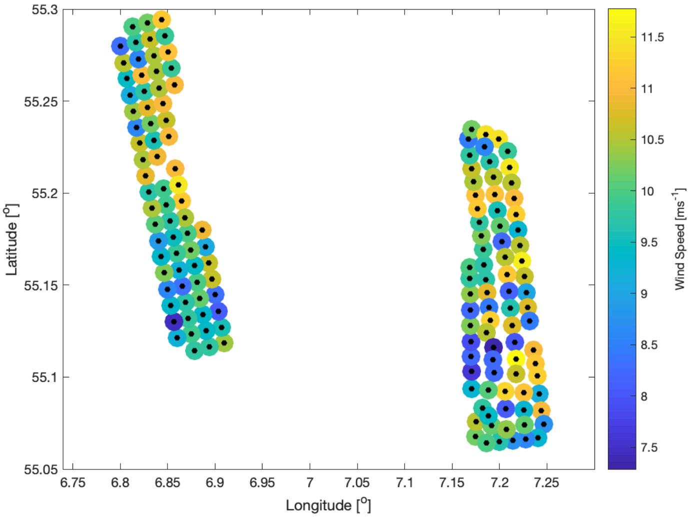

FIGURE A.16: Annual mean wind speed for WD bin [60,90)]

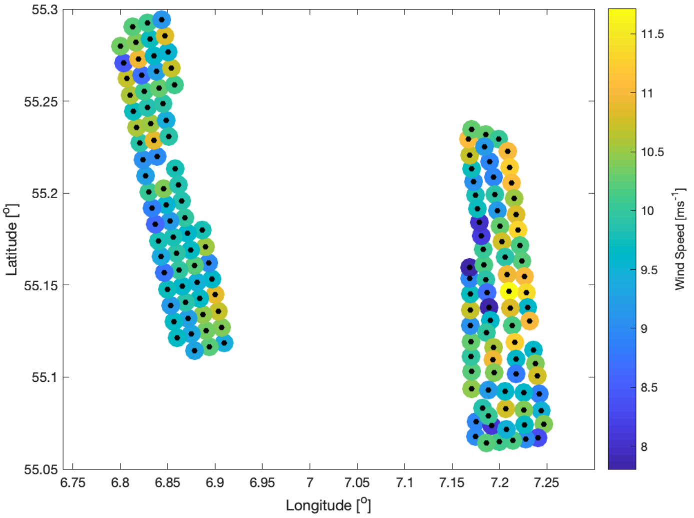

FIGURE A.17: Annual mean wind speed for WD bin [90,120)]

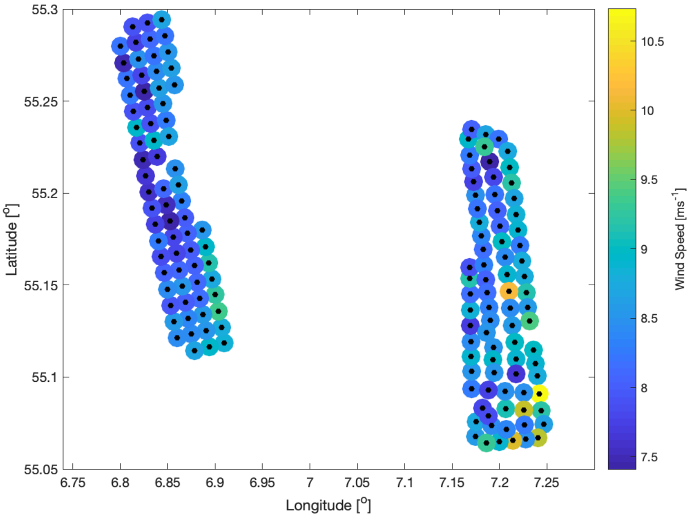

FIGURE A.18: Annual mean wind speed for WD bin [120,150)]

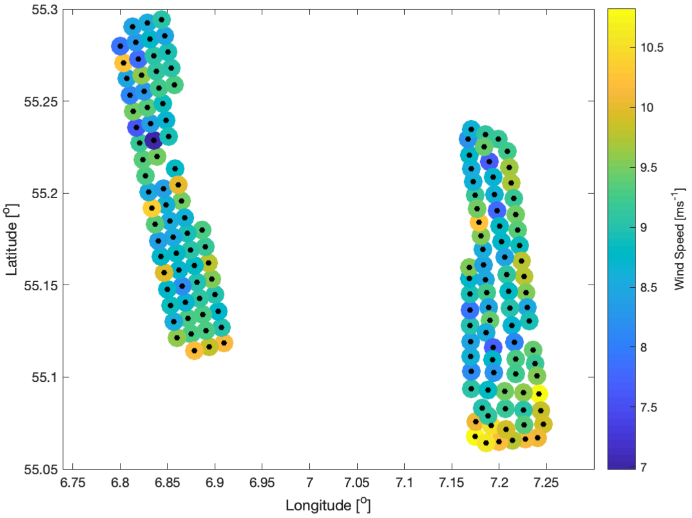

FIGURE A.19: Annual mean wind speed for WD bin [150,180)]

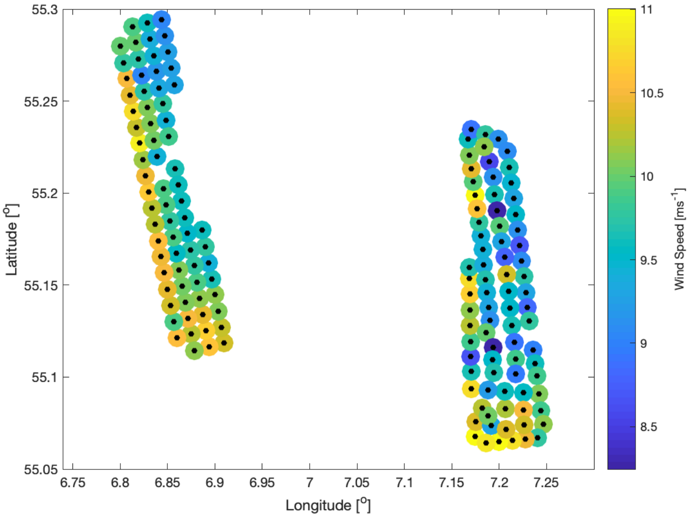

FIGURE A.20: Annual mean wind speed for WD bin [180,210)]

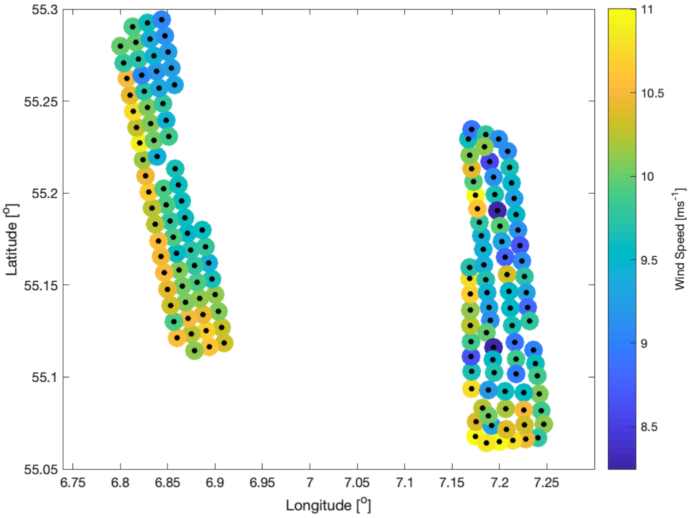

FIGURE A.21: Annual mean wind speed for WD bin [180,210)]

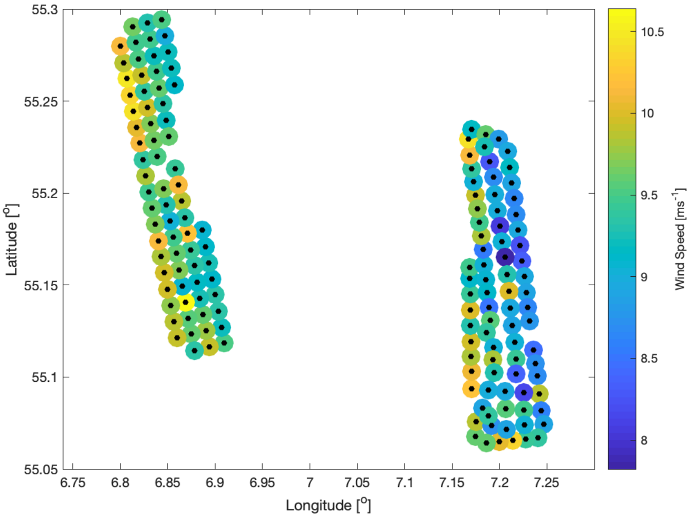

FIGURE A.22: Annual mean wind speed for WD bin [210,240)]

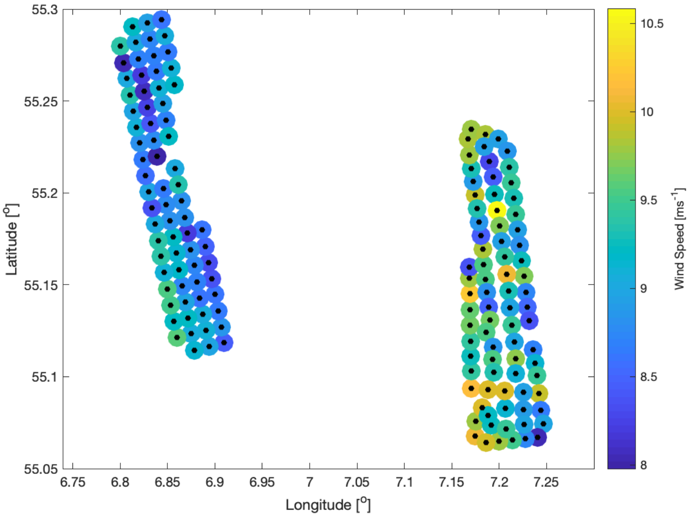

FIGURE A.23: Annual mean wind speed for WD bin [240,270)]

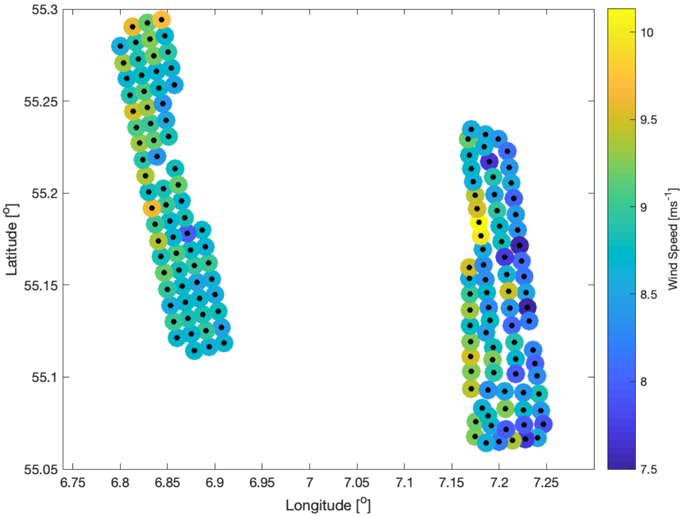

FIGURE A.24: Annual mean wind speed for WD bin [270,300)]

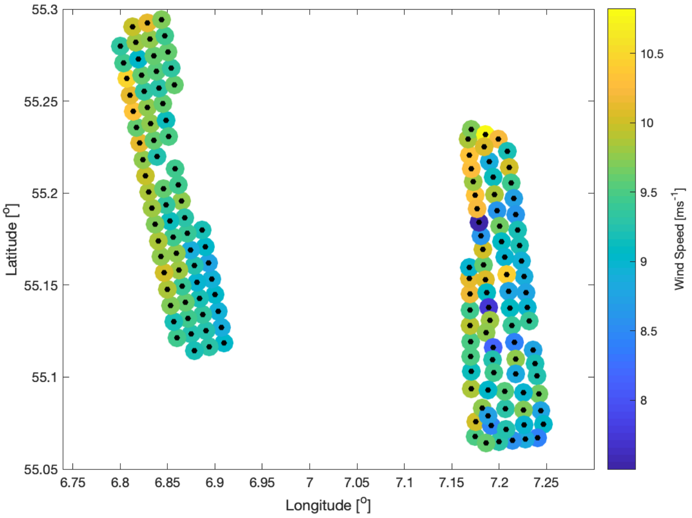

FIGURE A.25: Annual mean wind speed for WD bin [300,330)]

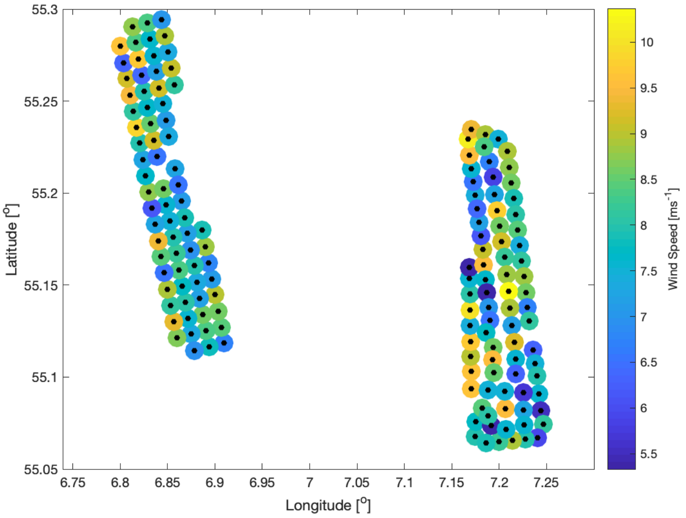

FIGURE A.26: Annual mean wind speed for WD bin [330,360)]

Bibliography

[1] I., V. Masson-Delmotte, P Zhai, H.-O. Pörtner, D. Roberts, J Skea, P R. Shukla, A Pirani, W Moufouma-Okia, C Péan, R Pidcock, S Connors, R. Matthews, Y Chen, X Zhou, M I. Gomis, E Lonnoy, T Maycock, M Tignor, and T Waterfield, *Global warming of* $1.5^{o}C$*. An IPCC Special Report on the impacts of global warming of* $1.5^{o}C$ *above pre-industrial levels and related global greenhouse gas emission pathways, in the context of strengthening the global response to the threat of climate change, sustainable development, and efforts to eradicate poverty*. Dec. 2018.

[2] *Climate change*. [Online]. Available: https://windeurope.org/policy/topics/climate-change/ (visited on 07/22/2019).

[3] *Offshore wind in Europe – key trends and statistics 2018*, Feb. 2019. [Online]. Available: https://windeurope.org/about-wind/statistics/offshore/european-offshore-wind-industry-key-trends-statistics-2018/ (visited on 07/22/2019).

[4] *Wind energy in Europe in 2018*, Feb. 2019. [Online]. Available: https://windeurope.org/about-wind/statistics/european/wind-energy-in-europe-in-2018/ (visited on 07/22/2019).

[5] C. B. Hasager, P Vincent, R Husson, A Mouche, M Badger, A Peña, P Volker, J Badger, A Di Bella, A Palomares, E Cantero, and P. M. F. Correia, “Comparing satellite SAR and wind farm wake models”, en, *Journal of Physics: Conference Series*, vol. 625, p. 012 035, Jun. 2015, ISSN: 1742-6588, 1742-6596. DOI: 10.1088/1742-6596/625/1/012035. [Online]. Available: http://stacks.iop.org/1742-6596/625/i=1/a=012035?key=crossref.9a9e2b0d83dcc13ca5b93302fd20b22b (visited on 11/01/2018).

[6] J. K. Lundquist, K. K. DuVivier, D. Kaffine, and J. M. Tomaszewski, “Costs and consequences of wind turbine wake effects arising from uncoordinated wind energy development”, en, *Nature Energy*, vol. 4, no. 1, pp. 26–34, Jan. 2019, ISSN: 2058-7546. DOI: 10.1038/s41560-018-0281-2. [Online]. Available: http://www.nature.com/articles/s41560-018-0281-2 (visited on 07/22/2019).

[7] X. G. Larsén, P. Volker, P. E. Sørensen, J. Nissen, J. Du, G. Giebel, S. Ott, C. B. Hasager, P. Maule, A. N. Hahmann, T. T. Ahsbahs, and J. Badger, “Large scale offshore wake impact on the danish power system”, eng, 2018.

[8] *Global Statistics 2018 (preliminary)*, en. [Online]. Available: https://public.tableau.com/views/Template_wwea/Dashboard1?:embed=y&:showVizHome=no&:host_url=https%3A%2F%2Fpublic.tableau.com%2F&:embed_code_version=3&:tabs=no&:toolbar=yes&:animate_transition=yes&:display_static_image=no&:display_spinner=no&:display_overlay=yes&:display_count=yes&publish=yes&:loadOrderID=0 (visited on 07/22/2019).

[9] *Global Offshore Renewable Map - 4c Offshore*. [Online]. Available: https://www.4coffshore.com/offshorewind/ (visited on 04/16/2019).

[10] N. Moskalenko, K. Rudion, and A. Orths, “Study of wake effects for offshore wind farm planning”, en, p. 7,

[11] N. O Jensen, *A NOTE ON WIND GENERATOR INTERACTION*. en. ROSKILDE: RISOE NAT. LAB. NOV, 1983, OCLC: 1075460569, ISBN: 978-87-550-0971-4.

[12] M. L. Aitken, R. M. Banta, Y. L. Pichugina, and J. K. Lundquist, "Quantifying Wind Turbine Wake Characteristics from Scanning Remote Sensor Data", en, *Journal of Atmospheric and Oceanic Technology*, vol. 31, no. 4, pp. 765–787, Apr. 2014, ISSN: 0739-0572, 1520-0426. DOI: `10.1175/JTECH-D-13-00104.1`. [Online]. Available: `http://journals.ametsoc.org/doi/abs/10.1175/JTECH-D-13-00104.1` (visited on 04/07/2019).

[13] M. B. Christiansen and C. B. Hasager, "Using airborne and satellite SAR for wake mapping offshore", en, *Wind Energy*, vol. 9, no. 5, pp. 437–455, Sep. 2006, ISSN: 1095-4244, 1099-1824. DOI: `10.1002/we.196`. [Online]. Available: `http://doi.wiley.com/10.1002/we.196` (visited on 08/14/2019).

[14] C. Hasager, P. Vincent, J. Badger, M. Badger, A. Di Bella, A. Peña, R. Husson, and P. Volker, "Using Satellite SAR to Characterize the Wind Flow around Offshore Wind Farms", en, *Energies*, vol. 8, no. 6, pp. 5413–5439, Jun. 2015, ISSN: 1996-1073. DOI: `10.3390/en8065413`. [Online]. Available: `http://www.mdpi.com/1996-1073/8/6/5413` (visited on 11/01/2018).

[15] M. B. Christiansen and C. B. Hasager, "Wake effects of large offshore wind farms identified from satellite SAR", en, *Remote Sensing of Environment*, vol. 98, no. 2-3, pp. 251–268, Oct. 2005, ISSN: 00344257. DOI: `10.1016/j.rse.2005.07.009`. [Online]. Available: `http://linkinghub.elsevier.com/retrieve/pii/S0034425705002476` (visited on 11/01/2018).

[16] A. Platis, S. K. Siedersleben, J. Bange, A. Lampert, K. Bärfuss, R. Hankers, B. Cañadillas, R. Foreman, J. Schulz-Stellenfleth, B. Djath, T. Neumann, and S. Emeis, "First in situ evidence of wakes in the far field behind offshore wind farms", en, *Scientific Reports*, vol. 8, no. 1, Dec. 2018, ISSN: 2045-2322. DOI: `10.1038/s41598-018-20389-y`. [Online]. Available: `http://www.nature.com/articles/s41598-018-20389-y` (visited on 11/01/2018).

[17] S. K. Siedersleben, A. Platis, J. K. Lundquist, A. Lampert, K. Barfuss, B. Cañadillas, B. Djath, J. Schulz-Stellenfleth, J. Bange, T. Neumann, and S. Emeis, "Evaluation of a Wind Farm Parametrization for Mesoscale Atmospheric Flow Models with Aircraft Measurements", en, *Meteorologische Zeitschrift*, vol. 27, no. 5, pp. 401–415, Dec. 2018, ISSN: 0941-2948. DOI: `10.1127/metz/2018/0900`. [Online]. Available: `http://www.schweizerbart.de/papers/metz/detail/27/89817/Evaluation_of_a_Wind_Farm_Parametrization_for_Meso?af=crossref` (visited on 04/15/2019).

[18] J. C. Y. Lee and J. K. Lundquist, "Evaluation of the wind farm parameterization in the Weather Research and Forecasting model (version 3.8.1) with meteorological and turbine power data", en, *Geoscientific Model Development*, vol. 10, no. 11, pp. 4229–4244, Nov. 2017, ISSN: 1991-9603. DOI: `10.5194/gmd-10-4229-2017`. [Online]. Available: `https://www.geosci-model-dev.net/10/4229/2017/` (visited on 06/02/2019).

[19] P. J. H. Volker, J. Badger, A. N. Hahmann, and S. Ott, "The Explicit Wake Parametrisation V1.0: A wind farm parametrisation in the mesoscale model WRF", en, *Geoscientific Model Development*, vol. 8, no. 11, pp. 3715–3731, Nov. 2015, ISSN: 1991-9603. DOI: `10.5194/gmd-8-3715-2015`. [Online]. Available: `https://www.geosci-model-dev.net/8/3715/2015/` (visited on 03/22/2019).

[20] S. C. Pryor, R. J. Barthelmie, and T. J. Shepherd, "The Influence of Real-World Wind Turbine Deployments on Local to Mesoscale Climate", en, *Journal of Geophysical Research: Atmospheres*, vol. 123, no. 11, pp. 5804–5826, Jun. 2018, ISSN: 2169897X. DOI: `10.1029/2017JD028114`. [Online]. Available: `http://doi.wiley.com/10.1029/2017JD028114` (visited on 08/14/2019).

[21] A. N. Kishore, "The Effect of Stability Conditions on Offshore Wind Farm Wakes – an Investigation through Mesoscale Modelling", English, Master's thesis, Technical University of Denmark, Lyngby, Denmark. (visited on 01/25/2019).

[22] A. N. Hahmann, C. L. Vincent, A. Pena, J. Lange, and C. B. Hasager, "Wind climate estimation using WRF model output: Method and model sensitivities over the sea: Offshore wind climate estimation using WRF output", en, *International Journal of Climatology*, vol. 35, no. 12, pp. 3422–3439, Oct. 2015, ISSN: 08998418. DOI: `10.1002/joc.4217`. [Online]. Available: `http://doi.wiley.com/10.1002/joc.4217` (visited on 03/22/2019).

[23] P. A. Jiménez, J. Navarro, A. M. Palomares, and J. Dudhia, "Mesoscale modeling of offshore wind turbine wakes at the wind farm resolving scale: A composite-based analysis with the Weather Research and Forecasting model over Horns Rev", en, *Wind Energy*, vol. 18, no. 3, pp. 559–566, Mar. 2015, ISSN: 1099-1824. DOI: `10.1002/we.1708`. [Online]. Available: `https://onlinelibrary-wiley-com.proxy.findit.dtu.dk/doi/abs/10.1002/we.1708` (visited on 03/22/2019).

[24] L. Vermeer, J. Sørensen, and A. Crespo, "Wind turbine wake aerodynamics", en, *Progress in Aerospace Sciences*, vol. 39, no. 6-7, pp. 467–510, Aug. 2003, ISSN: 03760421. DOI: `10.1016/S0376-0421(03)00078-2`. (visited on 04/09/2019).

[25] R Mikkelsen, Technical University of Denmark, F. M. Department of Mechanical Engineering, and MEK, "Actuator disc methods applied to wind turbines", en, OCLC: 474919625, PhD thesis, Lyngby, 2003.

[26] B. Sanderse, "Aerodynamics of wind turbine wakes - literature review", Tech. Rep., 2009.

[27] "Wind Energy Handbook", en, in *Wind Energy Handbook*, Chichester, UK: John Wiley & Sons, Ltd, May 2011, pp. i–xxxvii, ISBN: 978-1-119-99271-4 978-0-470-69975-1. DOI: `10.1002/9781119992714.fmatter`. [Online]. Available: `http://doi.wiley.com/10.1002/9781119992714.fmatter` (visited on 07/18/2019).

[28] I Katic, J Hojstrup, and N. O. Jensen, "A SIMPLE MODEL FOR CLUSTER EFFICIENCY", en, p. 5,

[29] M. J. Churchfield, *A Review of Wind Turbine Wake Models and Future Directions*, Boulder, Colarado, Aug. 2013. [Online]. Available: `https://www.nrel.gov/docs/fy14osti/60208.pdf` (visited on 07/19/2019).

[30] L. F. Richardson, *Weather prediction by numerical process*. Cambridge University Press, 1922. [Online]. Available: `https://archive.org/details/weatherpredictio00richrich`.

[31] P. Lynch, *Lecture notes in numerical weather prediction*, online.

[32] J. G. Charney, "Progress in dynamic meteorology", *Bulletin of the American Meteorological Society*, vol. 31, no. 7, pp. 231–236, 1950. DOI: `10.1175/1520-0477-31.7.231`. [Online]. Available: `https://doi.org/10.1175/1520-0477-31.7.231`.

[33] R. Stull, *Introduction to boundary layer meteorology*, eng. Kluwer, 1988, 666 s. ISBN: 9027727694, 9027727686, 9789027727688.

[34] W. C. Skamarock, J. B. Klemp, J. Dudhia, D. O. Gill, D. M. Barker, M. G. Duda, X.-Y. Huang, W. Wang, and J. G. Powers, "A Description of the Advanced Research WRF Version 3", en, p. 125,

[35] A. C. Fitch, J. B. Olson, J. K. Lundquist, J. Dudhia, A. K. Gupta, J. Michalakes, and I. Barstad, "Local and Mesoscale Impacts of Wind Farms as Parameterized in a Mesoscale NWP Model", en, *Monthly Weather Review*, vol. 140, no. 9, pp. 3017–3038, Sep. 2012, ISSN: 0027-0644, 1520-0493. DOI: `10.1175/MWR-D-11-00352.1`. [Online]. Available: `http://journals.ametsoc.org/doi/abs/10.1175/MWR-D-11-00352.1` (visited on 04/17/2019).

[36] X. G. Larsén, C. Vincent, and S. Larsen, "Spectral structure of mesoscale winds over the water", en, *Quarterly Journal of the Royal Meteorological Society*, vol. 139, no. 672, pp. 685–700, Apr. 2013, ISSN: 00359009. DOI: `10.1002/qj.2003`. [Online]. Available: `http://doi.wiley.com/10.1002/qj.2003` (visited on 08/28/2019).

[37] A. Peña, R. Floors, A. Sathe, S.-E. Gryning, R. Wagner, M. S. Courtney, X. G. Larsén, A. N. Hahmann, and C. B. Hasager, "Ten Years of Boundary-Layer and Wind-Power Meteorology at Hovsore, Denmark", en, *Boundary-Layer Meteorology*, vol. 158, no. 1, pp. 1–26, Jan. 2016, ISSN: 0006-8314, 1573-1472. DOI: `10.1007/s10546-015-0079-8`. [Online]. Available: `http://link.springer.com/10.1007/s10546-015-0079-8` (visited on 07/22/2019).

[38] H. Beck, J. J. Trujillo, G. Wolken-Möhlmann, A. P. Diaz, and V. C. Gomes, "D5.10 Mesoscale effects on wind farm energy yield reported", en, p. 30,

[39] O. Bossuyt, "Modelling and validation of wind turbine wake superposition: Using wind farm data", en, 2018. [Online]. Available: `http://resolver.tudelft.nl/uuid:8a9ff2f3-d4d4-470b-a5b8-11a08e31eb16` (visited on 08/19/2019).